SIAM J. IMAGING SCIENCES
Vol. 11, No. 4, pp. 2368–2428

Compensated Convexity Methods for Approximations and Interpolations of Sampled Functions in Euclidean Spaces: Applications to Contour Lines, Sparse Data, and Inpainting*

Kewei Zhang†, Elaine Crooks‡, and Antonio Orlando§

Abstract. This paper is concerned with applications of the theory of approximation and interpolation based on compensated convex transforms developed in [K. Zhang, E. Crooks, and A. Orlando, *SIAM J. Math. Anal.*, 48 (2016), pp. 4126–4154]. We apply our methods to (i) surface reconstruction starting from the knowledge of finitely many level sets (or "contour lines"); (ii) scattered data approximation; (iii) image inpainting. For (i) and (ii) our methods give interpolations. For the case of finite sets (scattered data), in particular, our approximations provide a natural triangulation and piecewise affine interpolation. Prototype examples of explicitly calculated approximations and inpainting results are presented for both finite and compact sets. We also show numerical experiments for applications of our methods to high density salt & pepper noise reduction in image processing, for image inpainting, and for approximation and interpolations of continuous functions sampled on finitely many level sets and on scattered points.

Key words. compensated convex transforms, scattered data, contour lines, interpolation, approximation, inpainting, Hausdorff stability, maximum principle, convex density radius, image inpainting, high density salt & pepper noise reduction

AMS subject classifications. 90C25, 90C26, 49J52, 52A41, 65K10

DOI. 10.1137/17M116152X

1. Introduction.

This paper is concerned with the application of the compensated-convexity–based theory for approximation and interpolation of sampled functions that was presented in our previous article [55] to surface reconstruction based on knowledge from finitely many level sets, scattered data approximation, and image inpainting.

In general, approximation theory is concerned with the problem of finding in the set of simple known functions one that is close in some sense to a more complicated otherwise

*Received by the editors December 15, 2017; accepted for publication (in revised form) August 23, 2018; published electronically October 23, 2018.

http://www.siam.org/journals/siims/11-4/M116152.html

Funding: This work was partially supported by EPSRC grant EP/K032208/1. The work of the second author was supported by the College of Science, Swansea University. The work of the third author was partially supported by the Argentinian Research Council (CONICET) through the project PIP 11220170100100CO, the National University of Tucumán through the project PIUNT CX-E625, and the FonCyT through the project PICT 2016 201-0105 Prestamo Bid.

†School of Mathematical Sciences, University of Nottingham, University Park, Nottingham, NG7 2RD, UK (kewei.zhang@nottingham.ac.uk).

‡Department of Mathematics, Swansea University, Singleton Park, Swansea, SA2 8PP, UK (e.c.m.crooks@swansea.ac.uk).

§CONICET, Departamento de Bioingeniería, FACET, Universidad Nacional de Tucumán, San Miguel de Tucumán CP 4000, Argentina (aorlando@herrera.unt.edu.ar).

unknown function. The variational theory is developed by specifying a priori the class of the approximating functions and the criteria that allow selecting an element of such a class. In the implementation of the theory, the approximating functions generally depend on unknown parameters that control their form, so that the problem boils down to selecting the parameters that allow meeting the chosen criteria. Such criteria are usually related to the error between the approximating functions and what is known about the function to be approximated and might contain some regularizing term that determines the regularity of the approximating function and makes the whole problem well posed.

Different classes of approximating functions, such as, for instance, algebraic polynomials [49], trigonometric polynomials [48, 49], radial basis functions [51, 11, 23], and continuous piecewise polynomials [40], have been considered, and while their definition is usually motivated by good approximating properties for a given field of application, on the other hand the specific nature of a class of functions also represents a restriction that limits their general application.

Total Variation–type models [42, 10], [17, Ch. 6] and geometric partial differential equations (PDEs) [13], [50, Ch. 1], [43, Ch. 8] have also been used as interpolation models. Their use has been principally motivated by applications in the field of image processing and geoscience. We mention in particular the applications to salt & pepper noise reduction [14], image inpainting (by using TV-inpainting models [9, 29], [17, Ch. 6], the Curvature Diffusion Driven inpainting model [16], the geometric PDE-based inpainting model [8], or other PDE-based models discussed in the monograph [45]), and image interpolation [6, 13, 28], among others. For the applications to geoscience, and in particular to the construction of digital elevation models, PDE-based interpolation models, such as the one considered in [2], where the interpolant is sought as the absolutely minimizing Lipschitz extension (AMLE) [5, 34] of the known values, have also been proposed and shown to be competitive against the classical interpolation methods such as the geodesic distance transformation method [46], the thin plate model [20, 26], and the kriging method [47].

As for these latter methods, although there is a well-developed mathematical theory on the existence and uniqueness of weak solutions of variational models [4, 7, 30], and of the viscosity solution [5, 34] of the PDE-based interpolation model used in [13], the quantitative effectiveness of such methods is mostly assessed on the basis of numerical experiments.

The new approximation and interpolation theory introduced in [55] is based, on the other hand, on the theory of compensated convex transforms [52, 57, 56, 54] and can be applied to general bounded real-valued functions sampled from either a compact set $K \subset \mathbb{R}^n$ or the complement $K = \mathbb{R}^n \setminus \Omega$ of a bounded open set Ω. The methods presented in [55] center on the so-called average approximation that is recalled in Definition 1.1 below. Importantly, [55] establishes error estimates for the approximation of bounded uniformly continuous functions, or Lipschitz functions, and of $C^{1,1}$-functions, and proves rigorously that the approximation methods are stable with respect to the Hausdorff distance between samples.

Here we apply the average approximation method developed in [55] to three important problems: approximation and interpolation for level sets and scattered data, for which the sample set $K \subset \mathbb{R}^n$ is compact, and the inpainting problem in image processing, where the aim is to reconstruct an image in a damaged region based on the image values in the undamaged part and the sample set $K = \mathbb{R}^n \setminus \Omega$ is the complement of a bounded open set Ω representing

the damaged area of the image. We will also present a series of prototype examples of explicitly calculated approximations that build insight into the behavior of the average approximation introduced in [55], as well as a selection of illustrative numerical experiments.

Before outlining the rest of the paper, we first recall the definitions of compensated convex transforms [52] and average approximation [55]. Suppose $f : \mathbb{R}^n \to \mathbb{R}$ is bounded. The quadratic lower and upper compensated convex transform [52] (lower and upper transforms for short) are defined for each $\lambda > 0$ by

$$\begin{aligned} &C^l_\lambda(f)(x) = \mathsf{co}[\lambda|\cdot|^2 + f](x) - \lambda|x|^2, \\ \text{resp.,}\quad &C^u_\lambda(f)(x) = \lambda|x|^2 - \mathsf{co}[\lambda|\cdot|^2 - f](x), \qquad x \in \mathbb{R}^n, \end{aligned} \tag{1.1}$$

where $|x|$ is the standard Euclidean norm of $x \in \mathbb{R}^n$ and $\mathsf{co}[g]$ denotes the convex envelope [33, 41] of a function $g : \mathbb{R}^n \to \mathbb{R}$ that is bounded below.

Let $K \subset \mathbb{R}^n$ be a nonempty closed set. Given a function $f : \mathbb{R}^n \to \mathbb{R}$, we denote by $f_K : \mathbb{R}^n \supset K \to \mathbb{R}$ the restriction of f to K, which can be thought of as a sampling of the original function f, which we would like to approximate, on the convex hull of the set K.

Suppose that for some constant $A_0 > 0$, $|f_K(x)| \le A_0$ for all $x \in K$. Then given $M > 0$, we define two bounded functions that extend f_K to $\mathbb{R}^n \setminus K$, namely

$$\begin{aligned} f^{-M}_K(x) &= f(x)\chi_K(x) - M\chi_{\mathbb{R}^n\setminus K} = \begin{cases} f_K(x), & x \in K, \\ -M, & x \in \mathbb{R}^n \setminus K\,, \end{cases} \\ f^{M}_K(x) &= f(x)\chi_K(x) + M\chi_{\mathbb{R}^n\setminus K} = \begin{cases} f_K(x), & x \in K, \\ M, & x \in \mathbb{R}^n \setminus K\,, \end{cases} \end{aligned} \tag{1.2}$$

where χ_G denotes the characteristic function of a set G.

Definition 1.1. *The* average compensated convex approximation *with scale $\lambda > 0$ and module $M > 0$ of the sampled function $f_K : K \to \mathbb{R}$ is defined by*

$$A^M_\lambda(f_K)(x) = \frac{1}{2}\left(C^l_\lambda(f^M_K)(x) + C^u_\lambda(f^{-M}_K)(x)\right), \quad x \in \mathbb{R}^n\,. \tag{1.3}$$

In addition, we can also set $M = +\infty$ in place of (1.2) and consider the following functions, which are commonly used in convex analysis:

$$f^{-\infty}_K(x) = \begin{cases} f(x), & x \in K, \\ -\infty, & x \in \mathbb{R}^n \setminus K, \end{cases} \qquad f^{+\infty}_K(x) = \begin{cases} f(x), & x \in K, \\ +\infty, & x \in \mathbb{R}^n \setminus K, \end{cases} \tag{1.4}$$

and define the corresponding average approximation approximation,

$$A^\infty_\lambda(f_K)(x) := \frac{1}{2}\left(C^l_\lambda(f^{+\infty}_K)(x) + C^u_\lambda(f^{-\infty}_K)(x)\right), \quad x \in \mathbb{R}^n\,. \tag{1.5}$$

By doing so, we can establish better approximation results than those obtained using f^{-M}_K and f^M_K, but $A^\infty_\lambda(f_K)$ is not Hausdorff stable with respect to sample sets, in contrast to the basic average approximation $A^M_\lambda(f_K)$ (see [55, Thm. 4.12]).

The plan of the rest of the paper is as follows. Section 2 introduces notation and recalls key definitions and results from our article [55], including error estimates for the average approximation $A_\lambda^M(f_K)$ of bounded and uniformly continuous, Lipschitz, and $C^{1,1}$ functions. In section 3, we consider level set interpolation and approximation, for which f is continuous and K consists of finitely many compact level sets. We give conditions so that $A_\lambda^M(f_K)$ is an interpolation between level sets and also establish a maximum principle. Section 4 treats the case of scattered data, when K is finite. In this case, we show that when $\lambda > 0$ is sufficiently large and when $M >> \lambda$, $A_\lambda^M(f_K)$ is a piecewise affine interpolation of f_K in the convex hull of K. Moreover, if K is regular in the sense of the Delaunay triangulation, we show that $A_\lambda^M(f_K)$ agrees with the piecewise interpolation given by the Delaunay method. In the irregular case that the Delaunay sphere S_r contains more than $n+1$ points in $\mathbb{R}^n$, $A_\lambda^M(f_K)$ is the average of the maximum and minimum piecewise affine interpolation over the convex hull of $K \cap S_r$. Section 5 presents error estimates for our average approximation in the context of the inpainting problem and compares and contrasts these estimates with the error analysis in [15]. We also give a simple one-dimensional example to illustrate the effect of the upper and lower compensated convex transforms $C_\lambda^u(f)$, $C_\lambda^l(f)$ and the average approximation $A_\lambda^M(f_K)$ on a jump function, to provide insight into how jump discontinuities behave under our approach.

Section 6 contains explicitly calculated prototype examples in $\mathbb{R}^2$, including both examples where the sample set K is finite, and also examples where K is not finite. We present graphs of our calculated average approximation for two irregular Delaunay cells, for four and for eight points on the unit circle. We also present prototype examples of contour line approximations, as well as prototypes for inpainting of functions that show that singularities such as ridges and jumps can be preserved subject to compensated convex approximations to the original function when the singular parts are close to each other. Section 7 discusses several numerical experiments for level set and point cloud reconstructions of functions and images, for image inpainting, and for restoration of images with heavy salt & pepper noise. Though such experiments are carried out only on a proof-of-concept level, we briefly report on the comparison of our method with some state-of-art methods. In section 8 we conclude the paper with proofs of our main theorems stated in sections 3, 4, and 5.

2. Notation and preliminaries.

Throughout the paper, we adopt the following notation and recall those results from [55] that will be used here for our proofs, to make the development as self-contained as possible. For the necessary background in convex analysis, we refer to the monographs [41, 33].

For a given set $E \subset \mathbb{R}^n$, with $\mathbb{R}^n$ an n-dimensional Euclidean space, $\bar{E}$, ∂E, $\mathring{E}$, E^c, and $\mathsf{co}[E]$ stand for the closure, the boundary, the interior, the complement, and the convex hull of E, i.e., the smallest convex set which contains E, respectively. For a convex set $E \subset \mathbb{R}^n$, we define the dimension of E, $\dim(E)$, as the dimension of the intersection of all affine manifolds that contain E, where by affine manifold we mean a translated subspace, i.e., a set N of the form $N = x + S$ with $x \in \mathbb{R}^n$ and S a subspace of $\mathbb{R}^n$. We then define $\dim(N) = \dim(S)$. We use the term convex body to denote a compact convex set with nonempty interior. The convex hull of a finite set of points is called a polytope and with the notation $\#(E)$ we denote the cardinality of the finite set E. If $E = \{x_1, \ldots, x_{k+1}\}$ and $\dim(E) = k$, then $\mathsf{co}[E]$ is called

a k-dimensional simplex and the points $x_1, \dots, x_{k+1}$ are called vertices. A zero-dimensional simplex is a point; a one-dimensional simplex is a line segment; a two-dimensional simplex is a triangle; a three-dimensional simplex is a tetrahedron. The condition that $\dim(E) = k$ is equivalent to require that the vectors $x_2 - x_1, \dots, x_{k+1} - x_1$ are linearly independent.

The open ball centered at $x \in \mathbb{R}^n$ and of radius $r > 0$ is denoted by $B(x; r) = \{y \in \mathbb{R}^n : |y - x| < r\}$ where $|\cdot|$ stands for the Euclidean norm in $\mathbb{R}^n$; thus $|x - y|$ is the distance between the points x, $y \in \mathbb{R}^n$. The diameter of the set $E \subset \mathbb{R}^n$, $\mathsf{diam}(E)$, is then defined as $\mathsf{diam}(E) = \sup_{x,y\in E} |x - y|$.

In this paper, we will assume, unless otherwise specified, that $K \subset \mathbb{R}^n$ is either a compact set or the complement of a bounded open set, that is, $K = \Omega^c$ where $\Omega \subset \mathbb{R}^n$ is a bounded open set. A function $g : \mathsf{co}[K] \subset \mathbb{R}^n \to \mathbb{R}$ is said to be an *interpolation* of f_K if $g = f$ in K, while for $\lambda > 0$, a family of functions $g_\lambda : \mathsf{co}[K] \subset \mathbb{R}^n \to \mathbb{R}$ is said to *approximate* f if $\lim_{\lambda\to+\infty} g_\lambda = f$ uniformly in K.

The error estimates obtained in [55] are expressed in terms of the modulus of continuity of the underlying function f to be approximated and of the convex density radius of K. For the convenience of the reader, these definitions are recalled here. The modulus of continuity of a bounded and uniformly continuous function f is defined as follows [19, 32].

Definition 2.1. *Let $f : \mathbb{R}^n \to \mathbb{R}$ be a bounded and uniformly continuous function in $\mathbb{R}^n$. Then,*

$$\omega_f : t \in [0, \infty) \to \omega_f(t) = \sup\Big\{|f(x) - f(y)| : x, y \in \mathbb{R}^n \text{ and } |x - y| \le t\Big\} \tag{2.1}$$

is called the modulus of continuity of f.

We also recall that the modulus of continuity of f has the following properties [32, pp. 19–21].

Proposition 2.2. *Let $f : \mathbb{R}^n \to \mathbb{R}$ be a bounded and uniformly continuous function in $\mathbb{R}^n$. Then the modulus of continuity ω_f of f satisfies the following properties:*

$$\begin{aligned} &\text{(i)} && \omega_f(t) \to \omega_f(0) = 0 \text{ as } t \to 0;\\ &\text{(ii)} && \omega_f \text{ is a nonnegative and nondecreasing continuous function on } [0, \infty);\\ &\text{(iii)} && \omega_f \text{ is subadditive: } \omega_f(t_1 + t_2) \le \omega_f(t_1) + \omega_f(t_2) \text{ for all } t_1, t_2 \ge 0\,. \end{aligned} \tag{2.2}$$

Any function ω defined on $[0, \infty)$ and satisfying (2.2)(i), (ii), (iii) is called *a modulus of continuity*. A modulus of continuity ω can be bounded from above by an affine function (see [19, Lemma 6.1]); that is, there exist constants $a > 0$ and $b \ge 0$ such that

$$\omega(t) \le at + b \quad (\text{for all } t \ge 0). \tag{2.3}$$

As a result, given ω_f, one can define the least concave majorant of ω_f, which we denote by ω, which is also a modulus of continuity with the property (see [19])

$$\frac{1}{2}\omega(t) \le \omega_f(t) \le \omega(t) \quad \text{for all } t \in [0, \infty)\,. \tag{2.4}$$

The convex density radius of a point $x \in \mathsf{co}[K]$ with respect to the set K and the convex density radius of K in $\mathsf{co}[K]$ are the geometrical quantities that describe the set K with respect to its convex hull and are such properties which enter the error estimates for our approximation operators. We next recall their definition from [55].

Definition 2.3. *Suppose $K \subset \mathbb{R}^n$ is a nonempty and closed set, and denote by* $\operatorname{dist}(x; K)$ *the Euclidean distance of x to K. For $x \in \mathsf{co}[K]$, consider the balls $B(x; r)$ such that $x \in \mathsf{co}[\bar{B}(x; r) \cap K]$. The convex density radius of x with respect to K is defined as*

$$r_c(x) = \inf\{r \geq 0 \text{ such that } x \in \mathsf{co}[\bar{B}(x; r) \cap K]\}\,, \tag{2.5}$$

whereas the convex density radius of K in $\mathsf{co}[K]$ is defined by

$$r_c(K) = \sup\{r_c(x),\ x \in \mathsf{co}[K]\}\,. \tag{2.6}$$

Here it is also useful to introduce the following, more geometric quantities. Let $Q \subset \mathbb{R}^n$ be a bounded set, and given $x \in Q$ and $\nu \in \mathbb{R}^n$ with $|\nu| = 1$, define the quantity

$$d_\nu(x) = d_\nu^+(x) + d_\nu^-(x)\,,$$

where

$$d_\nu^+(x) = \sup\left\{t > 0 :\ x + s\nu \in Q \text{ for } 0 \leq s \leq t\right\} \text{ and } d_\nu^-(x) = \sup\left\{t > 0 :\ x - s\nu \in Q \text{ for } 0 \leq s \leq t\right\}.$$

It is then easy to see that $d_\nu(x)$ is the length of the line segment with direction ν passing through x and intersecting ∂Q at two points on each side. We also define

$$d(x) = \inf\left\{d_\nu(x),\ \nu \in \mathbb{R}^n,\ |\nu| = 1\right\} \tag{2.7}$$

and the thickness of the set $Q \subset \mathbb{R}^n$ as

$$D_Q = \sup\left\{d(x),\ x \in Q\right\}. \tag{2.8}$$

Remark 2.4.

(a) Given a nonempty bounded open set $Q = \Omega \subset \mathbb{R}^n$, by comparing the definitions (2.5) of $r_c(x)$ and (2.8) of $d(x)$, it is straightforward to verify that

$$r_c(x) \leq d(x) \tag{2.9}$$

for $x \in \Omega$.

(b) If the interior $\mathring{Q} = \varnothing$, such as in the case of a discrete set, then its thickness D_Q is zero.

We recall next the error estimates for our average approximation operators developed in [55] and refer the reader to [55] for proofs and details. For the case of K compact and $M = +\infty$, we have the following.

Theorem 2.5 (see [55, Theorem 3.6]). *Suppose $f : \mathbb{R}^n \to \mathbb{R}$ is bounded and uniformly continuous, satisfying $|f(x)| \leq A_0$ for some constant $A_0 > 0$ and all $x \in \mathbb{R}^n$, and let $K \subset \mathbb{R}^n$ be a nonempty compact set. Denote by ω the least concave majorant of the modulus of continuity of f. Let $a \geq 0$, $b \geq 0$ be such that $\omega(t) \leq at + b$ for $t \geq 0$. Then for all $\lambda > 0$ and $x \in \mathsf{co}[K]$,*

$$|A_\lambda^\infty(f_K)(x) - f(x)| \leq \omega\left(r_c(x) + \frac{a}{\lambda} + \sqrt{\frac{2b}{\lambda}}\right), \tag{2.10}$$

where $r_c(x) \geq 0$ is the convex density radius of x with respect to K. If we further assume that f is a globally Lipschitz function with Lipschitz constant $L > 0$, then for all $\lambda > 0$ and $x \in \mathsf{co}[K]$,

$$|A_\lambda^\infty(f_K)(x) - f(x)| \leq Lr_c(x) + \frac{L^2}{\lambda}. \tag{2.11}$$

Section 4 will discuss an application of Theorem 2.5 to the case of scattered data approximation. We will apply Theorem 2.5 also to the case of salt & pepper noise removal, where K is the compact set given by the part of the image which is noise free. Section 7 contains a numerical experiment showing such an application.

A statement similar to Theorem 2.5 is obtained with M finite in the case that $K = \Omega^c$, where $\Omega \subset \mathbb{R}^n$ is a nonempty bounded open set. In this case, clearly $\mathsf{co}[K] = \mathbb{R}^n$ and the error estimate of the average approximation $A_\lambda^M(f_K)$ is as follows.

Theorem 2.6 (see [55, Theorem 3.7]). *Suppose $f : \mathbb{R}^n \to \mathbb{R}$ is bounded and uniformly continuous, satisfying $|f(x)| \leq A_0$ for some constant $A_0 > 0$ and all $x \in \mathbb{R}^n$. Let $\Omega \subset \mathbb{R}^n$ be a bounded open set, d_Ω the diameter of Ω, and $K = \Omega^c$. Denote by ω the least concave majorant of the modulus of continuity of f, and let $a \geq 0$, $b \geq 0$ be such that $\omega(t) \leq at + b$ for $t \geq 0$. Then for $\lambda > 0$, $M > A_0 + \lambda d_\Omega^2$, and all $x \in \mathbb{R}^n$,*

$$|A_\lambda^M(f_K)(x) - f(x)| \leq \omega\left(r_c(x) + \frac{a}{\lambda} + \sqrt{\frac{2b}{\lambda}}\right), \tag{2.12}$$

where $r_c(x) \geq 0$ is the convex density radius of x with respect to K. If we further assume that f is a globally Lipschitz function with Lipschitz constant $L > 0$, then for $\lambda > 0$, $M > A_0 + \lambda d_\Omega^2$, and all $x \in \mathbb{R}^n$, we have

$$|A_\lambda^M(f_K)(x) - f(x)| \leq Lr_c(x) + \frac{L^2}{\lambda}. \tag{2.13}$$

Under an additional restriction on f and on K, it is possible to extend the results of Theorem 2.6 to the case when K is a compact set and thus to obtain error estimates independent of M. More precisely, the following result refers to the case where we are given the values of the function f on the union of a compact set and the complement of a bounded open set. This extension allows the application of Theorem 2.6 to the problem of inpainting, for instance.

Corollary 2.7 (see [55, Corollary 3.9]). *Suppose $f : \mathbb{R}^n \to \mathbb{R}$ is bounded and uniformly continuous satisfying $|f(x)| \leq A_0$ for some constant $A_0 > 0$ and all $x \in \mathbb{R}^n$. Assume that*

$f(x) = c_0$ for $|x| \geq r > 0$, where $c_0 \in \mathbb{R}$ and $r > 0$ are constants. Let $K \subset \mathbb{R}^n$ be a nonempty compact set satisfying $K \subset \bar{B}(0; r)$. For $R > r$, define $K_R := K \cup B^c(0; R)$. Denote by ω the least concave majorant of the modulus of continuity of f. Let $a \geq 0$, $b \geq 0$ be such that $\omega(t) \leq at + b$ for $t \geq 0$. Then for all $\lambda > 0$, $M > A_0 + \lambda(R + r)^2$, and all $x \in \mathsf{co}[K]$,

$$|A_\lambda^M(f_{K_R})(x) - f(x)| \leq \omega\left(r_c(x) + \frac{a}{\lambda} + \sqrt{\frac{2b}{\lambda}}\right), \tag{2.14}$$

where $r_c(x) \geq 0$ is the convex density radius of x with respect to K. If we further assume that f is a globally Lipschitz function with Lipschitz constant $L > 0$, then for $\lambda > 0$, $M > A_0 + \lambda(R + r)^2$, and all $x \in \mathsf{co}[K]$, we have

$$|A_\lambda^M(f_{K_R})(x) - f(x)| \leq Lr_c(x) + \frac{L^2}{\lambda}. \tag{2.15}$$

If we further assume that f is a $C^{1,1}$ function such that $|Df(x) - Df(y)| \leq L|x - y|$ for all $x, y \in \mathbb{R}^n$ and $L > 0$ is a constant, then for $\lambda > L$, $M > A_0 + \lambda(R + r)^2$, and all $x \in \mathsf{co}[K]$, we have

$$|A_\lambda^M(f_{K_R})(x) - f(x)| \leq \frac{L}{4}\left(\frac{\lambda + L/2}{\lambda - L/2} + 1\right) r_c^2(x). \tag{2.16}$$

Furthermore, in case (iii), *$A_\lambda^M(f_{K_R})$ is an interpolation of f_K in $\mathbb{R}^n$.*

The conditions of Corollary 2.7 can be realized, for instance, in the case when we can define f to be zero outside a large ball containing K.

Theorem 2.6 and Corollary 2.7 will be applied to the case of (i) surface reconstructions from a finitely many level sets representation and (ii) inpainting of damaged images, where Ω is the domain to be inpainted and $K = \Omega^c$. We will discuss such applications in section 3 and section 5, respectively, whereas section 7 contains some numerical experiments of both applications.

We conclude this section by giving the following property, which will be useful in section 4, which deals with scattered data approximations.

Proposition 2.8 (the restriction property). *Let $m \geq 1$, $n \geq 1$. Suppose $f : \mathbb{R}^n \to \mathbb{R}$ is bounded, satisfying $|f(x)| \leq M$ for some $M > 0$ and for all $x \in \mathbb{R}^n$. Let $g^{\pm M} : \mathbb{R}^n \times \mathbb{R}^m \to \mathbb{R}$ be defined, respectively, as follows:*

$$g^M(x, y) = \begin{cases} f(x), & x \in \mathbb{R}^n,\ y = 0 \in \mathbb{R}^m, \\ M, & x \in \mathbb{R}^n,\ y \in \mathbb{R}^m,\ y \neq 0, \end{cases}$$

$$g^{-M}(x, y) = \begin{cases} f(x), & x \in \mathbb{R}^n,\ y = 0 \in \mathbb{R}^m, \\ -M, & x \in \mathbb{R}^n,\ y \in \mathbb{R}^m,\ y \neq 0. \end{cases}$$

Then

$$C_\lambda^l(g^M)(x, 0) = C_\lambda^l(f)(x) \quad \text{and} \quad C_\lambda^u(g^{-M})(x, 0) = C_\lambda^u(f)(x) \quad (\text{for } x \in \mathbb{R}^n).$$

In the case when the sampled set K is compact, the restriction property and Corollary 2.7 imply that if K is contained in a k-dimensional plane $E \subset \mathbb{R}^n$, we can then calculate the average approximation operator $A^M_\lambda(f_K(x))$ for $x \in \mathsf{co}[K] \subset E$ by restricting our calculations in E.

3. Level set approximations. We consider the case where the sampled set is given by the union of finitely many compact level sets, that is, we know the values of a continuous function f only on finitely many compact contour lines, and we want to study the structure of $A^M_\lambda(f_K)$. We will establish a result which gives a natural bound on the value of $A^M_\lambda(f_K)$, ensuring that, for $\lambda > 0$ sufficiently large, the value of $A^M_\lambda(f_K)$ at points between level sets is between the values of the corresponding level sets, and present an error estimate for $A^M_\lambda(f_K)$.

Let $f : \mathbb{R}^n \to \mathbb{R}$ be a continuous function and $a \in \mathbb{R}$. Denote by $\Gamma_a = \{x \in \mathbb{R}^n,\ f(x) = a\}$ the level set of f of level a and by $V_a := \{x \in \mathbb{R}^n,\ f(x) \le a\}$ the sublevel set of f of level a.

We then have the following result.

Theorem 3.1. *Suppose $f : \mathbb{R}^n \to \mathbb{R}$ is continuous and that for $a_0 < a_1 < \cdots < a_m$, $m \in \mathbb{N}$, the level sets $\Gamma_{a_i} = \{x \in \mathbb{R}^n,\ f(x) = a_i\}$ are compact for $i = 0, 1, \ldots, m$. Denote by*

$$\delta_0 = \min\Big\{\operatorname{dist}(\Gamma_{a_i}, \Gamma_{a_j}),\ 0 \le i, j \le m,\ i \ne j\Big\} > 0$$

the minimum Euclidean distance between two different level sets. Define $K = \cup_{i=0}^m \Gamma_{a_i}$ and denote by d_K the diameter of K. If $\lambda > (a_m - a_0)/\delta_0^2$ and $M > \lambda d_K^2 + \max_K |f|$, then the following hold:

(i) *$A^M_\lambda(f_K)$ is an interpolation of f from K to $\mathsf{co}[K]$, that is, for $x_0 \in \Gamma_{a_i}$, $i = 0, 1, \ldots, m$,*

$$A^M_\lambda(f_K)(x_0) = a_i. \tag{3.1}$$

(ii) *For each x_0 satisfying $a_i \le f(x_0) \le a_{i+1}$ for some $0 \le i \le m-1$,*

$$a_i \le A^M_\lambda(f_K)(x_0) \le a_{i+1}\,. \tag{3.2}$$

(iii) *$A^M_\lambda(f_K)(x_0) = a_0$ for $x_0 \in V_{a_0}$.*

Remark 3.2.

(a) A sufficient condition for the level set Γ_a to be compact is that f is continuous and either $\lim_{|x|\to\infty} f(x) = +\infty$ or $\lim_{|x|\to\infty} f(x) = -\infty$.

(b) It might happen that there is an open subset of $\{x \in \mathbb{R}^n,\ a_i \le f(x) \le a_{i+1}\}$ on which $A^M_\lambda(f_K)(x) = a_i$ or $A^M_\lambda(f_K)(x) = a_{i+1}$. Therefore, Theorem 3.1 gives a weak maximum principle.

(c) In $\mathbb{R}^2$, it is not difficult to see that if two neighboring level sets are parallel lines, then our interpolation gives a plane passing through these two lines. However, if the function under consideration is not continuous, different level sets can "intersect" each other. In general, it is not clear what the natural level set approximations for functions with jump discontinuity will be like. In section 6 we will present a prototype example of two level lines which are not parallel to each other and work out an analytical expression of the interpolation operator $A^M_\lambda(f_K)$ for such a case.

We next give an error estimate for our level set average approximation $A_\lambda^M(f_K)$, which is obtained by applying Corollary 2.7 [55, Corollary 3.9]. We first introduce some further definitions that are needed for the application of this result. Under the assumptions of Theorem 3.1, for $i = 0, 1, \dots, m-1$, define the open set

$$\Omega_i = \{x \in \mathbb{R}^n,\, a_i < f(x) < a_{i+1}\}\,, \tag{3.3}$$

and then for $x \in \Omega_i$, define $d_i(x)$ using (2.8) with $Q = \Omega_i$. Suppose that V_{a_m} is compact, let $R > 0$ be such that $V_{a_m} \subset B(0;\, R)$, and set $V_R^m = V_{a_m} \cup B^c(0;\, R)$. Then define the auxiliary function

$$\tilde{f}_{V_R^m}(x) = \begin{cases} f(x), & x \in V_{a_m}, \\ a_m + 1, & x \in B^c(0;\, R)\,. \end{cases}$$

We consider the following two cases.

(i) If f is continuous, $\tilde{f}_{V_R^m}$ is bounded and uniformly continuous in V_R^m. Therefore, by the Tietze extension theorem [21, p. 149], $\tilde{f}_{V_R^m}$ can be extended to $\mathbb{R}^n$ as a bounded uniformly continuous function. We denote this extension by $\tilde{f}$ and by $\tilde{A}_0 > 0$ an upper bound of $|\tilde{f}|$. Clearly, $\tilde{f}(x) = f(x)$ for $x \in V_{a_m}$. Furthermore, we denote by $\tilde{\omega}(t)$ the least concave majorant of the modulus of continuity of $\tilde{f}$, which is itself a modulus of continuity, thus satisfies the properties (2.2), and, in particular, can be bounded from above by an affine function; that is, there exist some constants $\tilde{a} \geq 0$ and $\tilde{b} \geq 0$ such that $\tilde{\omega}(t) \leq \tilde{a}t + \tilde{b}$ for all $t \geq 0$.

(ii) If f is Lipschitz continuous with Lipschitz modulus $L > 0$, then $\tilde{f}_{V_R^m}$ is bounded and Lipschitz continuous in V_R^m with a possibly different Lipschitz modulus $\tilde{L}$ such that

$$\tilde{L} \leq \max\left\{L,\, \max_{V_{a_m}} |f| + |a_m + 1|\right\}. \tag{3.4}$$

By Kirszbraun's theorem [24, p. 202], $\tilde{f}_{V_R^m}$ can then be extended to $\mathbb{R}^n$ as a bounded Lipschitz function. Again we denote this extension by $\tilde{f}$ and assume that $|\tilde{f}(x)| \leq \tilde{A}_0$ for all $x \in \mathbb{R}^n$.

With the notation above, we have the following error estimates for $A_\lambda^M(f_K)$.

Proposition 3.3. *Suppose $f : \mathbb{R}^n \to \mathbb{R}$ is continuous and that for $a_0 < a_1 < \cdots < a_m$, the sublevel sets $V_{a_0} \subset V_{a_1} \subset \cdots \subset V_{a_m}$ are nonempty and compact. Let Γ_{a_i} be the level set of f of level a_i, $K = \cup_{i=0}^m \Gamma_{a_i}$, and $d_i(x)$, Ω_i be defined by (2.8), (3.3), respectively, for $i = 0, 1, \dots, m-1$. Denote by $\tilde{f}$ the function defined in* (i) *above, and by $\tilde{A}_0$ an upper bound of $|\tilde{f}|$. If $\lambda > a_m - a_0 + 1$ and $M > \tilde{A}_0 + \lambda(2R+1)^2$, then for all $x \in \Omega_i$, $i = 0, \dots, m-1$, we have*

$$|A_\lambda^M(f_K)(x) - f(x)| \leq \tilde{\omega}\left(d_i(x) + \frac{\tilde{a}}{\lambda} + \sqrt{\frac{2\tilde{b}}{\lambda}}\right), \tag{3.5}$$

where $\tilde{\omega}$ is the least concave majorant of the modulus of continuity of $\tilde{f}$. If we further assume that f is a globally Lipschitz function of Lipschitz constant $L > 0$, $\lambda > a_m - a_0 + 1$, and

$M > \tilde{A}_0 + \lambda(2R+1)^2$, then for all $x \in \Omega_i$, $i = 0, \ldots, m-1$, we have

$$|A^M_\lambda(f_K)(x) - f(x)| \leq \tilde{L} d_i(x) + \frac{\tilde{L}^2}{\lambda}, \tag{3.6}$$

where $\tilde{L}$ is defined by (3.4).

4. Scattered data approximations. We now turn our attention to the so-called case of "scattered data" approximation [51] corresponding to a discrete sampled set K. Since for any function $f : \mathbb{R}^n \to \mathbb{R}$, the restriction f_K of f to a finite set K is always a Lipschitz function, the following result provides a sufficient condition for our upper and lower transforms to be interpolations in this case.

Theorem 4.1. *Suppose $K = \{x_1, x_2, \ldots, x_m\} \subset \mathbb{R}^n$ is a finite set with distinct points and assume $f : K \subset \mathbb{R}^n \to \mathbb{R}$ is a function. Assume $-M < f(x_j) < M$ for $j = 1, \ldots, m$ and let $L > 0$ be the Lipschitz constant of $f : K \subset \mathbb{R}^n \to \mathbb{R}$. Define $\alpha = \min\{|x_i - x_j|,\ x_i, x_j \in K, i \neq j\} > 0$. Then for $\lambda \geq L/\alpha$,*

$$C^u_\lambda(f_K^{-M})(x_j) = f(x_j) \quad \text{and} \quad C^l_\lambda(f_K^M)(x_j) = f(x_j) \quad \text{for } x_j \in K.$$

Let $K \subset \mathbb{R}^n$ be a finite set. Without loss of generality, from now on, we assume that $\dim(\mathsf{co}[K]) = n$, that is, that $\mathsf{co}[K] \subset \mathbb{R}^n$ is a convex body. In the case $\dim(\mathsf{co}[K]) = k < n$, we can simply translate K so that $0 \in K$, and let $E_k = \mathsf{span}(\mathsf{co}[K])$ where $\mathsf{span}(\mathsf{co}[K])$ is the k-dimensional subspace spanned by $\mathsf{co}[K]$. In this case, $E_k \subset \mathbb{R}^n$ is a supporting plane of $\mathsf{co}[K]$ and we only need to work in E_k given that in our interpolation problem we are only interested in values of our approximation in $\mathsf{co}[K]$. We can therefore reduce our approximation/interpolation problem to E_k by applying Proposition 2.8.

In order to describe our approximation/interpolation results, we first need to introduce notions related to the Voronoi diagram and Delaunay triangulation for a finite set K [18, 38, 22].

Let $K = \{x_1, \ldots, x_m\}$ be a finite set of distinct points of $\mathbb{R}^n$, and denote $m = \#(K)$. We define $\mathcal{V}(K)$, the Voronoi diagram of K, to be the partition of $\mathbb{R}^n$ into m cells, one for each point of K, with the property that a point $x \in \mathbb{R}^n$ belongs to the cell corresponding to the point $x_i \in K$ if $|x - x_i| < |x - x_j|$ for each $x_j \in K$ with $j \neq i$. We then denote by $M(K)$ the Voronoi edges of the Voronoi diagram $\mathcal{V}(K)$ of K, meaning the set of the edges of $\mathcal{V}(K)$ where a point $y \in M(K)$ if there are at least two different points $x_i, x_j \in K$ such that $\mathrm{dist}(y, K) = |y - x_i| = |y - x_j| > 0$. Then there are finitely many points $y_1, \ldots, y_l \in M(K)$, called Voronoi vertices, whose set is denoted by $V(K)$, with the property that there are corresponding radii $r_1, \ldots, r_l > 0$, such that for each $y_i \in V(K)$, there are $m_i \geq n+1$ points $x^i_1, \ldots, x^i_{m_i} \in K$ such that $\mathrm{dist}(y_i, K) = |y_i - x^i_j| = r_i$ so that the open ball $B(y_i; r_i)$ does not intersect K and $\bar{B}(y_i; r_i) \cap K = \{x^i_1, \ldots, x^i_{m_i}\}$. If we write $K_i = \{x^i_1, \ldots, x^i_{m_i}\}$ for each $i \in \{1, \ldots, l\}$, we also have that $\dim(\mathsf{co}[K_i]) = n$, $\cup_{j=1}^l \mathsf{co}[K_j] = \mathsf{co}[K]$, and if $i \neq j$, either $\dim(\mathsf{co}[K_i] \cap \mathsf{co}[K_j]) < n$ or $\mathsf{co}[K_i] \cap \mathsf{co}[K_j] = \emptyset$ [38].

For each $i = 1, \ldots, l$, $\mathsf{co}[K_i]$ is referred to as a Delaunay cell with generator K_i, center y_i, and radius r_i, and the ball $B(y_i; r_i)$ is called the associated open ball of the Delaunay cell $\mathsf{co}[K_i]$. We have $K_i = K \cap \partial B(y_i; r_i)$ while $K \cap B(y_i; r_i) = \varnothing$. A Delaunay cell is then said to be

regular if it is an n-dimensional simplex (so, in particular, a triangle if $n = 2$ and a tetrahedron if $n = 3$). If each Delaunay cell $\mathsf{co}[K_i]$ in $\mathsf{co}[K]$ is regular, the set $\{\mathsf{co}[K_1], \mathsf{co}[K_2], \ldots, \mathsf{co}[K_l]\}$ is said to be the regular Delaunay triangulation of $\mathsf{co}[K]$.

In the following, we consider two different situations:

(i) Each Delaunay cell $\mathsf{co}[K_i]$ is an n-dimensional simplex; that is, $\mathsf{co}[K]$ has a regular Delaunay triangulation.

(ii) For some or for all K_i's, $\dim(\mathsf{co}[K_i]) = \dim(\mathsf{co}[K]) = n$ and $\#(K_i) > n + 1$; that is, the Delaunay cell is a convex polytope that is not an n-dimensional simplex.

We will show that if (i) holds, that is, if we have a regular Delaunay triangulation of $\mathsf{co}[K]$, then our average approximation $A_\lambda^M(f_K)$ defines the usual piecewise affine interpolation based on this Delaunay triangulation [38, p. 191] when $\lambda > 0$ and $M >> \lambda$ are sufficiently large. If (ii) occurs, our average approximation $A_\lambda^M(f_K)$ will be the average of the minimum and maximum piecewise affine interpolations of f_K in the cell.

Remark 4.2. A remarkable difference between our average approximation $A_\lambda^M(f_K)$ and the usual design of piecewise affine constructions is that we do not need to know or compute the Delaunay cells in advance. Our method simply directly generates the piecewise affine function.

Before we state our first structural theorem on the effect of the upper, lower, and average approximations over a regular cell, we need the following lemma.

Lemma 4.3. *Let $B(x^*; r) \subset \mathbb{R}^n$ be the open ball centered at x^* with radius $r > 0$, and let $S = \{x_1, x_2, \ldots, x_m\} \subset \partial B(x^*; r)$ be a finite set with distinct points and with $\#(S) = m \geq n + 1$. Assume $\mathsf{co}[S] \subset \bar{B}(x^*; r)$ is the convex hull of S satisfying $\dim(\mathsf{co}[S]) = n$. Suppose $f_S : S \to \mathbb{R}$ is a real-valued function with Lipschitz constant $L > 0$. If there is an affine function $\ell_s : \mathbb{R}^n \to \mathbb{R}$ such that $\ell_s(x_i) = f_S(x_i)$ for all $x_i \in S$, then there is a constant $C_s > 0$ such that the gradient of ℓ satisfies $|D\ell_s(x)| \leq C_s L$.*

Remark 4.4. In Lemma 4.3, if $m = n + 1$, then $\mathsf{co}[S]$ is an n-dimensional simplex and there is an affine function ℓ_s such that $\ell_s(x) = f_S(x)$ for $x \in S$. However, if $m > n + 1$, in general one cannot find an affine function satisfying $\ell_s(x) = f_S(x)$ for $x \in S$. We will deal with such a case together with a more general one in Lemma 4.9 and in Theorem 4.11.

We now calculate the transforms $C_\lambda^u(f_K^{-M})$, $C_\lambda^l(f_K^M)$, and $A_\lambda^M(f_K)$ in a regular Delaunay cell $\mathsf{co}[S]$ satisfying $m = \#(S) = n+1$ and $\dim(\mathsf{co}[S]) = n$. For each regular cell $\mathsf{co}[S]$, define

$$\sigma_s = \min\left\{|x_j - x_s| - r_s,\ x_j \in K \setminus S\right\} > 0,$$

where x_s, r_s are the center and radius, respectively, of the associated Delaunay ball $B(x_s; r_s)$ of $\mathsf{co}[S]$, and let C_s be the constant given by Lemma 4.3 for the affine function ℓ_s associated with $\{(x, f_S(x)),\ x \in S\}$. We then have the following result.

Theorem 4.5. *Let $K = \{x_i\}_{i=1}^m \subset \mathbb{R}^n$ be a finite set with distinct points, and let $f_K : K \to \mathbb{R}$ be a function with Lipschitz constant $L > 0$ and bound $A_0 > 0$; that is, $|f_K(x)| \leq A_0$ for $x \in K$. Suppose $S = \{x_1, x_2, \ldots, x_{l+1}\} \subset K$ satisfies that $\mathsf{co}[S]$ is a regular Delaunay cell with associated Delaunay ball $B(x_s; r_s)$. Let $\ell_s : \mathbb{R}^n \to \mathbb{R}$ be the affine function given by Lemma*

4.3 *for S and f_K restricted on S. Then, for every $x \in \mathsf{co}[S]$,*

$$C_\lambda^u(f_K^{-M})(x) = \lambda|x-x_s|^2 - \lambda r_s^2 + \ell_s(x), \qquad C_\lambda^l(f_K^M)(x) = \lambda r_s^2 - \lambda|x-x_s|^2 + \ell_s(x),$$
$$A_\lambda^M(f_K)(x) = \frac{C_\lambda^u(f_K^{-M})(x) + C_\lambda^l(f_K^M)(x)}{2} = \ell_s(x) \tag{4.1}$$

whenever

$$\lambda > \frac{2A_0}{\sigma_s(2r_s+\sigma_s)} + \frac{C_s L}{\sigma_s} \tag{4.2}$$

and

$$M > \lambda r_s^2 + C_s L r_s + A_0 + \frac{C_s^2 L^2}{4\lambda}. \tag{4.3}$$

Remark 4.6. If we replace our functions f_K^{-M} and f_K^M by $f_K^{-\infty}$ and f_K^∞, respectively, defined by

$$f_K^{-\infty}(x) = \begin{cases} f_K(x) & \text{if } x \in\in K\,, \\ -\infty & \text{if } x \in \mathbb{R}^n \setminus K\,, \end{cases} \qquad \text{and} \qquad f_K^{\infty}(x) = \begin{cases} f_K(x) & \text{if } x \in K\,, \\ +\infty & \text{if } x \in \mathbb{R}^n \setminus K\,, \end{cases}$$

then condition (4.2) alone is sufficient to obtain (4.1). Although by setting $M = +\infty$ we have a mathematically simpler statement, the resulting approximations would not, however, meet the Hausdorff stability property (see [55, Thm. 4.12] for a Hausdorff stability theorem for $A_\lambda^M(f_K)$).

If we further assume that for the given finite set K there is a regular Delaunay triangulation of $\mathsf{co}[K]$, which thus consists of n-dimensional simplices, we can then easily give global explicit descriptions of $C_\lambda^u(f_K^{-M})$ and $C_\lambda^l(f_K^M)$, and hence of $A_\lambda^M(f_K)$ in each n-dimensional Delaunay simplex. This, however, requires $\lambda > 0$ and $M > 0$ to be sufficiently large.

Corollary 4.7. *Let $K \subset \mathbb{R}^n$ be a finite set with distinct points such that it admits a regular Delaunay triangulation $\mathcal{D}(K)$ of $\mathsf{co}[K]$, thus comprised of the n-dimensional simplices $\mathsf{co}[S_1], \dots, \mathsf{co}[S_l]$, where $V(K)$ is the set of vertices of the Voronoi diagram $\mathcal{V}(K)$ of K with $\#(V(K)) = l$. For each Delaunay cell S_i for $i = 1, \dots, l$, consider its associated open ball $B(y_i; r_i)$ such that $B(y_i; r_i) \cap K = \varnothing$ and $K \cap \bar{B}(y_i; r_i) = S_i$ for $i = 1, \dots, l$. Define $\sigma_i = \min\{|x-y_i| - r_i,\ x \in K \setminus S_i\}$.*

Let $f_K : K \subset \mathbb{R}^n \to \mathbb{R}$ be a function with Lipschitz constant $L > 0$ satisfying, for some $A_0 > 0$, $|f_K(x)| \le A_0$ for all $x \in K$. Let ℓ_i be the affine function defined in Lemma 4.3 for S_i, such that $\ell_i(x) = f_K(x)$ for $x \in S_i$ and $|D\ell_i(x)| \le C_i L$ for some constant $C_i > 0$, $i = 1, \dots, l$. Then in each simplex $\mathsf{co}[S_i]$, $i = 1, \dots, l$, and for every $x \in \mathsf{co}[S_i]$, we have

$$C_\lambda^u(f_K^{-M})(x) = \lambda|x-x_i|^2 - \lambda r_i^2 + \ell_i(x), \qquad C_\lambda^l(f_K^M)(x) = \lambda r_i^2 - \lambda|x-x_i|^2 + \ell_i(x)\,,$$
$$A_\lambda^M(f_K)(x) = \frac{C_\lambda^u(f_K^{-M})(x) + C_\lambda^l(f_K^M)(x)}{2} = \ell_i(x) \tag{4.4}$$

whenever

$$\lambda > \max_{1\le i\le m}\left(\frac{2A_0}{\sigma_i(2r_i+\sigma_i)}+\frac{C_iL}{\sigma_i}\right) \tag{4.5}$$

and

$$M > \max_{1\le i\le m}\left(\lambda r_i^2 + C_iLr_i + A_0 + \frac{C_i^2L^2}{4\lambda}\right).$$

Remark 4.8. An observation similar to Remark 4.6 for Theorem 4.5 can be made for Corollary 4.7. Under the assumptions of Corollary 4.7, condition (4.5) is sufficient to ensure that (4.4) holds with $f_K^{-\infty}$, f_K^{∞}, and $A_\lambda^\infty(f_K)$, respectively, for $i = 1,\dots,l$ and for every $x \in \mathsf{co}[S_i]$.

Let $S = \{x_1,\dots,x_m\} \subset \mathbb{R}^n$. Next we study the structure of our upper and lower transforms and average approximations when the n-dimensional Delaunay cell $\mathsf{co}[S]$ is not a simplex, that is, $\#(S) = m > n+1$. In this case, we say that the n-dimensional Delaunay cell $\mathsf{co}[S]$ is not regular. Without loss of generality we may assume that there is an open ball $B(0;r)$ centered at 0 with radius $r > 0$, such that $S \subset \partial B(0;r)$. Let $f_S : S \to \mathbb{R}$ be a given function, and write $f_S(x_i) = v_i$, $i = 1,\dots,m$. Let $\Gamma_s = \{(x_i,v_i),\ i = 1,\dots,m\}$ be the graph of f_S in $S\times\mathbb{R}$; we may assume that the convex envelope $\mathsf{co}[\Gamma_s] \subset \mathbb{R}^n\times\mathbb{R}$ of Γ_s is an $n+1$-dimensional convex polytope; otherwise there will be a single affine function as in Lemma 4.3 satisfying $\ell_s(x_i) = v_i$, and we are back to the situation of Theorem 4.5.

Let $D = \mathsf{co}[S] \subset \mathbb{R}^n$ and $\Gamma = \partial\,\mathsf{co}[\Gamma_s]$ be the boundary of the convex polytope $\mathsf{co}[\Gamma_s]$. We have the following result.

Lemma 4.9. *Let S, f_S, and Γ_s be as defined above. Then the following hold:*

(i) *There are two continuous piecewise affine functions $p_+(x)$ and $p_-(x)$ in $D = \mathsf{co}[S]$ defined by*

$$\begin{aligned} p_+(x) &= \max\{v,\ (x,v)\in\mathsf{co}[\Gamma_s]\}\\ &= \max\left\{\sum_{i=1}^m \lambda_i v_i,\ x_i\in S,\ \lambda_i\ge 0,\ i=1,\dots,m,\ \sum_{i=1}^m\lambda_i = 1,\ \sum_{i=1}^m\lambda_i x_i = x\right\},\\ p_-(x) &= \min\{v,\ (x,v)\in\mathsf{co}[\Gamma_s]\}\\ &= \min\left\{\sum_{i=1}^m \lambda_i v_i,\ x_i\in S,\ \lambda_i\ge 0,\ i=1,\dots,m,\ \sum_{i=1}^m\lambda_i = 1,\ \sum_{i=1}^m\lambda_i x_i = x\right\}, \end{aligned}$$

where p_+ and p_- are piecewise affine concave and convex functions in D, respectively.

(ii) *For every $x \in \mathring{D}$, the interior of D, $p_-(x) < p_+(x)$.*

(iii) *The convex polytope $D\subset\mathbb{R}^n$ has two decompositions $D = \cup_{i=1}^k D_i^+$ and $D = \cup_{j=1}^l D_j^-$ such that D_k^+ and D_j^- are closed convex n-dimensional polytopes, $\mathring{D}_i^+\cap\mathring{D}_j^+ = \varnothing$, and $\mathring{D}_i^-\cap\mathring{D}_j^- = \varnothing$ for $1\le i\ne j\le l$. On each D_k^+ (respectively, D_j^-), $p_+(x)$ (respectively, $p_-(x)$) is an affine function, that is, $p_+(x) := \ell_k^+(x) = a_k^+\cdot x + b_k^+$, $x\in D_k^+$ (respectively, $p_-(x) := \ell_j^-(x) = a_j^-\cdot x + b_j^-$, $x\in D_j^-$). Furthermore, the affine*

function $\ell_k^+(x)$ (respectively, $\ell_j^-(x)$), defined in $\mathbb{R}^n$ as above, satisfies $\ell_k^+(x) \geq p_+(x)$ (respectively, $\ell_j^-(x) \leq p_-(x)$) for $x \in D$.

(iv) *Let $S_k^+ \subset D_k^+$ be the set of all vertices of D_k^+ for $k = 1, \dots, m$; then $S_k^+ \subset S$, and $\cup_{k=1}^m S_k^+ = S$. On each S_k^+, $p_+(x) = f_S(x)$.*

(v) *Let $S_j^- \subset D_j^-$ be the set of all vertices of D_j^- for $j = 1, \dots, l$; then $S_j^- \subset S$, and $\cup_{j=1}^l S_j^- = S$. On each S_k^-, $p_-(x) = f_S(x)$.*

Remark 4.10. In Lemma 4.9, the piecewise affine functions p_+ and p_- are replacements of ℓ_s in Theorem 4.5. For the average approximation, the average $\frac{p_+ + p_-}{2}$ of the piecewise affine functions p_+ and p_- gives the new interpolation formula in $D = \mathsf{co}[S]$, replacing the affine function ℓ_S. This means that our interpolation $A_\lambda^M(f_K)$ might introduce extra nodes in $\mathsf{co}[S]$ in a unique way, in the sense that D is the union of q n-dimensional convex polytopes D_i^{av}, $i \in \{1, \dots, q\}$, such that $\frac{p_+ + p_-}{2}$ is affine on each D_i^{av} but not all vertices of D_i^{av} are contained in S.

The following is a generalization of Theorem 4.5.

Theorem 4.11. *Let $K = \{x_i\}_{i=1}^m \subset \mathbb{R}^n$ be a finite set with distinct points, and let $f_K : K \to \mathbb{R}$ be a function with Lipschitz constant $L > 0$ and bound $A_0 > 0$, that is, $|f(x)| \leq A_0$ for $x \in K$. Suppose $S = \{x_1, x_1, \dots, x_m\} \subset K$ generates a Delaunay cell $\mathsf{co}[S]$ satisfying $\dim(\mathsf{co}[S]) = n$ and $\dim(\mathsf{co}[\Gamma_s]) = n + 1$, where $\Gamma_s = \{(x, f_K(x)),\ x \in S\}$ is the graph of f_K restricted to S. Let $B(y_s; r_s)$ be the associated open ball of the cell $\mathsf{co}[S]$. Let $p_+ : \mathsf{co}[S] \to \mathbb{R}$ be the piecewise affine concave function and $p_- : \mathsf{co}[S] \to \mathbb{R}$ be the piecewise affine convex function defined in Lemma 4.9, and let $\mathsf{co}[S] = \cup_{k=1}^m D_k^+$ and $\mathsf{co}[S] = \cup_{j=1}^l D_j^-$ be the decompositions of $\mathsf{co}[S]$ given by Lemma 4.9. Let*

$$C_s^+ L = \max_{1 \leq k \leq m} C_k^+ L, \quad C_s^- L = \max_{1 \leq j \leq l} C_j^- L, \quad C_s L = \max\{C_s^+ L, C_s^- L\},$$

where $C_k^+ L$ and $C_j^- L$ are the positive upper bounds given by Lemma 4.3 for $|Dp_+(x)|$ and $|Dp_-(x)|$, respectively, on D_k^+ and D_j^-. Let $\sigma_s = \min\{|x - x_s| - r_s,\ x \in K \setminus S\} > 0$. Then for every $x \in \mathsf{co}[S]$,

(4.6)
$$C_\lambda^u(f_K^{-M})(x) = \lambda|x - x_s|^2 - \lambda r_s^2 + p_+(x), \qquad C_\lambda^l(f_K^M)(x) = \lambda r_s^2 - \lambda|x - x_s|^2 + p_-(x),$$
$$A_\lambda^M(f_K)(x) = \frac{p_+(x) + p_-(x)}{2}$$

whenever

$$\lambda > \frac{2A_0}{\sigma_s(2r_s + \sigma_s)} + \frac{C_s L}{\sigma_s} \tag{4.7}$$

and

$$M > \lambda r_s^2 + C_s L r_s + A_0 + \frac{C_s^2 L^2}{4\lambda}. \tag{4.8}$$

Remark 4.12. Under the assumptions of Lemma 4.9 and Theorem 4.11, we see that $p_+(x)$ and $p_-(x)$ are the maximal and minimal piecewise affine interpolations over $\mathsf{co}[S]$. It is well

known [38] that in this irregular case, there still exist Delaunay triangulations of $\mathsf{co}[S]$ consisting of n-dimensional simplices, but the triangulation is not unique. The average approximation

$$A_\lambda^M(f_K)(x) = \frac{p_+(x) + p_-(x)}{2}$$

given by Theorem 4.11 is exactly the average of the maximal and minimal interpolations in a Delaunay cell.

5. Inpainting revisited. Consider now inpainting of damaged areas of an image. This is the problem where we are given an image that is damaged in some parts and we want to reconstruct the values in the damaged part on the basis of the known values of the image. To specify the setting of the problem, let $\Lambda \subset \mathbb{R}^n$ be a convex compact set representing the domain of the image f which, without loss of generality, we assume to be a grayscale image, and which is thus represented by a function $f : \Lambda \subset \mathbb{R}^n \to \mathbb{R}$. We assume that f is bounded and uniformly continuous. See Remark 5.2 and the comments on Example 5.3 for a discussion of this assumption in the case of an image.

Denote by $\Omega \subset \Lambda$ an open set representing the damaged areas of the image, and let $K = \Lambda \setminus \Omega$. We have then $\Omega \subset \mathsf{co}[K]$.

On the basis of the values of f in K, we reconstruct the values of f in Ω by using the average approximation $A_\lambda^M(f_K)$. In this section, we want to assess the error of this approximation.

The next result, which follows from an application of Corollary 2.7, is the main error estimate for our inpainting method.

Proposition 5.1. *Let $\Lambda \subset \mathbb{R}^n$ be a convex compact set and $\Omega \subset \Lambda$ a nonempty open set. Assume $f : \Lambda \subset \mathbb{R}^n \to \mathbb{R}$ is bounded and uniformly continuous, such that for $A_0 > 0$ we have that $|f(x)| \le A_0$ for all $x \in K = \Lambda \setminus \Omega$. Let $\tilde{f}$ be a bounded and uniformly continuous extension of f to $\mathbb{R}^n$, derived by the Tietze extension theorem, with $\tilde{f}(x) = c_0$ outside an open ball $B(0;r)$ with $r > 0$ and such that $K \subset B(0;r)$. For $R > r$, define $K_R = K \cup B^c(0;R)$, and let $f_{K_R}(x) = f_K(x)$ for $x \in K$ and $f_{K_R}(x) = c_0$ for $x \in B^c(0;R)$. Denote by ω the least concave majorant of the modulus of continuity of $\tilde{f}$. Let $a \ge 0$, $b \ge 0$ be such that $\omega(t) \le at + b$ for $t \ge 0$. Then for all $\lambda > 0$, $M > A_0 + \lambda(R+r)^2$, and all $x \in \mathsf{co}[K]$, we have*

$$|A_\lambda^M(f_K)(x) - \tilde{f}(x)| \le \omega\left(r_c(x) + \frac{a}{\lambda} + \sqrt{\frac{2b}{\lambda}}\right), \tag{5.1}$$

where $r_c(x) \ge 0$ is the convex density radius of x with respect to K.

If we further assume that f is a globally Lipschitz function with Lipschitz constant $L > 0$, then for $\lambda > 0$, $M > A_0 + \lambda(R+r)^2$, and all $x \in \mathsf{co}[K]$, we have

$$|A_\lambda^M(f_{K_R})(x) - f(x)| \le L r_c(x) + \frac{L^2}{\lambda}. \tag{5.2}$$

If we further assume that $\tilde{f}$ is a $C^{1,1}$ function such that $|D\tilde{f}(x) - D\tilde{f}(y)| \le L|x-y|$ for all $x, y \in \mathbb{R}^n$ with $L > 0$ the Lipschitz constant of $D\tilde{f}$, then for $\lambda > L$, $M > A_0 + \lambda(R+r)^2$, and all $x \in \mathsf{co}[K]$, we have

$$|A_\lambda^M(f_{K_R})(x) - \tilde{f}(x)| \le \frac{L}{4}\left(\frac{\lambda + L/2}{\lambda - L/2} + 1\right) r_c^2(x). \tag{5.3}$$

Furthermore, in this case, $A_\lambda^M(f_{K_R})$ *is an interpolation of* f_K *in* $\mathbb{R}^n$.

Remark 5.2.

(i) Using (2.9), it follows that the estimates (5.1) and (5.3) hold with $r_c(x)$ replaced by $d(x)$. Although the resulting estimates are less sharp, they have a clearer meaning in light of the geometric interpretation of the gap $d(x)$.

(ii) While the assumption of boundedness of the image f is a plausible one, the assumption on the continuity of f seems to be less reasonable for applications to images which might have sharp changes in grayscale intensity. However, Example 5.3 at the end of this section illustrates the fact that our average approximation operator well approximates jump discontinuities.

It is interesting to compare our error estimates (5.1) and (5.3) with the error analysis for image inpainting discussed in [15]. Let $\Omega \subset \mathbb{R}^2$ be a smooth domain, which is the damaged area of the image to be reconstructed, and let u be a C^2-function in a larger domain containing $\bar{\Omega}$. Let $u_0 = u$ on $\partial\Omega$, and consider the solution v of the boundary value problem $\Delta v(x) = 0$ with $v = u_0$ on $\partial\Omega$. The function v is the reconstruction of u within Ω. The error estimate obtained in [15] is then given by

$$|v(x) - u(x)| \leq \frac{T\beta^2}{4}, \quad x \in \Omega\,, \tag{5.4}$$

where $T = \max\{|\Delta u(x)|,\ x \in \bar{\Omega}\}$ and β is the shorter semiaxis of any ellipse covering Ω. Reference [15] also contains variations of estimate (5.4) by deforming (if possible) a general long thin domain into one for which β is reasonably small.

Note that in light of Remark 5.2(i), the error bound (5.3) depends explicitly on $d(x)$ and the Lipschitz constant L of the gradient $D\tilde{f}$, which is comparable with the bound T for the Laplacian of u. Moreover, our assumptions on the smoothness of the domain Ω and the underlying function are weaker than those considered in [15]. In fact, we do not require any smoothness of the boundary $\partial\Omega$. Our estimate is particularly sharp for more general thin domains given its dependence on $d(x)$. As noted in [15], the short semiaxis β^2 used in the error estimate for harmonic inpainting cannot be replaced by $d^2(x)$ which better accounts for the geometric structure of the damaged area to be inpainted. Due to the Hausdorff stability property of the average approximation (see [55, Theorem 4.12]), if Ω_ϵ is another domain whose Hausdorff distance to Ω is small, we can also obtain similar results to estimate (5.3) for such domains.

Reference [15] also contains error estimates for the TV inpainting model using the energy $\int_\Omega |v(x)|dx$ under the Dirichlet condition $v|_{\partial\Omega} = u_0$. However, it is not clear how such estimates can be made rigorous. Compared with Proposition 5.1, where we assumed the underlying function to be bounded and uniformly continuous, the TV model, in contrast, allows the function to have jumps; thus the TV inpainting model tries to preserve such jump discontinuities. However, such a model cannot be Hausdorff stable. Also, in order to establish the existence of solutions for this model, we note that the boundary condition has to be relaxed. Even for the more regular minimal graph energy $\int_\Omega \sqrt{1 + |Dv(x)|^2}dx$, existence of solutions for the Dirichlet problem may not be guaranteed [31]. On the other hand, the average approximation always exists and is unique. See Example 6.5 in section 6 for an illustration of

this.

Compared with our model for inpainting, we also note that for the relaxed Dirichlet problem of the minimal graph or of the TV model, as the boundary value of the solution does not have to agree with the original boundary value, extra jumps can be introduced along the boundary. By comparison, since our average approximation is continuous, it will not introduce such a jump discontinuity at the boundary.

One of the motivations for using TV related models [17] for the inpainting problem is that functions of bounded variations can have jump discontinuities [3]. Some authors argue that continuous functions cannot be used to model digital image related functions as functions representing images may have jumps [17]. However, from the human vision perspective, it is hard to distinguish between a jump discontinuity, where values change abruptly, and a continuous function with sharp changes within a very small transition layer. The following is a simple one-dimensional example showing the effects of our upper, lower, and average compensated convex transforms on a jump function. More explicitly calculated prototype examples of inpainting by using our method over jump discontinuity and continuous edges are given in section 6.

Example 5.3. Let $f(x) = \operatorname{sign}(x)$ be the sign function defined by $\operatorname{sign}(x) = 1$ if $x > 0$ and $\operatorname{sign}(x) = -1$ if $x < 0$. For $\lambda > 0$, we have

$$
\begin{aligned}
C_\lambda^l(f)(x) &= \begin{cases} -1, & x \le 0, \\ 1 - \lambda(x - \sqrt{2/\lambda})^2, & 0 \le x \le \sqrt{2/\lambda}, \\ 1, & x \ge \sqrt{2/\lambda}, \end{cases} \\
C_\lambda^u(f)(x) &= \begin{cases} -1, & x \le -\sqrt{2/\lambda}\,, \\ \lambda(x + \sqrt{2/\lambda})^2 - 1, & -\sqrt{2/\lambda} \le x \le 0\,, \\ 1, & x \ge 0, \end{cases} \qquad (5.5) \\
\frac{1}{2}(C_\lambda^l(f)(x) + C_\lambda^u(f)(x)) &= \begin{cases} -1, & x \le -\sqrt{2/\lambda}, \\ \frac{\lambda}{2}(x + \sqrt{2/\lambda})^2 - 1, & -\sqrt{2/\lambda} \le x \le 0, \\ 1 - \frac{\lambda}{2}(x - \sqrt{2/\lambda})^2, & 0 \le x \le \sqrt{2/\lambda}, \\ 1, & x \ge \sqrt{2/\lambda}. \end{cases}
\end{aligned}
$$

Figure 1 displays the graphs of these transforms with $\lambda = 100$, which give very good approximations of the jump function with the square of the L^2-error equal to $2\sqrt{2}/(5\sqrt{\lambda})$ for the average approximation and equal to $\sqrt{2}/(5\sqrt{\lambda}$ for the lower and upper transforms. Therefore, these transforms can be used quite effectively to replace the jump discontinuity. For further prototype examples of inpainting with jump discontinuity, see section 6.

We conclude this section by presenting a result on inpainting in bounded convex domains which we state only for continuous functions defined on the closure of the domain. For Lipschitz and $C^{1,1}$-functions, similar results can be established.

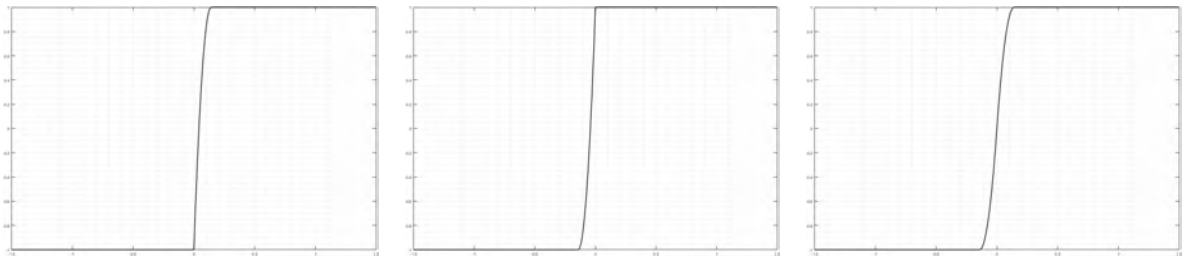

(a) (b) (c)

Figure 1. (a) *Lower transform of the sign function for* $\lambda = 100$. (b) *Upper transform of the sign function for* $\lambda = 100$. (c) *Average approximation of the sign function for* $\lambda = 100$.

Corollary 5.4. *Suppose* $\Omega \subset \mathbb{R}^n$ *is a nonempty, bounded, open, and convex set and* $U \subset \bar{U} \subset \Omega$ *is an open subset whose closure* $\bar{U}$ *is contained in* Ω. *Suppose* $f : \bar{\Omega} \to \mathbb{R}$ *is a continuous function. Let* $\tilde{f}$ *be any bounded uniformly continuous extension of* f *to* $\mathbb{R}^n$ *and* ω *be the least concave majorant of the modulus of continuity of* $\tilde{f}$ *which is itself a modulus of continuity. Let* $K = \bar{\Omega} \setminus U$ *and define for* $M > 0$

$$f_K^{M,\infty}(x) = \begin{cases} f(x), & x \in K, \\ M, & x \in U, \\ +\infty, & x \in \mathbb{R}^n \setminus \bar{\Omega}, \end{cases} \qquad f_K^{-M,-\infty}(x) = \begin{cases} f(x), & x \in K, \\ -M, & x \in U, \\ -\infty, & x \in \mathbb{R}^n \setminus \bar{\Omega}. \end{cases}$$

Then the average approximation in $\bar{\Omega}$ *defined by*

$$A_\lambda^{M;\infty}(f_K)(x) = \frac{1}{2}\left(C_\lambda^l(f_K^{M,+\infty})(x) + C_\lambda^u(f_K^{-M,-\infty})(x)\right) \tag{5.6}$$

for $x \in \bar{\Omega}$ *satisfies*

$$|A_\lambda^{M,\infty}(f_K)(x) - f(x)| \le \omega(r_c(x) + a/\lambda + \sqrt{b/\lambda})$$

for all $x \in \bar{\Omega}$, *where* $r_c(x)$ *is the convex density radius of* $x \in \bar{\Omega}$ *with respect to* K.

Remark 5.5. The average approximation defined by (5.6) is the same average approximation as defined on the bounded domain $\bar{\Omega}$,

$$A_\lambda^M(f_K; \bar{\Omega})(x) = \frac{1}{2}\left(C_\lambda^l(f_K^M; \bar{\Omega})(x) + C_\lambda^u(f_K^{-M}; \bar{\Omega})(x)\right)$$

for $x \in \bar{\Omega}$, where $f_K^M(x)$ and $f_K^{-M}(x)$ are defined by (1.2), restricted to $\bar{\Omega}$. We can also state the average approximation under the Dirichlet boundary condition in a similar way. We leave this to interested readers.

6. Prototype models.

In this section we present explicitly calculated average approximations for some particular simple functions of two variables. Recall that such approximations $A_\lambda^\infty(f_K)$ are obtained by first finding lower and upper compensated convex transforms and then taking their arithmetic mean, and that the approximation properties of $A_\lambda^\infty(f_K)$ hold for $(x, y) \in \mathsf{co}[K]$. For some examples we also give expressions for the constituent lower and

upper transforms to help illustrate the construction of the approximations. Such examples serve the dual purpose of providing insight into this new class of approximations based on compensated convexity transforms, and of verifying numerical methods for computing such approximations. In fact, in section 7 below, we will see numerical examples that show that, at a sufficient level of magnification, the conditions that occur in practice for the approximation of general functions often look essentially like one of these prototypes.

6.1. Simple prototypes.

Example 6.1. These two examples give average approximations $A_\lambda^\infty(f_K)$ for simple sampled functions over nonregular Delaunay cells. In each case, the average approximation is an interpolation of the sampled function values.

(i) Consider the four-point set $K = \{(\pm 1, 0), (0, \pm 1)\}$, and define $f_K(1,0) = f_K(0,1) = 1$ and $f_K(-1,0) = f_K(0,-1) = -1$. The upper and lower compensated convex transforms are then, for $\lambda > 0$,

$$C_\lambda^l(f_K^\infty)(x,y) = \begin{cases} 2\lambda - 1 - x + y - \lambda(x^2+y^2) & \text{if } x \geq -1,\ y \leq 1 \text{ and } x \leq y, \\ 2\lambda - 1 + x - y - \lambda(x^2+y^2) & \text{if } y \geq -1,\ x \leq 1 \text{ and } x \geq y, \\ +\infty & \text{if } |x| > 1 \text{ or } |y| > 1, \end{cases}$$

$$C_\lambda^u(f_K^{-\infty})(x,y) = \begin{cases} -2\lambda + 1 + x + y + \lambda(x^2+y^2) & \text{if } x \geq -1,\ y \geq -1, \text{ and } x + y \leq 0, \\ -2\lambda + 1 - x - y + \lambda(x^2+y^2) & \text{if } x \leq 1,\ y \leq 1, \text{ and } x + y \geq 0, \\ -\infty & \text{if } |x| > 1 \text{ or } |y| > 1, \end{cases}$$

so that, for $(x,y) \in D := \mathsf{co}[K] = \{(x,y) \in \mathbb{R}^2 :\ |x| \leq 1,\ |y| \leq 1\}$, we have

$$A_\lambda^\infty(f_K)(x,y) = \begin{cases} y & \text{if } x \leq y \text{ and } x + y \leq 0, \\ -x & \text{if } x \leq y \text{ and } x + y \geq 0, \\ x & \text{if } x \geq y \text{ and } x + y \leq 0, \\ -y & \text{if } x \geq y \text{ and } x + y \geq 0. \end{cases}$$

This is the continuous piecewise affine interpolation of f_K inside the square D. The graph of $A_\lambda^\infty(f_K)$ is shown in Figure 2(a).

(ii) Consider the eight-point set $K \subset \mathbb{R}^2$ consisting of the eight points on the unit circle with polar angles $k\pi/4$, $k = 0, 1, 2, \ldots, 7$, and define $f_K(\cos(k\pi/4), \sin(k\pi/4)) =$

$(-1)^k$. The upper and lower compensated convex transforms are then, for $\lambda > 0$,

$$C^l_\lambda(f^\infty_K)(x,y) = \begin{cases} \frac{\sqrt{2}+1}{\sqrt{2}-1} - \frac{2|y|}{\sqrt{2}-1} & \text{if } |x| \le 1,\ |y| \ge 1, \text{ and } |y| + (\sqrt{2}-1)|x| \le \sqrt{2}, \\ \frac{\sqrt{2}+1}{\sqrt{2}-1} - \frac{2|x|}{\sqrt{2}-1} & \text{if } |y| \le -1,\ |x| \ge 1, \text{ and } |x| + (\sqrt{2}-1)|y| \le \sqrt{2}, \\ 1 & \text{if } |x| \le 1 \text{ and } |y| \le 1, \\ 0 & \text{otherwise,} \end{cases}$$

$$C^u_\lambda(f^{-\infty}_K)(x,y) = \begin{cases} \frac{\sqrt{2}+1}{\sqrt{2}-1} - \frac{\sqrt{2}|x-y|}{\sqrt{2}-1} & \text{if } |x+y| \le \sqrt{2},\ |x-y| \ge \sqrt{2}, \text{ and} \\ & \quad |x-y| + (\sqrt{2}-1)|x+y| \le 2, \\ \frac{\sqrt{2}+1}{\sqrt{2}-1} - \frac{\sqrt{2}|x+y|}{\sqrt{2}-1} & \text{if } |x+y| \ge \sqrt{2},\ |x+y| \ge \sqrt{2}, \text{ and} \\ & \quad |x+y| + (\sqrt{2}-1)|x-y| \le 2, \\ 1 & \text{if } |x+y| \le \sqrt{2} \text{ and } |x-y| \le \sqrt{2}, \\ 0 & \text{otherwise,} \end{cases}$$

whereas $A^\infty_\lambda(f_K)(x,y)$ is obtained by taking the arithmetic mean of $C^l_\lambda(f^\infty_K)(x,y)$ and $C^u_\lambda(f^{-\infty}_K)(x,y)$. Figure 2(b) shows the graph of $A^\infty_\lambda(f_K)$ in $\mathsf{co}[K]$, which is the inside of the regular octagon with vertices at the eight points of K. As in (i), $A^\infty_\lambda(f_K)$ is a continuous piecewise affine interpolation of f_K in $\mathsf{co}[K]$.

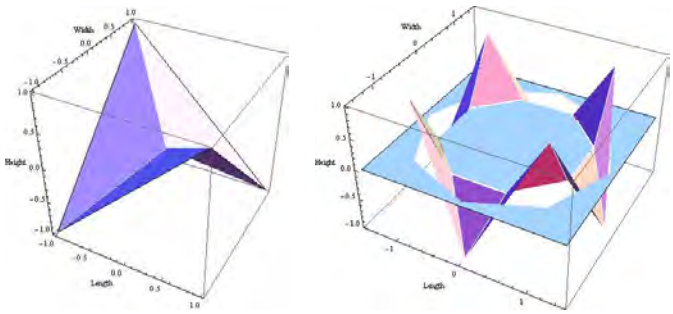

(a) (b)

Figure 2. *Graphs of the average approximation operators $A^\infty_\lambda(f_K)$ in Example 6.1, when K is* (a) *a four point set on the circle of unit radius and* (b) *an eight point set on the circle of unit radius. In both* (a) *and* (b)*, the average approximation operator is an interpolation operator over* $\mathsf{co}[K]$.

Example 6.2. These two examples give average approximations $A^\infty_\lambda(f_K)$ for unbounded sets K with $\mathsf{co}[K] = \mathbb{R}^2$.

(i) Consider the set $K = \ell_- \cup \ell_+$ with $\ell_- = \{(x,x),\ x \in \mathbb{R}\}$, $\ell_+ = \{(y,-y),\ y \in \mathbb{R}\}$, and define $f_K(x,x) = -x^2$ and $f_K(y,-y) = y^2$. To simplify the calculations, first consider the scaled and rotated function $g_{\tilde{K}}$ defined on the set $\tilde{K} = \{(x,0), x \in \mathbb{R}\} \cup \{(0,y), y \in \mathbb{R}\}$, with $g_{\tilde{K}}(x,0) = -x^2$ and $g_{\tilde{K}}(0,y) = y^2$. Then, for $(x,y) \in \mathbb{R}^2$, the lower and upper compensated convex transforms of $g_{\tilde{K}}$ are

$$C^l_\lambda(g^\infty_{\tilde{K}})(x,y) = y^2 + 2|x||y| - x^2, \qquad C^u_\lambda(g^{-\infty}_{\tilde{K}})(x,y) = y^2 - 2|x||y| - x^2,$$

and the average approximation of $g_{\tilde{K}}$ is

$$A_\lambda^\infty(g_{\tilde{K}})(x,y) = \frac{1}{2}\left(C_\lambda^l(g_{\tilde{K}}^\infty)(x,y) + C_\lambda^u(g_{\tilde{K}}^{-\infty})(x,y)\right) = y^2 - x^2\,.$$

The average approximation $A_\lambda^\infty(f_K)$ of f_K is then obtained from $A_\lambda^\infty(g_{\tilde{K}})$ via a change of variables and is

$$A_\lambda^\infty(f_K)(x,y) = \frac{1}{2}\left(A_\lambda^\infty(g_{\tilde{K}})\left(\frac{x+y}{\sqrt{2}}, \frac{x-y}{\sqrt{2}}\right)\right) = -xy\,.$$

Figure 3(a) shows the graph of $A_\lambda^\infty(f_K)$.

(ii) Let $K = \{(x,0),\, x \in \mathbb{R}\} \cup \{(0,y),\, y \in \mathbb{R}\}$, and define f_K by $f_K(x,0) = |x|$ for $x \in \mathbb{R}$ and $f_K(0,y) = -|y|$ for $y \in \mathbb{R}$. For $(x,y) \in \mathbb{R}^2$, the lower and upper compensated convex transforms of f_K are

$$C_\lambda^l(f_K^\infty)(x,y) = \begin{cases} 2|x| - \frac{1}{4\lambda} - \lambda(x^2+y^2) & \text{if } |x|+|y| \le \frac{1}{2\lambda}, \\ |x| + 2\lambda|x||y| - |y| & \text{if } |x|+|y| \ge \frac{1}{2\lambda}, \end{cases}$$

$$C_\lambda^u(f_K^{-\infty})(x,y) = \begin{cases} -2|y| + \frac{1}{4\lambda} + \lambda(x^2+y^2) & \text{if } |x|+|y| \le \dfrac{1}{2\lambda}, \\ |x| - 2\lambda|x||y| - |y| & \text{if } |x|+|y| \ge \dfrac{1}{2\lambda}, \end{cases}$$

and the average approximation operator is

$$A_\lambda^\infty(f_K)(x,y) = |x| - |y|\,,$$

which here coincides with the natural interpolation of f_K by the piecewise affine function $f(x,y) = |x| - |y|$, $(x,y) \in \mathbb{R}^2$. The graph of $A_\lambda^\infty(f_K)$ is shown in Figure 3(b).

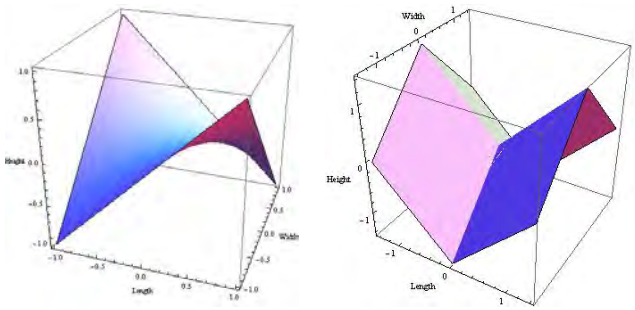

(a) (b)

Figure 3. *Graphs of the average approximation operators $A_\lambda^\infty(f_K)$ in Example 6.2*(i) *and* (ii)*, respectively.*

6.2. Inpainting prototypes. Examples 6.3 and 6.4 are prototype models for the inpainting problem. Our question is to what extent our method can preserve singularities on the boundary based on the given boundary values. Our calculations show that if the domain is narrow and similar singular boundary values appear on both sides of the narrow gap, the inpainting function $A_\lambda^\infty(f_K)$ can preserve the singular shape across the gap, subject to a λ-dependent regularization of the singularity due to the local smoothing effect of the compensated convex transforms.

Example 6.3.

(i) For $r > 0$, $h > 0$, let $K = \{(\pm r, y),\ |y| \le h\} \subset \mathbb{R}^2$, i.e., two parallel line segments a distance r apart (see Figure 4(a)), and define $f_K(\pm r, y) = 1 - |y|$. Let $D = \mathsf{co}[K] = \{(x, y) \in \mathbb{R}^2 :\ |x| \le r,\ |y| \le h\}$. Then for $\lambda > 1/2h$,

$$C_\lambda^l(f_K^\infty)(x,y) = \begin{cases} 1 - \frac{1}{4\lambda} + \lambda r^2 - \lambda x^2 - \lambda y^2 & \text{if } |x| \le r \text{ and } |y| \le \frac{1}{2\lambda}, \\ 1 + \lambda r^2 - \lambda x^2 - |y| & \text{if } |x| \le r \text{ and } \frac{1}{2\lambda} \le |y| \le h, \\ +\infty & \text{otherwise,} \end{cases}$$

$$C_\lambda^u(f_K^{-\infty})(x,y) = \begin{cases} 1 - \lambda r^2 + \lambda x^2 - |y| & \text{if } |x| \le r \text{ and } |y| \le h, \\ -\infty & \text{otherwise,} \end{cases}$$

and for $(x, y) \in D$, the average approximation operator is

$$A_\lambda^\infty(f_K)(x,y) = \begin{cases} 1 - \frac{1}{8\lambda} - \frac{\lambda y^2}{2} - \frac{|y|}{2} & \text{if } |x| \le r \text{ and } |y| \le \frac{1}{2\lambda}, \\ 1 - |y| & \text{if } |x| \le r \text{ and } \frac{1}{2\lambda} \le |y| \le h\,. \end{cases}$$

The graph of $A_\lambda^\infty(f_K)$ is shown in Figure 4(b).

Note that this example shows that if we only sample the two gables K of the roof, the whole roof can be recovered well for any $r > 0$ and $h > 0$. On the other hand, we will see in the next example that the situation is more complicated if the other two sides, $(x, \pm h)$ for $|x| \le r$, are added to the sample set.

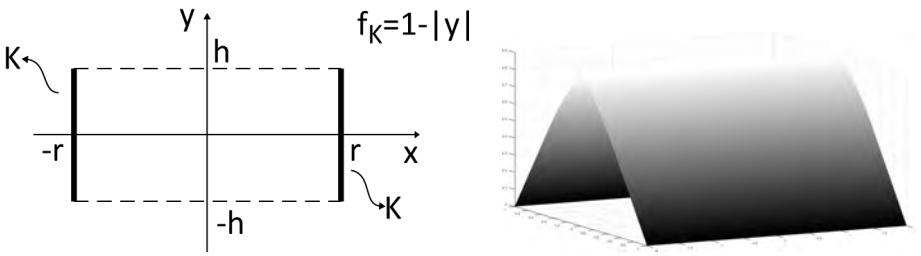

(a) (b)

Figure 4. *Example* 6.3(i). (a) *The sample set K shown in bold, with the sample function $f_K = 1 - |y|$.* (b) *Graph of $A_\lambda^\infty(f_K)$ for $\lambda = 1$.*

(ii) Next let $D = \{(x, y),\ |x| \le r,\ |y| \le h\}$ with $h > 0$ and $r > 0$, take the sample set $K = \partial D = \{(\pm r, y),\ |y| \le h\} \cup \{(x, \pm h),\ |x| \le r\}$, and define

$$f_K(x,y) = \begin{cases} h - |y|, & x = \pm r,\ |y| \le h, \\ 0, & y = \pm h,\ |x| \le r. \end{cases}$$

For large λ, the shape of $A_\lambda^\infty(f_K(x, y))$ in D now depends on whether $h > r$, $h < r$, or $h = r$.

(a) If $h > r$, the two gables of the roof $h - |y|$ at $x = \pm r$ are close to each other and we have a very good approximation of the whole roof $h - |y|$ for $(x, y) \in D$ when λ is sufficiently large. For $(x, y) \in D$, the approximation $A^\infty_\lambda(f_K(x, y))$ is

$$A^\infty_\lambda(f_K)(x,y) = \begin{cases} h - \frac{1}{4\lambda} - \lambda y^2 & \text{if } |y| \le \frac{1}{2\lambda} \text{ and } |x| \le r, \\ h - |y| & \text{if } \frac{1}{2\lambda} \le |y| \le h \text{ and } |x| \le r, \end{cases}$$

which yields the explicit error estimate

$$|A^\infty_\lambda(f_K)(x,y) - f(x,y)| \le \tfrac{1}{8\lambda}.$$

In particular, the ridge of the roof is preserved well in this case.

(b) If $h = r$ and $\lambda > 0$ is large, the roof dips in the middle, while the "ridge" is still preserved.

(c) If $h < r$ and $\lambda > 0$ is large, the roof falls inside $D = \mathsf{co}[K]$ and touches the ground. In this case, the ridge is no longer preserved at all.

In summary, the average approximation can approximate well the nonsmooth function given on two sides of K provided the two gables are close enough. In this case, we could say that by symmetry we have a behavior similar to the one seen in Example 6.3(a). On the other hand, when the two gables are far apart, i.e., when $h/r < 1$, having $f_K = 0$ on the sides $y = \pm h$ results in a zero interpolation in the middle of the domain. We stress again that this situation is different from the one seen in Example 6.3(a), where f_K was sampled only on the sides $x = \pm r$. Figure 5 shows the graphs of A^∞_λ in each of the three cases, together with the sample set K.

A preliminary one-dimensional prototype of the inpainting of a region when the boundary values have discontinuities was given in Example 5.3. We next explore how our inpainting method can preserve jumps in a two-dimensional example.

Example 6.4. Consider the inpainting of the region $D = \{(x, y),\ |x| \le r,\ |y| \le h\}$, for r, $h > 0$, in the case of narrow gap, that is, when $h < r$. The sample set is the boundary of the domain D, that is, $K = \partial D$, and the sample function f_K is taken as $f_K(x, y) = \mathrm{sign}(x)$. The sample set K with the sample function f_K' is shown in Figure 6(b). Then for $\lambda > 0$ large enough, the average approximation operator is in fact given by (5.5), that is, for $(x, y) \in D$,

$$A^\infty_\lambda(f_K)(x,y) = \begin{cases} -1 & \text{if } x \le -\sqrt{2/\lambda} \text{ and } |y| \le h\,, \\ \frac{\lambda}{2}(x + \sqrt{2/\lambda})^2 - 1 & \text{if } -\sqrt{2/\lambda} \le x \le 0 \text{ and } |y| \le h\,, \\ 1 - \frac{\lambda}{2}(x - \sqrt{2/\lambda})^2 & \text{if } 0 \le x \le \sqrt{2/\lambda} \text{ and } |y| \le h\,, \\ 1 & \text{if } x \ge \sqrt{2/\lambda} \text{ and } |y| \le h\,. \end{cases}$$

Figure 6(a) shows the graph of the average approximation $A^\infty_\lambda(f_K)$ in this case. The approximation $A^\infty_\lambda(f_K)(x, y)$ is different from $\mathrm{sign}(x)$ in the range $[-\sqrt{2/\lambda}, \sqrt{2/\lambda}] \times [-h, h]$ due to the smoothing effect of the compensated transform in the neighborhood of the singularity. The width of such a neighborhood depends on $\sqrt{\lambda}^{-1}$. The full recovery of the sign function in D requires taking the limit $\lim_{\lambda\to\infty} A^\infty_\lambda(f_K)(x, y)$.

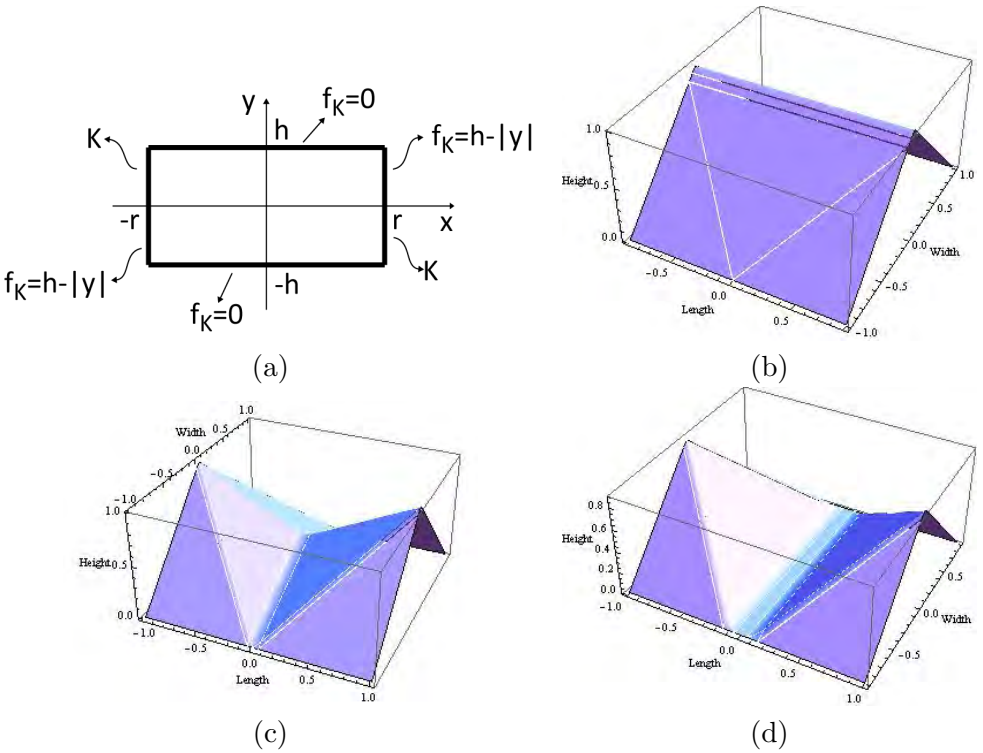

Figure 5. *Example* 6.3(ii). (a) *The sample set K shown in bold, with the sample function f_K. Average approximation in D for the following parameters:* (b) $h = 1$, $r = 0.9$, $\lambda = 10$. (c) $h = 1$, $r = 1$, $\lambda = 10$. (d) $h = 0.9$, $r = 1$, $\lambda = 10$.

Note that if, on the other hand, $h > r$, the gap is "wide" and the graph of $A_\lambda^\infty(f_K)$ starts to collapse in the middle of the domain, similar to what happens in Example 6.3(ii)(c). In the collapsed region, the approximation looks like an affine function connecting the two sides $\{x = \pm r\}$ of D on which f_K is given by the constants $+1$, when $x = +r$, and -1, when $x = -r$.

6.3. Level-set prototypes. We next present prototype models for the approximation of functions sampled on contour lines.

Example 6.5. This example examines the behavior of $A_\lambda^\infty(f_K)$ when the contour lines of f are (i) smooth and (ii) not smooth.

(i) For $0 < r < R$, let $K = \Gamma_r \cup \Gamma_R$ with Γ_r and Γ_R circles of radius r and R, respectively, as displayed in Figure 7(a), and define the sample function f_K by $f_K(x, y) = 0$ for

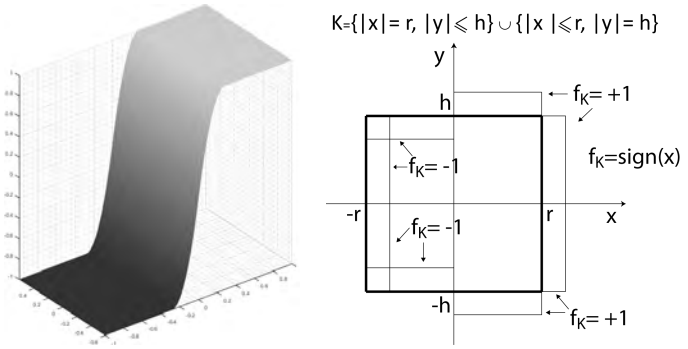

(a) (b)

Figure 6. *Example 6.4. Inpainting in the closed set* $D = \{(x, y),\ |x| \le l,\ |y| \le h\}$ *by the boundary value of the sign function on the sample set* $K = \partial D$. (a) *Graph of* $A_\lambda^\infty(f_K)$ *for* $h = 0.6$, $r = 1$, $\lambda = 25$, *showing that the jump is preserved across the domain* D. (b) *Sample set* K *shown in bold with the sampled function* $f_K = \text{sign}(x)$.

$(x, y) \in \Gamma_r$ and $f_K(x, y) = M > 0$ if $(x, y) \in \Gamma_R$. Then for $\lambda > M/(R^2 - r^2)$,

$$C_\lambda^u(f_K^{-\infty})(x,y) = \begin{cases} M + \lambda(x^2 + y^2 - r^2) & \text{if } \sqrt{x^2+y^2} \le r, \\ \lambda(x^2 + y^2 - R^2) + \frac{M+\lambda(R^2-r^2)}{R-r}(R - \sqrt{x^2+y^2}) & \text{if } r \le \sqrt{x^2+y^2} \le R, \end{cases}$$

$$C_\lambda^l(f_K^{\infty})(x,y) = \begin{cases} M + \lambda(r^2 - x^2 - y^2) & \text{if } \sqrt{x^2+y^2} \le r, \\ \lambda(R^2 - x^2 - y^2) - \frac{\lambda(R^2-r^2)-M}{R-r}(R - \sqrt{x^2+y^2}) & \text{if } r \le \sqrt{x^2+y^2} \le R, \end{cases}$$

so that for $(x, y) \in D = \mathsf{co}[K] = \{(x, y) : x^2 + y^2 \le R^2\}$, the average approximation $A_\lambda^\infty(f_K)$ is

$$A_\lambda^\infty(f_K)(x,y) = \begin{cases} M & \text{if } \sqrt{x^2+y^2} \le r, \\ \frac{M(R-\sqrt{x^2+y^2})}{R-r} & \text{if } r \le \sqrt{x^2+y^2} \le R. \end{cases}$$

The graph of $A_\lambda^\infty(f_K)$ is shown in Figure 7(b).

Note that a common method for the interpolation of function values assigned on contour lines is to solve the Dirichlet problem for the minimal surface equation $\mathsf{div}\,\frac{Du}{\sqrt{1+|Du|^2}} = 0$ over the annulus domain $r \le \sqrt{x^2+y^2} \le R$ with boundary conditions $u(x, y) = 0$ if $(x, y) \in \Gamma_r$ and $u(x, y) = M$ if $(x, y) \in \Gamma_R$. It is then known that this problem does not have a regular solution [31]. Moreover, the interpolation obtained by solving the total variation equation $\mathsf{div}\,\frac{Du}{|Du|} = 0$ faces the same type of issue, because to obtain its numerical solution, the denominator $|Du|$ is usually replaced by the term $\sqrt{\epsilon^2 + |Du|^2}$, thus obtaining the scaled minimal surface equation $\mathsf{div}\,\frac{Du}{\sqrt{\epsilon+|Du|^2}} = 0$ whose solution, as mentioned above, may not be regular. As a result, these models must be relaxed, and one must look for generalized solutions [30]. In contrast, the method we propose yields the natural, easy to compute, and expected interpolation $A_\lambda^\infty(f_K)$ between the two level lines.

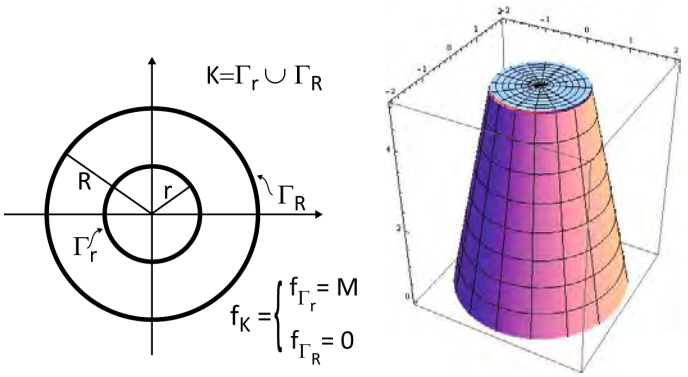

Figure 7. *Example* 6.5(i). (a) *Sample set* K *given by the two circular level lines* Γ_r *and* Γ_R *with* $f_K(x,y)=0$ *for* $(x,y)\in\Gamma_r$ *and* $f_K(x,y)=M>0$ *if* $(x,y)\in\Gamma_R$. (b) *Graph of* $A^\infty_\lambda(f_K)$ *with* $r=1$, $R=2$, $M=5$, *and* $\lambda=10$.

(ii) For $a,\ \lambda>0$, consider the sample set $K=K_1\cup K_2$ with $K_1=\{(x,\ y):\ |y|=ax,\ x\geq 0\}$ and $K_2=\{(x,\ y):\ |y|=a(x-\frac{\sqrt{1+a^2}}{a\sqrt{\lambda}}),\ x\geq\frac{\sqrt{1+a^2}}{a\sqrt{\lambda}}\}$, and define the sample function f_K by $f_K(x,y)=1$ for $(x,y)\in K_1$ and $f_K(x,y)=2$ for $(x,y)\in K_2$. The set K and f_K are shown in Figure 8(a). For $(x,y)\in D=\mathsf{co}[K]=\{(x,y):|y|\leq ax,\ x\geq 0\}$, the average approximation operator $A^\infty_\lambda(f_K)$ is

$$A^\infty_\lambda(f_K)(x,y)=\begin{cases}1 & \text{if } |y|\leq ax \text{ and } 0\leq x\leq \frac{1}{a\sqrt{1+a^2}},\\ 1+\frac{\sqrt{1+a^2}\left(-\frac{1}{a\sqrt{1+a^2}}+x\right)}{a} & \text{if } x\geq\frac{1}{a\sqrt{1+a^2}} \text{ and } \frac{x+a|y|}{\sqrt{1+a^2}}\leq\frac{1}{a\sqrt{\lambda}},\\ 2-\left|\frac{1}{\sqrt{\lambda}}+\frac{-ax+|y|}{\sqrt{1+a^2}}\right| & \text{if } -\frac{1}{\sqrt{\lambda}}\leq\frac{-ax+|y|}{\sqrt{1+a^2}}\leq 0 \text{ and } \frac{1}{a\sqrt{\lambda}}\leq\frac{x+a|y|}{\sqrt{1+a^2}},\\ 2 & \text{if } \frac{-ax+|y|}{\sqrt{1+a^2}}\leq-\frac{1}{\sqrt{\lambda}} \text{ and } x\geq\frac{\sqrt{1+a^2}}{a\sqrt{\lambda}}.\end{cases}$$

The graph of $A^\infty_\lambda(f_K)$ is displayed in Figure 8(b), whereas Figure 8(c) displays its isolines. Note that the interpolation $A^\infty_\lambda(f_K)$ takes the constant value 1, which is the value given on the level set K_1, inside a triangle next to the corner of K_1, which is then pieced continuously to K_2 by a continuous piecewise affine function.

We conclude this section with a prototype example of level set approximation for a function with a jump discontinuity at the point $(0,0)$.

Example 6.6. For $\alpha,\ m>0$, consider the sample set K given by $K=\ell_+\cup\ell_-$ with $\ell_+=\{(x,y),\ y=-\alpha x,\ x>0\}$ and $\ell_-=\{(x,y),\ y=\alpha x,\ x>0\}$, and define $f_K(x,y)=m$ on ℓ_+ and $f_K(x,y)=-m$ on ℓ_+. The set K and f_K are displayed in Figure 9(a). To describe the average approximation of f_K in $\mathsf{co}[K]=\{(x,y),\ |y|\leq\alpha x,\ x>0\}$ which we denote by S_+, we use a parameterized description of the graph $(x,y,A^\infty_\lambda(f_K)(x,y))$ in terms of two new parameters. This is to avoid solving quartic equations when we find the lower and upper transforms. Let $c_\lambda=2m/\lambda$. To calculate the lower transform $C^l_\lambda(f^\infty_K)$ in S_+ we need to find

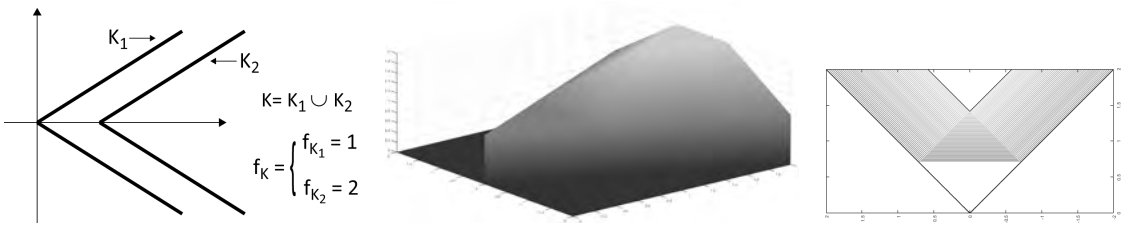

Figure 8. *Example* 6.5(ii). (a) *Sample set* K *given by two nonsmooth level sets* K_1 *and* K_2 *with* $a = 1$ *and* $f_K(x, y) = 0$ *for* $(x, y) \in K_1$ *and* $f_K(x, y) = 2$ *if* $(x, y) \in K_2$. (b) *Graph of* $A^{\infty}_{\lambda}(f_K)$ *with* $\lambda = 1$. (c) *Isolines of* $A^{\infty}_{\lambda}(f_K)$.

the common tangent planes for $f^{\infty}_K(x, y) + \lambda(x^2 + y^2)$ of both ℓ_+ and ℓ_-. We can write the coordinates of the convex envelope as $(x, y, \mathsf{co}[f^{\infty}_K(x, y) + \lambda(x^2 + y^2)])$ by

$$\left(\frac{(1 - t_l)\sqrt{s_l^2 + c_\lambda} + t_l s_l}{\sqrt{1 + \alpha^2}}, \frac{-\alpha(1 - t_l)\sqrt{s_l^2 + c_\lambda} + \alpha t_l s_l}{\sqrt{1 + \alpha^2}}, \lambda s_l^2 + 2\lambda(1 - t_l)c_\lambda - m \right),$$

where $0 \le t_l \le 1$ and $s_l \ge 0$. Similarly, the coordinates of $(x, y, \mathsf{co}[\lambda(x^2 + y^2) - f^{-\infty}_K(x, y)])$ are

$$\left(\frac{(1 - t_u)s_u t_u \sqrt{s_u^2 + c_\lambda}}{\sqrt{1 + \alpha^2}}, \frac{-\alpha(1 - t_u)s_u + \alpha t_u \sqrt{s_u^2 + c_\lambda}}{\sqrt{1 + \alpha^2}}, \lambda s_u^2 + 2\lambda t_u c_\lambda - m \right),$$

where $0 \le t_u \le 1$ and $s_u \ge 0$. However, the (x, y) coordinates in these two cases do not represent the same points. Therefore, we need to set them equal so that

$$t_l = \frac{\sqrt{s_u^2 + c_\lambda}\left(\sqrt{s_l^2 + c_\lambda} - s_u\right)}{\sqrt{s_u^2 + c_\lambda}\sqrt{s_l^2 + c_\lambda} - s_u s_l}, \quad t_u = \frac{s_l\left(\sqrt{s_l^2 + c_\lambda} - s_u\right)}{\sqrt{s_u^2 + c_\lambda}\sqrt{s_l^2 + c_\lambda} - s_u s_l}. \tag{6.1}$$

As $0 \le t_l, t_u \le 1$, we see that $|s_u^2 - s_l^2| \le c_\lambda$. Thus if we let

$$x(s_l, s_u) = \frac{(1 - t_l)\sqrt{s_l^2 + c_\lambda} + t_l s_l}{\sqrt{1 + \alpha^2}}, \quad y(s_l, s_u) = \frac{-\alpha(1 - t_l)\sqrt{s_l^2 + c_\lambda} + \alpha t_l s_l}{\sqrt{1 + \alpha^2}},$$

and

$$A^{\infty}_{\lambda}(f_K)(s_l, s_u) = \frac{1}{2}\Big(\lambda(s_l^2 - s_u^2) + 2\lambda c_\lambda((1 - t_l - t_u))\Big),$$

the graph of the average approximation of f_K in the sector S_+ defined above is

$$\Gamma_{S_+,\lambda} = \left\{(x(s_l, s_u),\, y(s_l, s_u),\, A^{\infty}_{\lambda}(f_K)(s_l, s_u)),\ s_u \ge 0,\ s_l \ge 0,\ |s_u^2 - s_l^2| \le c_\lambda\right\},$$

where t_l and t_u are given by (6.1).

Although it is not easy to write the graph in the standard Euclidean system, observe that the graph is smooth in the interior region $\{(s_l, s_u),\, s_l > 0,\, s_u > 0, |s_l^2 - s_u^2| < c_\lambda\}$.

By our construction, we also note that the surface $\Gamma_{S_+,\lambda}$ is formed by the average of two families of parameterized line segments. Also, when $\lambda > 0$ is large, outside a small sector, say, $S_+^\lambda = \{|y| \le \alpha, 0 < x < 2\sqrt{2m/\lambda}\}$, our formula is an interpolation in $S_+ \setminus S_+^\lambda$. Figure 9(b) shows a portion of the graph of $A_\lambda^\infty(f_K)$.

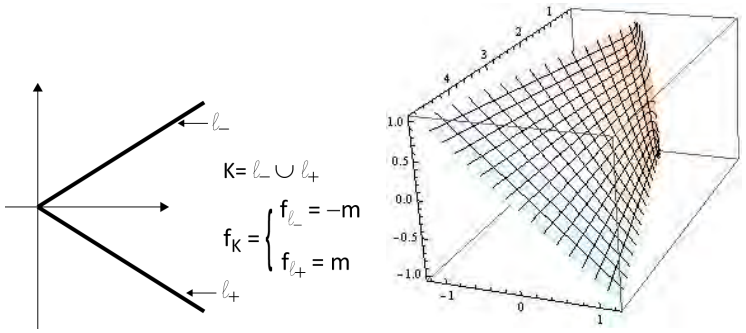

(a) (b)

Figure 9. *Example 6.6.* (a) *Sampled set K with the definition of f_K that presents a discontinuity jump at $(0,0)$.* (b) *Graph of $A_\lambda^\infty(f_K)$ with $\alpha = 0.25$, $m = 1$, and $\lambda = 5$.*

7. Numerical examples. For more complicated sets K and functions f_K, the average approximation operators $A_\lambda^M(f_K)$ and $A_\lambda^\infty(f_K)$ must be evaluated numerically. Figure 10 sketches the steps needed for their implementation. It is noted that the numerical realization relies mainly on the availability of numerical schemes for computing the upper and lower transforms of a given function, which in turn means the availability of schemes to compute the convex envelope of a function. Because of the locality property of the compensated convex transforms (see, for instance, Theorem 3.10 in [57], where quantitative estimates of the neighborhood size are also given), it is possible to develop fast schemes that depend only on the local behavior of the input function. This is in sharp contrast to the evaluation of the convex envelope of a function which is a global evaluation. In the current context, we consider a generalization of the scheme introduced in [37] which is briefly summarized in Algorithm 1 and described below. Given a uniform grid of points $x_k \in \mathbb{R}^n$, equally spaced with grid size h, let us denote by S_{x_k} the d-point stencil of $\mathbb{R}^n$ with center at x_K defined as $S_{x_k} = \{x_k + hr, |r|_\infty \le 1, r \in \mathbb{Z}^n\}$ with $|\cdot|_\infty$ the ℓ^∞-norm of $r \in \mathbb{Z}^n$ and $d = \#(S)$. At each grid point x_k we compute the convex envelope of f at x_k by an iterative scheme where each iteration step m is given by

$$(\mathsf{co}\, f)_m(x_k) = \min\left\{f(x_k), \sum \lambda_i (\mathsf{co}\, f)_{m-1}(x_i), \sum \lambda_i = 1, \lambda_i \ge 0, x_i \in S_{x_k}\right\}$$

with the minimum taken between $f(x_k)$ and only some convex combinations at the stencil grid points. For the full algorithmic and implementation details of the scheme, the convex combinations that one needs to take, and its convergence analysis, we refer the reader to [53].

In this section, we present some illustrative numerical experiments of the applications described above, namely, for surface reconstruction from contour lines, point clouds, and image inpainting. For the first two applications, we discuss examples of approximation of

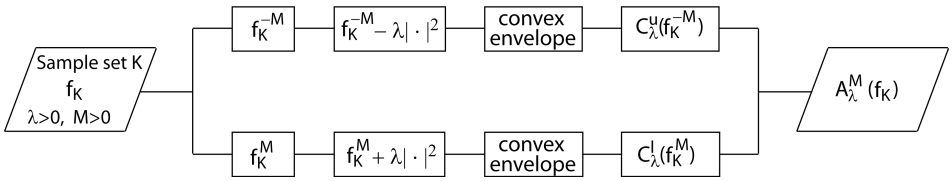

Figure 10. *Flow chart for the numerical evaluation of* $A_\lambda^M(f_K)$.

Algorithm 1. Conceptual implementation of the scheme that computes the convex envelope of f.

Set $m = 1$, $(\mathsf{co}\, f)_0 = f$, tol
$\epsilon = \|f\|_{L^2}$
while $\epsilon > tol$ **do**
  $\forall x_k, \quad (\mathsf{co}\, f)_m(x_k) = \min\left\{ f(x_k), \sum \lambda_i (\mathsf{co}\, f)_{m-1}(x_i), \ \sum \lambda_i = 1, \ \lambda_i \geq 0, \ x_i \in S_{x_k} \right\}$
  $\epsilon = \|(\mathsf{co}\, f)_m - (\mathsf{co}\, f)_{m-1}\|_{L^2}$
  $m \leftarrow m + 1$
end while

a smooth function, of a continuous but nondifferentiable function, and of a discontinuous function. The quality of the approximation is measured by computing the relative L^2-error

$$\epsilon = \frac{\|f - A_\lambda^M(f_K)\|_{L^2(\Omega)}}{\|f\|_{L^2(\Omega)}}, \tag{7.1}$$

where f is the original function that we want to approximate and $A_\lambda^M(f_K)$ is the average approximation of the sample f_K of f over K. We mainly postpone a thorough comparison with other state-of-art methods to forthcoming papers, just giving some first comparisons with the AMLE method presented in [2, 13] and applied to surface reconstruction and image inpainting. Image denoising for salt & pepper noise and image inpainting were solved by the TV model described in [14] and in [29], respectively.

We conclude this short introduction by stating that at least for the examples and methods we have considered here, we have observed higher accuracy of the $A_\lambda^M(f_K)$ interpolant and faster execution time for its numerical evaluation compared to the other methods.

7.1. Surface reconstruction from contour lines. We describe next some numerical experiments on surface reconstruction from sectional contours. This is the problem of reconstructing the graph of a function f by knowing only some contour lines of f, and it has applications in medical imaging, computer graphics, reverse engineering, and terrain modeling, among other areas. The underlying function $f : \mathbb{R}^2 \supset \Omega \to \mathbb{R}$ is assumed to have various regularity properties. Consider first the reconstruction of an infinitely differentiable function given by the Franke test function [25] and then the reconstruction of functions with less regularity. In addition to the relative L^2-error ϵ defined by (7.1), which gives a measure of how close

$A_\lambda^M(f_K)$ is to f, we also compute

$$\epsilon_K = \frac{\|f_K - A_\lambda^M(f_K)_K\|_{L^2(K)}}{\|f_K\|_{L^2(K)}}, \tag{7.2}$$

where f_K is the sample function and $A_\lambda^M(f_K)_K$ the restriction of $A_\lambda^M(f_K)$ to K, to assess the quality of $A_\lambda^M(f_K)$ as an interpolant of f_K. We will thus verify that in the examples where f is continuous, the average approximation $A_\lambda^M(f_K)$ represents an interpolation of f_K, consistently with the theoretical results established in section 3.

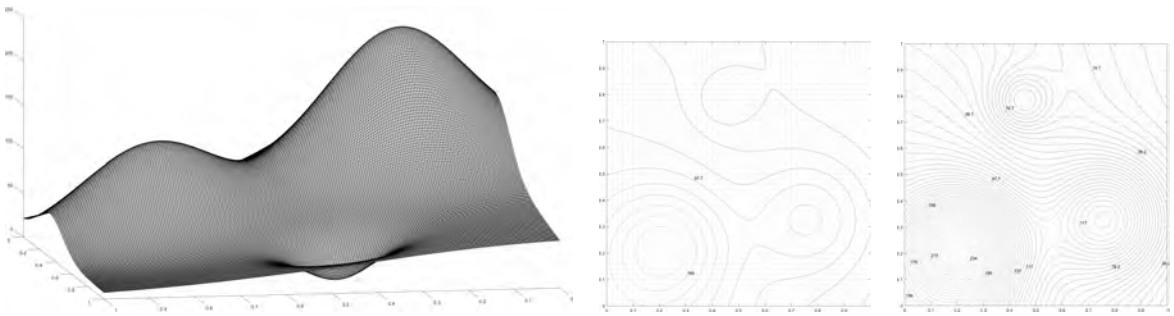

(a) (b) (c)

Figure 11. *Example* 7.1.1. (a) *Graph of the Franke test function* f *defined by* (7.3). (b) *Sample set* K *of* 10*-contour lines of* f *at equally spaced heights equal to* $(\max(f) - \min(f))/10$*, defining the sample function* f_K. (c) *Sample set* K *of* 50*-contour lines of* f *at equally spaced heights equal to* $(\max(f) - \min(f))/50$*, defining the sample function* f_K.

7.1.1. Franke test function. The Franke function was introduced in [25] as one of the test functions for the evaluation of methods for scattered data interpolation [26]. The function consists of two Gaussian peaks and a sharper Gaussian dip superimposed on a surface sloping toward the first quadrant [25] and is defined by

$$\begin{aligned} f(x,y) = {} & \frac{3}{4}e^{-\left((9x-2)^2+(9y-2)^2\right)/4} + \frac{3}{4}e^{-\left((9x+1)^2/49+(9y+1)^2/10\right)} + \frac{1}{2}e^{-\left((9x-7)^2/4-(9y-3)^2\right)/4} \\ & - \frac{1}{5}e^{-\left((9x-4)^2+(9y-7)^2\right)}. \end{aligned} \tag{7.3}$$

Consider f defined in the unit square $\Omega =]0, 1[^2$. Its graph is displayed in Figure 11(a). Approximations using two different sets of contour lines have been computed by applying the methods described in this paper and by the AMLE model introduced in [13] and applied in [2] to the interpolation of digital elevation models. The two sets of contour lines consist of 10 and 50 equally spaced level lines, respectively. Given the smoothness of f, the isolines are also smooth curves. The two sample sets are displayed in Figures 11(b) and 11(c), respectively, whereas the graphs of the corresponding average approximations $A_\lambda^M(f_K)$ are shown in Figures 12(a) and 12(c). Figures 12(b) and 12(d) display, on the other hand, the corresponding contour lines which, compared to the same equally spaced level lines of f displayed in Figure 11(c),

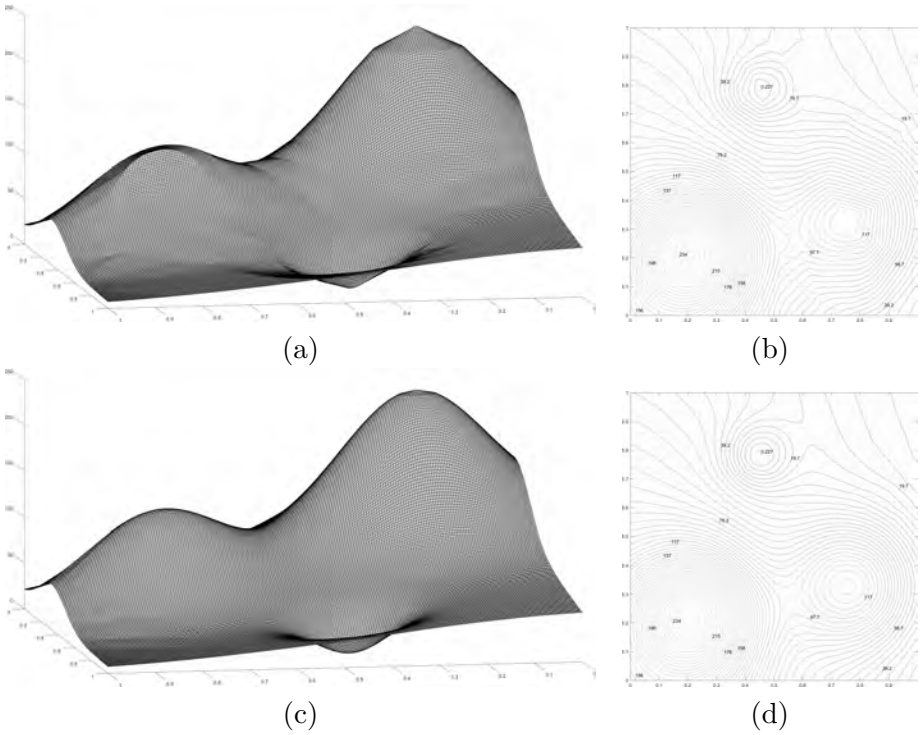

Figure 12. *Example* 7.1.1. (a) *Graph of the interpolation function* $A_\lambda^M(f_K)$ *computed for* $\lambda = 1 \cdot 10^4$, $M = 1 \cdot 10^5$, *and corresponding to the set* K *of* 10*-contour lines of* f *displayed in Figure* 11(b). *Relative* L^2*-errors:* $\epsilon = 0.01986$, $\epsilon_K = 3.33 \cdot 10^{-15}$. (b) *Isolines of* $A_\lambda^M(f_K)$ *at equally spaced heights equal to* $(\max(f) - \min(f))/50$. (c) *Graph of the interpolation function* $A_\lambda^M(f_K)$ *computed for* $\lambda = 1 \cdot 10^4$, $M = \cdot 10^5$, *and corresponding to the set* K *of* 50*-contour lines of* f *displayed in Figure* 11(d). *Relative* L^2*-errors:* $\epsilon = 0.0021$, $\epsilon_K = 2.62 \cdot 10^{-15}$. (d) *Isolines of* $A_\lambda^M(f_K)$ *at equally spaced heights equal to* $(\max(f) - \min(f))/50$.

show a good quality of the reconstruction given by $A_\lambda^M(f_K)$. This is also confirmed by the values of the relative L^2-error ϵ equal to 0.01986 and 0.00218 for the two sample sets K of contour lines, respectively. Note the clear reduction of error by increasing the density of the data set. For the two average approximations, the value of ϵ_K is of the order of 10^{-15}, confirming that the average approximation $A_\lambda^M(f_K)$ interpolates exactly f_K.

Figure 13 displays the reconstruction obtained by the AMLE method. The numerical results were obtained by using the MATLAB code described in [39]. In this case, for a number of iterations equal to 10^6, we found a relative L^2-error higher than the one generated by $A_\lambda^M(f_K)$ with ϵ equal to 0.0338 and 0.0101 for the two sample sets K of 10 and 50 level lines, respectively. Consistently with the findings of [35], also here we find that the AMLE interpolation generates additional kinks which are not present in f and might be the cause for the reduced quality of the approximation compared to $A_\lambda^M(f_K)$.

7.1.2. Continuous piecewise affine function. We describe now the approximation of the continuous piecewise affine function f associated with the triangulation shown in Figure 14(a), where also the node values of f are given, while Figure 14(b) displays the graph of f. Two different sample sets of contour lines have been considered. One consists of six

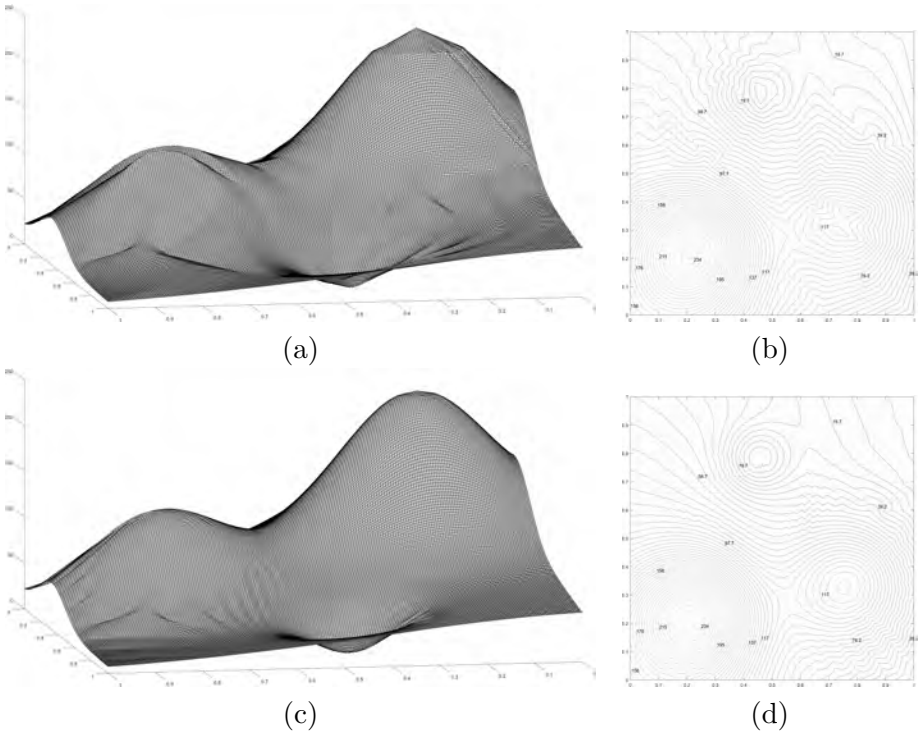

Figure 13. *Example* 7.1.1. (a) *Graph of the AMLE interpolation function of* f_K *with* K *the set of* 10*-contour lines of* f *displayed in Figure* 11(b). *Relative* L^2*-error* $\epsilon = 0.0338$. (b) *Isolines of the AMLE interpolation function of* f_K *at equally spaced heights equal to* $(\max(f) - \min(f))/50$. (c) *Graph of the AMLE interpolation function of* f_K *with* K *the set of* 50*-contour lines of* f *displayed in Figure* 11(d). *Relative* L^2*-error* $\epsilon = 0.0101$. (d) *Isolines of the AMLE interpolation function of* f_K *at equally spaced heights equal to* $(\max(f) - \min(f))/50$.

isolines, whereas the other is formed by 15 isolines. The isolines are not equally spaced and are displayed in Figures 14(c) and 14(d), respectively, whereas the graphs of the corresponding average approximations $A_\lambda^M(f_K)$ are shown in Figures 15(a) and 15(c) along with the isolines corresponding to 50 equally spaced isolevels. In this example the isolines are not smooth curves, so locally, around their singularities, for the interpretation of the results, it can be useful to recall and compare them with the behavior of the average approximation described in the prototype Example 6.5(ii) in section 6. The average approximation displays a step which reduces by increasing the number of isolines. Note that these steps are also visible in the MATLAB display of the graph of the function f; thus they are errors of the interpolation scheme that is used. We find that for the reconstruction of the function sampled on the six-contour line set, the relative L^2-error ϵ is equal to 0.019302. This value reduces to 0.004805 for the reconstruction of the function sampled on the 15-contour line set K. For both of these examples, it is confirmed that the average approximation $A_\lambda^M(f_K)$ interpolates f_K given that the computed value of ϵ_K is of the order of 10^{-16}.

The AMLE method appears to yield slightly better results for the reconstruction from the sample set K of six contour lines. In this case, we find a relative L^2-error ϵ equal to 0.01675, slightly lower than the one produced by $A_\lambda^M(f_K)$. Figure 16(a) displays the graph of the AMLE

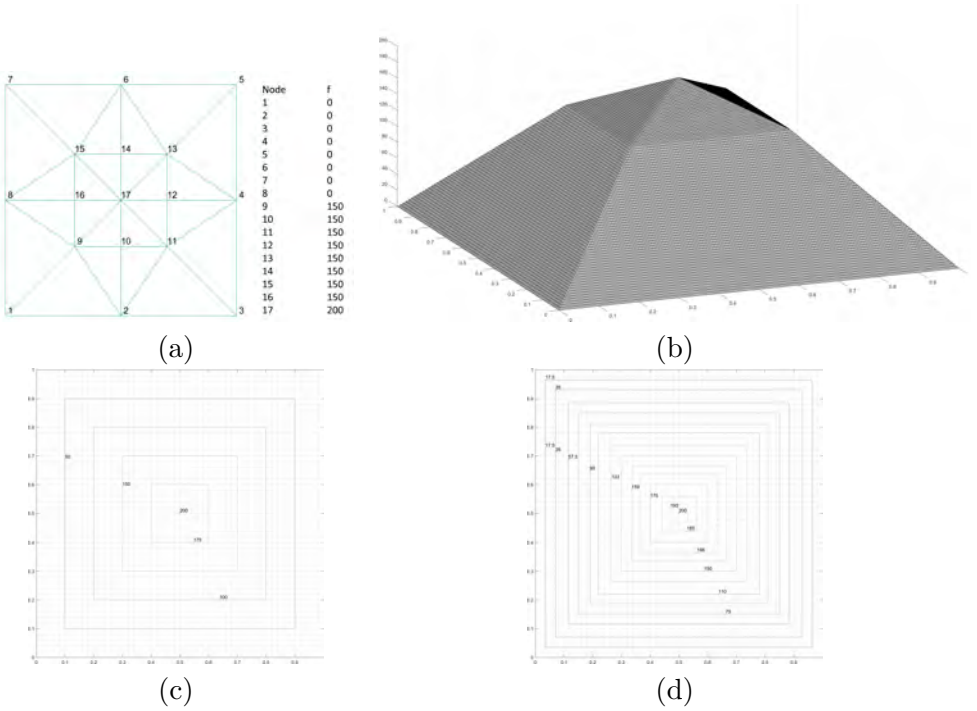

Figure 14. *Example* 7.1.2. (a) *Triangulation with nodal values used to construct a continuous piecewise affine function.* (b) *Graph of* f *associated with the triangulation defined in* (a). (c) *Sample set* K *of* 6*-contour line of* f*, defining the sample function* f_K. (d) *Sample set* K *of* 15*-contour line of* f*, defining the sample function* f_K.

interpolant which does not contain steps along the edges of the pyramid, whereas Figure 16(b) shows its isolines for 50 levels of equally spaced heights. For the AMLE interpolant of the sample set K of 15 contour lines, whose graph is displayed in Figure 16(c) and the isolines in Figure 16(d), the relative L^2-error ϵ is equal to 0.00713, which is slightly higher than the one produced by $A_\lambda^M(f_K)$ for the same sample set K. Here note also the appearance of additional kinks in the graph of the AMLE interpolant, which might reduce the global quality of the AMLE approximation compared to $A_\lambda^M(f_K)$.

7.1.3. Discontinuous piecewise affine function. The approximation of discontinuous functions has not been covered by the theoretical developments of section 3, where we assumed f to be continuous. Now we present a test case where we examine how our average approximation performs numerically and verify that also in this case $A_\lambda^M(f_K)$ represents a continuous interpolation of f_K. We consider the following discontinuous piecewise affine func-

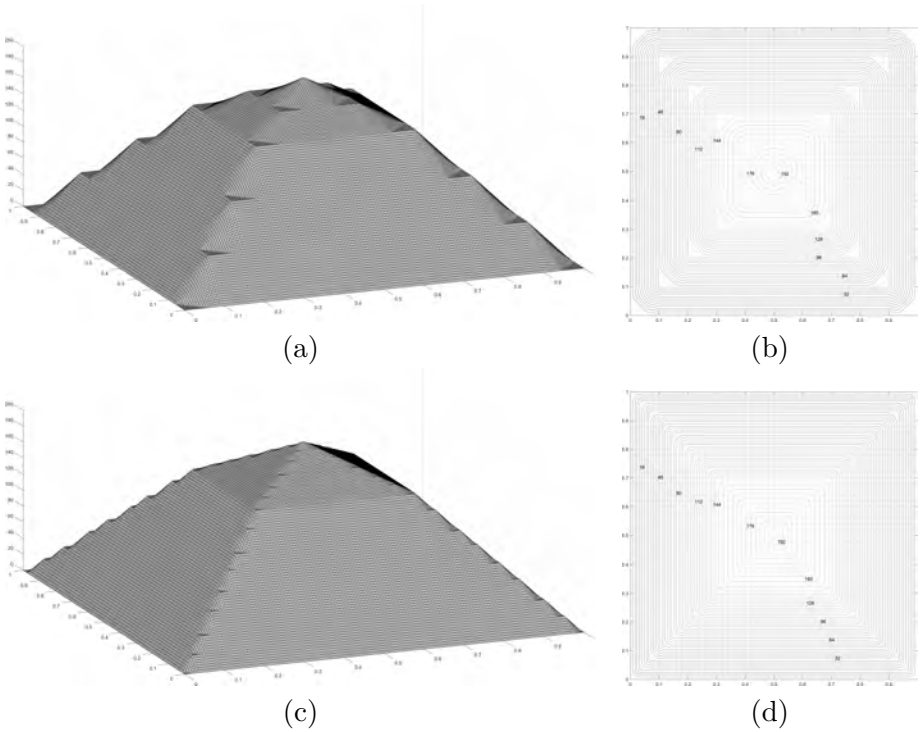

Figure 15. *Example 7.1.2.* (a) *Graph of the interpolation function* $A_\lambda^M(f_K)$ *with* K *given in Figure 14(c), and* $\lambda = 1 \cdot 10^5$, $M = 1 \cdot 10^5$, *tol* $= 10^{-9}$. *Relative* L^2*-errors:* $\epsilon = 0.019302$, $\epsilon_K = 4.50 \cdot 10^{-16}$. (b) *Isolines of* $A_\lambda^M(f_K)$ *at equally spaced heights equal to* $(\max(f) - \min(f))/50$. (c) *Graph of the interpolation function* $A_\lambda^M(f_K)$ *with* K *given in Figure 14(d), and* $\lambda = 1 \cdot 10^5$, $M = 1 \cdot 10^5$, *tol* $= 10^{-9}$. *Relative* L^2*-errors:* $\epsilon = 0.004805$, $\epsilon_K = 8.68 \cdot 10^{-16}$. (d) *Isolines of* $A_\lambda^M(f_K)$ *at equally spaced heights equal to* $(\max(f) - \min(f))/50$.

tion:

$$f : (x, y) \in]0,\, 1[^2 \to 200, \quad f(x,y) = \begin{cases} x + y - 1 & \text{if } 1/2 \le x \le 1, \quad 1/2 \le y \le 1, \\ x - y - 1/2 & \text{if } 1/2 \le x \le 1, \quad 0 \le y < 1/2, \\ -x + y - 1/2 & \text{if } 0 \le x < 1/2, \quad 1/2 \le y \le 1, \\ -x - y & \text{if } 0 \le x < 1/2, \quad 0 \le y < 1/2, \end{cases}$$

whose graph is displayed in Figure 17(b), while Figure 17(a) shows the equation of f in each of its affine parts.

We compare the reconstruction of f for two sample sets K, one formed by 20 equally spaced isolines and the other by 100 equally spaced isolines. Such sets are displayed in Figures 17(c) and 17(d), respectively. Notably, for both sample sets K, $A_\lambda^M(f_K)$ coincides exactly with the original function f. We find, indeed, for both sample sets K, ϵ and ϵ_K are of the order of 10^{-15} by taking $\lambda = 10^7$, $M = 10^6$. This occurs because of an exact sampling of the discontinuity jump; thus we are able to reproduce exactly the affine parts of f, consistently with the theoretical findings of section 3. Furthermore, given the high value of λ and recalling

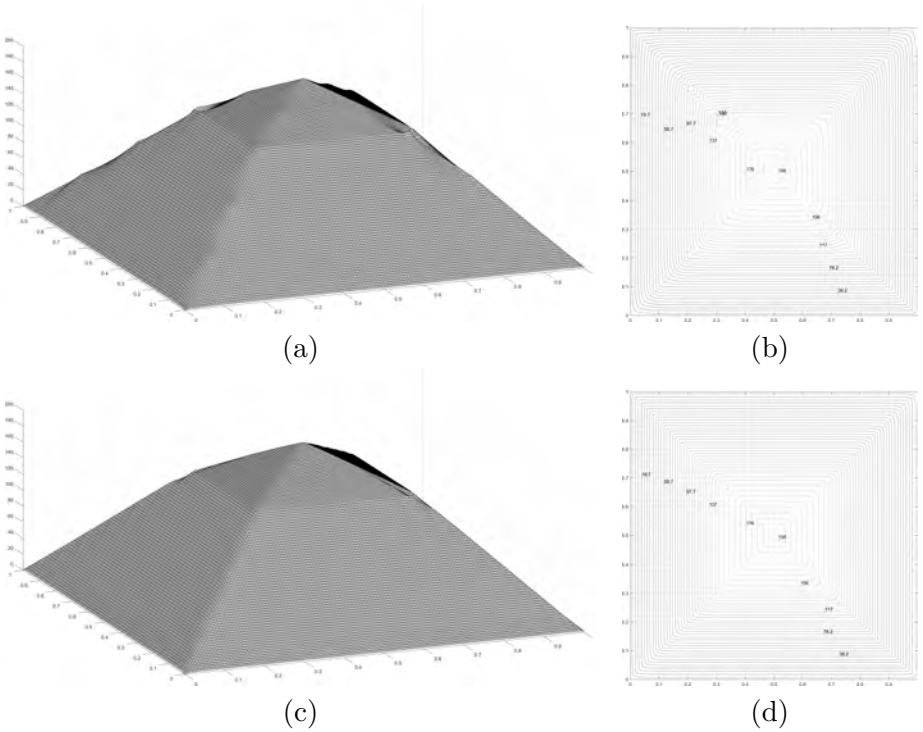

Figure 16. *Example* 7.1.2. (a) *Graph of the AMLE interpolation function of* f_K *with* K *the set of* 6*-contour lines of* f *displayed in Figure* 14(c). *Relative* L^2*-error* $\epsilon = 0.01675$. (b) *Isolines of the AMLE interpolant at equally spaced heights equal to* $(\max(f) - \min(f))/50$. (c) *Graph of the AMLE interpolation function of* f_K *with* K *the set of* 15*-contour lines of* f *displayed in Figure* 14(d). *Relative* L^2*-error* $\epsilon = 0.0071297$. (d) *Isolines of the AMLE interpolant at equally spaced heights equal to* $(\max(f) - \min(f))/50$.

the behavior of the jump in the prototype Example 5.3, we are able to describe the sharp discontinuity.

For the case where we do not have an exact sampling of the discontinuity jump, we refer the reader to Example 7.2.3 concerning the surface reconstruction from point clouds with sampling points not necessarily on the discontinuity.

A different behavior is displayed by the AMLE interpolation. Consistently with the observations in [35], the level lines of the AMLE interpolant are smooth [44]; thus discontinuities cannot be recovered. A better visual appreciation of this fact is obtained by looking at the graphs of the AMLE interpolant shown in Figures 18(a) and 18(c) for the two sample sets K, and at their isolines displayed in Figures 18(b) and 18(d), respectively. The isolines at the two sides of the jump should "end" in the discontinuity, but they are somehow enforced to join each other by the continuous isolines of the AMLE interpolant. In this case we find values of the relative L^2-error ϵ, with $\epsilon = 0.1071$ and $\epsilon = 0.06738$ for the two sample sets, respectively.

Table 1 summarizes the relative L^2-errors of $A^M_\lambda(f_K)$ and the AMLE interpolant for the examples considered in this section.

7.2. Scattered data approximation. We turn now to some numerical experiments on scattered data approximation. In particular, in the terminology of [36], we consider the

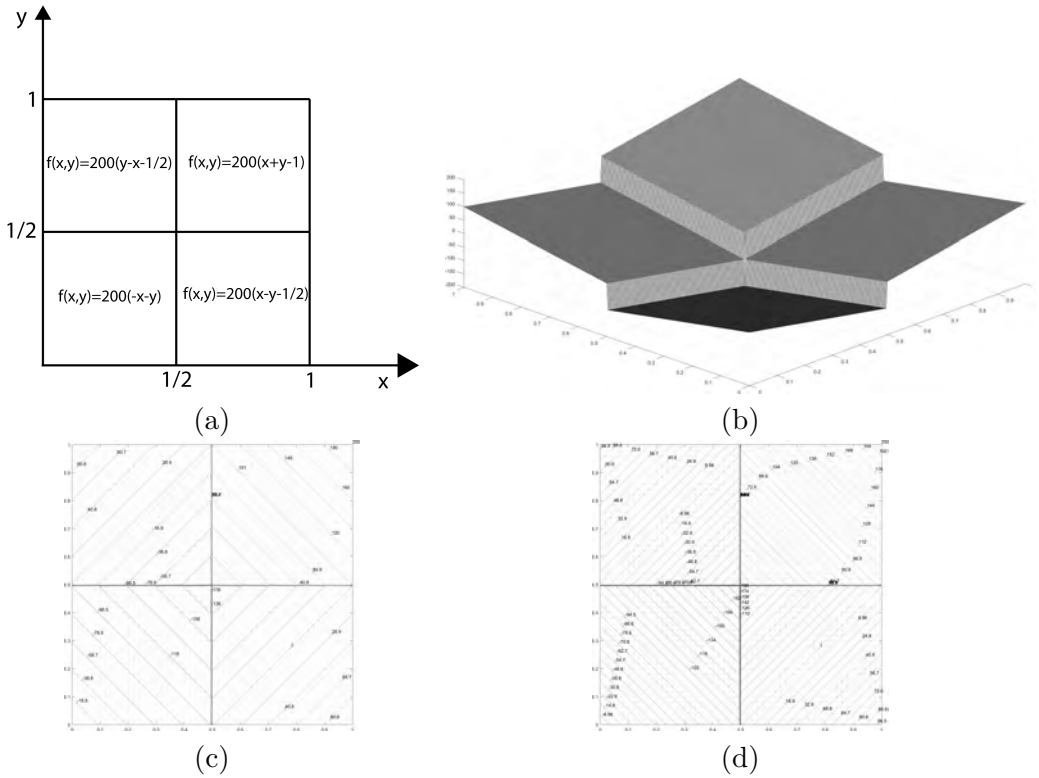

Figure 17. *Example* 7.1.3. (a) *Equations of each affine part of* f. (b) *Graph of* f. (c) *Sample set* K *of* 20*-contour line of* f *at equally spaced heights equal to* $(\max(f) - \min(f))/20$*, defining the sample function* f_K. (d) *Sample set* K *of* 50*-contour lines of* f *at equally spaced heights equal to* $(\max(f) - \min(f))/50$*, defining the sample function* f_K.

problem of function reconstruction from point clouds, where the sample points that form the set K do not meet any particular condition as to spacing or density. As in the previous section, the set of test problems consists of three test functions with different regularity: an infinitely differentiable function given by the Franke test function, a continuous piecewise affine function, and a discontinuous piecewise affine function. The three test functions are all to be approximated in $\Omega =]0, 1[^2$. In the numerical implementation of the method, the domain Ω is discretized with a grid of 201×201 points, and the two sample sets K are obtained by sampling the grid points using a random number generator with different levels of density. The two sample sets K, corresponding to a coarse and a dense sampling, are displayed in Figures 19(a) and 19(b), respectively. The reason for taking such a regular discretization of Ω is that the numerical scheme we use to compute the convex envelope (see Algorithm 1) is particularly suitable for applications to image processing where such discrete geometry is related to the image resolution.

For the measure of the global quality of the approximation $A_\lambda^M(f_K)$ we compute the

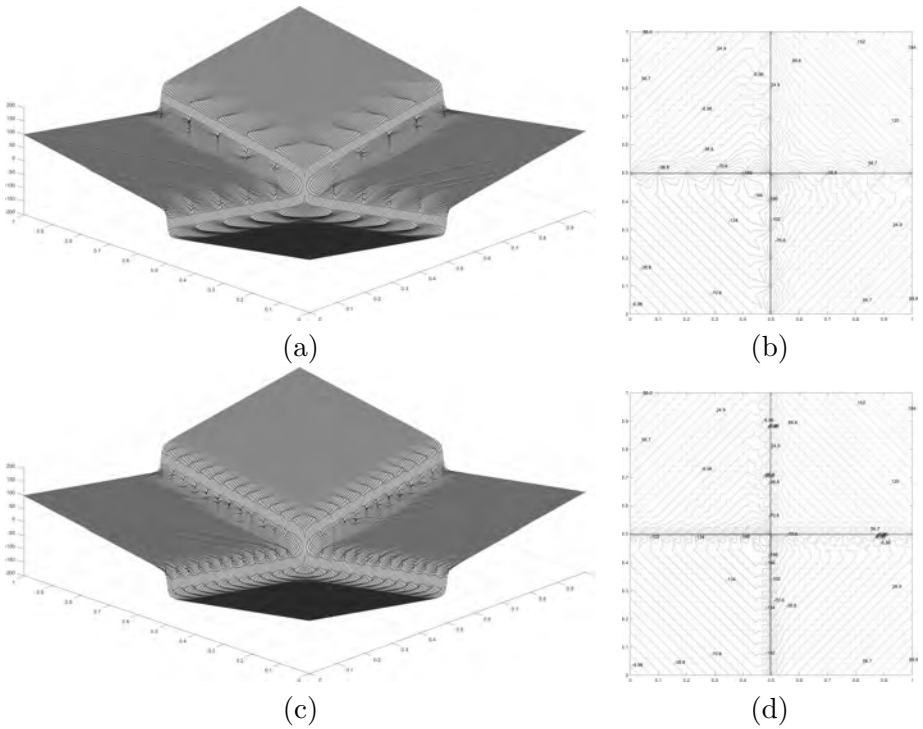

Figure 18. *Example* 7.1.3. (a) *Graph of the AMLE interpolation function of* f_K *with* K *the set of* 20*-contour lines of* f *displayed in Figure* 17(c). *Relative* L^2*-error* $\epsilon = 0.1071$. (b) *Isolines of the AMLE interpolant at equally spaced heights equal to* $(\max(f) - \min(f))/50$. (c) *Graph of the AMLE interpolation function of* f_K *with* K *the set of* 50*-contour lines of* f *displayed in Figure* 17(d). *Relative* L^2*-error* $\epsilon = 0.06738$. (d) *Isolines of the AMLE interpolant at equally spaced heights equal to* $(\max(f) - \min(f))/50$.

Table 1

Summary of the accuracy of the compensated convexity based interpolant $A_\lambda^M(f_K)$ *and of the AMLE interpolant for the examples considered in section* 7.1. *Legend:* K*, sample set.* ϵ*, relative* L^2*-error.* ϵ_K*, relative* L^2*-error on the sample set* K*.* F*, Franke test function (Example* 7.1.1*).* CPA*, continuous piecewise affine function (Example* 7.1.2*).* DPA*, discontinuous piecewise affine function (Example* 7.1.3*).*

		ϵ	
f	K	$A_\lambda^M(f_K)$	AMLE
F	10 level lines	0.0199	0.0338
	50 level lines	0.0021	0.0101
CPA	6 level lines	0.0193	0.0167
	15 level lines	0.0048	0.0071
DPA	20 level lines	$8.7 \cdot 10^{-15}$	0.1071
	100 level lines	$1.5 \cdot 10^{-16}$	0.0674

relative L^2-error ϵ defined by (7.1), whereas we will use the relative L^2-error ϵ_K defined by

$$\epsilon_K = \frac{\sqrt{\sum_{k\in K} |f(x_k) - A_\lambda^M(f_K)(x_k)|^2}}{\sqrt{\sum_{k\in K} |f(x_k)|^2}} \tag{7.4}$$

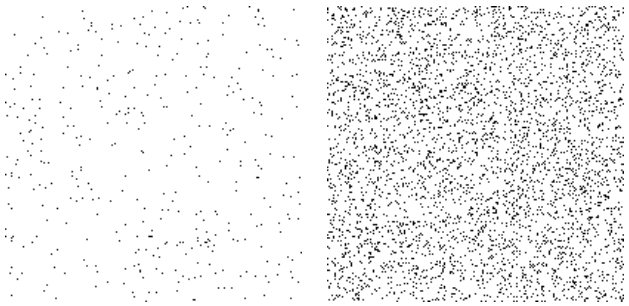

(a) (b)

Figure 19. *Set K of sample points of a grid of 201×201 points in $]0, 1[^2$ for two levels of sampling density:* (a) *Coarse sampling with* 400 *grid points out of* 40401. (b) *Dense sampling with* 4061 *grid points out of* 40401.

to assess the quality of $A_\lambda^M(f_K)$ as interpolant of f_K. In this case, too, we will find that the average approximation $A_\lambda^M(f_K)$ is an interpolation of f_K, consistently with the theoretical findings of section 4. We then conclude this section by giving an example of digital elevation model reconstruction starting from real data, and another of salt & pepper noise removal as an application of scattered data approximation to image processing.

7.2.1. Franke test function. In this example, the Franke test function f defined by (7.3) is sampled over the two sets K of scattered points displayed in Figures 19(a) and 19(b), respectively. For the resulting sample functions f_K we compute the corresponding average approximations $A_\lambda^M(f_K)$, whose graphs are displayed in Figure 20, along with the respective isolines. Specifically, the comparison of the isolines of $A_\lambda^M(f_K)$ displayed in Figures 20(b) and 20(d) for the coarse and dense sample sets K, respectively, with the isolines of the Franke function f displayed in Figure 11(d), allows a visual appreciation of the quality of the reconstruction. This is also confirmed by the computed values of the relative L^2-error ϵ. For the coarse sample set we get $\epsilon = 0.0206$, whereas, for the denser sample set, $\epsilon = 0.00157$. Finally, also in this case, we verify that $A_\lambda^M(f_K)$ is an interpolant of f_K given that for both approximations the relative L^2-error ϵ_K defined by (7.4) is of the order of 10^{-15}.

The AMLE method as introduced in [13] can be applied also in this case for the interpolation of isolated points. In fact, this is one of its particular features out of the PDE-based interpolators. The graphs of the AMLE interpolants for the two sample sets are displayed in Figure 21, which contains also the plot of the corresponding isolines for 50 level lines of equally spaced heights. The plot of these isolines, once compared with the same isolines of f displayed in Figure 11(c), allows a visual assessment of the quality of the reconstruction. As in Example 7.1.1 concerning the reconstruction from contour lines, we note also here the introduction of artificial artifacts in the form of kinks in the graph of the interpolant, which, in contrast, are not present in the graph of $A_\lambda^M(f_K)$. For the coarse and dense sampling set we find that the relative L^2-error of the AMLE interpolant amounts to $\epsilon = 0.05764$ and $\epsilon = 0.010902$, respectively, which are slightly higher than the values produced by $A_\lambda^M(f_K)$.

7.2.2. Continuous piecewise affine function. The continuous piecewise affine function f introduced in section 7.1.2 is evaluated here over the two sample sets K of Figures 19(a)

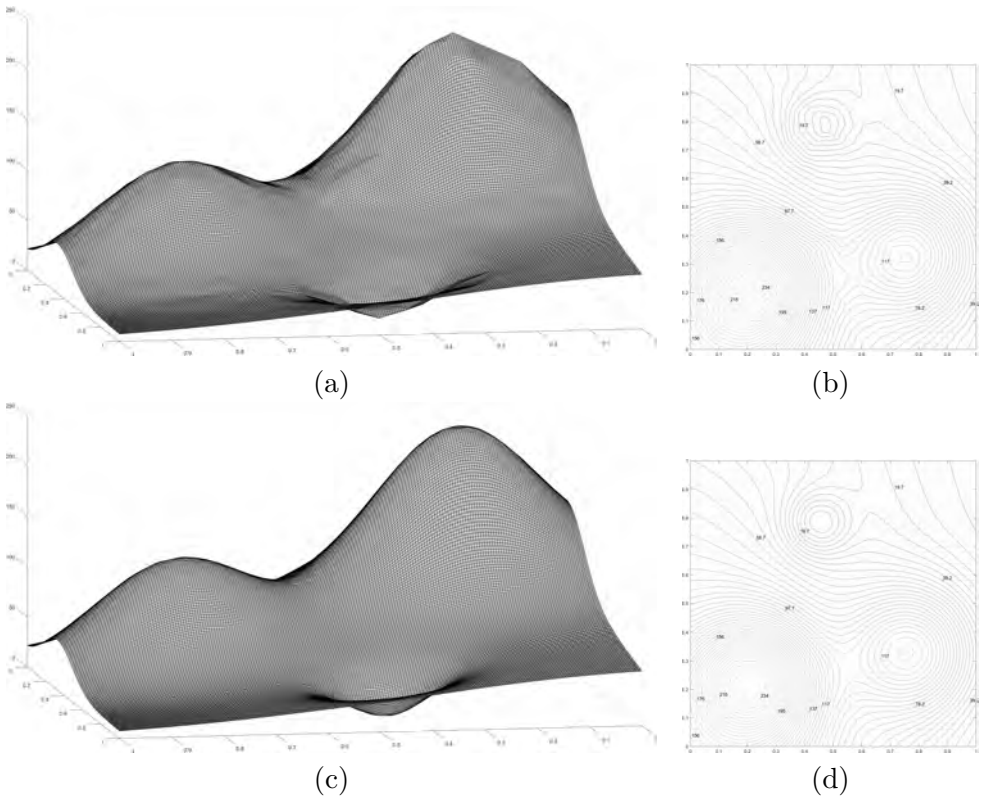

Figure 20. *Example* 7.2.1. (a) *Graph of* $A_\lambda^M(f_K)$ *for* $\lambda = 1 \cdot 10^4$, $M = 1 \cdot 10^5$, *and the set* K *of Figure* 19(a). *Relative* L^2*-errors:* $\epsilon = 0.020252$, $\epsilon_K = 5.31 \cdot 10^{-15}$. (b) *Isolines of* $A_\lambda^M(f_K)$ *at equally spaced heights equal to* $(\max(f) - \min(f))/50$. (c) *Graph of* $A_\lambda^M(f_K)$ *for* $\lambda = 5 \cdot 10^3$, $M = 1 \cdot 10^5$, *and the set* K *of Figure* 19(b). *Relative* L^2*-errors:* $\epsilon = 0.0015548$, $\epsilon_K = 4.13 \cdot 10^{-15}$. (d) *Isolines of* $A_\lambda^M(f_K)$ *at equally spaced heights equal to* $(\max(f) - \min(f))/50$.

and 19(b), defining two test cases of sample function f_K. The graph of the corresponding average approximation $A_\lambda^M(f_K)$ is displayed in Figure 22 along with the respective isolines, whereas Figure 23 shows those of the AMLE interpolating along with its isolines of equally spaced heights. The drawing of the isolines allows a visual assessment of the quality of the reconstruction if these are compared to the isolines of the original function f displayed in Figure 15(c). A first observation about the graphs of $A_\lambda^M(f_K)$ is the near absence of the steps along the edges of the pyramid due to the constraint enforced by the fixed contour lines; on the contrary, the graphs of the AMLE interpolant present, even for this example, artifacts in the form of artificial kinks and valleys. The relative L^2-error ϵ produced by $A_\lambda^M(f_K)$ is equal to 0.0215 for the coarse sample set and to 0.00390 for the denser sample set, whereas it is $\epsilon = 0.053594$ and $\epsilon = 0.012515$ for the AMLE interpolant of the coarse and dense sample set, respectively. Compared with the reconstruction of f from contour lines, where the sample points can be considered to be somehow organized, we observe that both the reconstructed function $A_\lambda^M(f_K)$ and the AMLE interpolant appear to be less regular, which reflects the fact that the sample points are scattered over Ω without any requirement of spacing or density.

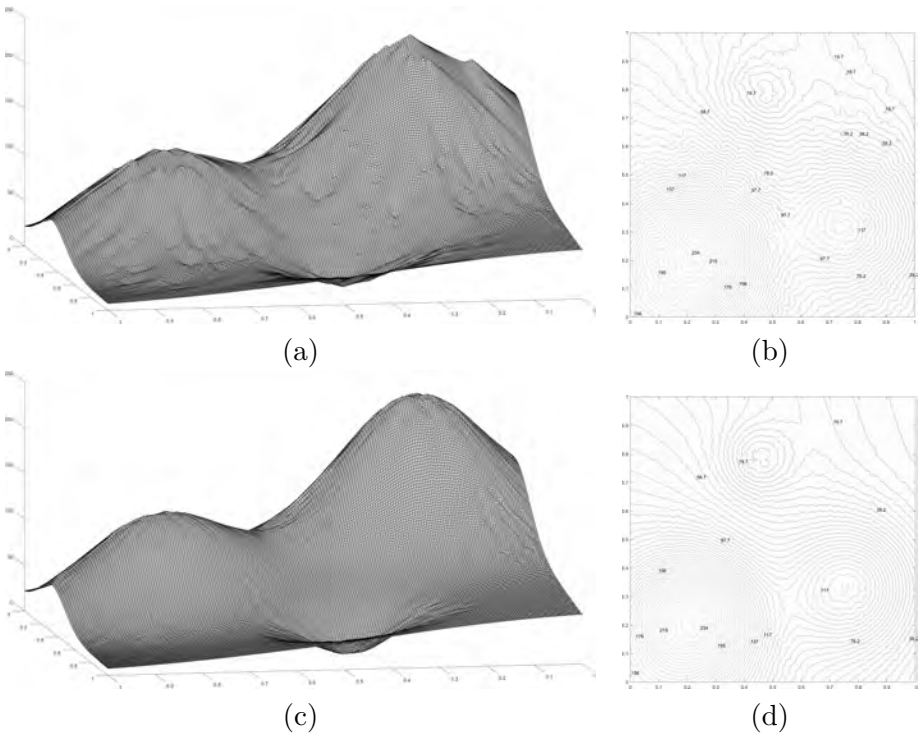

Figure 21. *Example* 7.2.1. (a) *Graph of the AMLE interpolation function of* f_K *with* K *the set of scattered points displayed in Figure* 19(a). *Relative* L^2*-error:* $\epsilon = 0.05764$. (b) *Isolines of the AMLE interpolant at equally spaced heights equal to* $(\max(f) - \min(f))/50$. (c) *Graph of the AMLE interpolation function of* f_K *with* K *the set of scattered points displayed in Figure* 19(b). *Relative* L^2*-error:* $\epsilon = 0.010902$. (d) *Isolines of the AMLE interpolant at equally spaced heights equal to* $(\max(f) - \min(f))/50$.

This effect clearly reduces by increasing the density of the sample points, though for the AMLE interpolant we note that the relative L^2-errors for the two cases of sampling density remain of the same order of magnitude. For this example, too, we finally verify that $A_\lambda^M(f_K)$ is an interpolation of f_K given that the relative L^2-error ϵ_K is of the order 10^{-16} for both test cases.

7.2.3. Discontinuous piecewise affine function. The discontinuous piecewise affine function f introduced in section 7.1.3 is evaluated here over the two sample sets K displayed in Figures 19(a) and 19(b) to form two sample functions f_K corresponding to a coarse and a dense sample set, respectively. The graph of $A_\lambda^M(f_K)$ is displayed in Figure 24 for the two cases, along with their isolines, whereas Figure 25 shows the graph of the AMLE interpolants along with their isolines with equally spaced heights. Also here, it is useful to compare such isolines with those of the original function f displayed in Figure 18(d) for a visual assessment of the quality of the reconstructions. Unlike the reconstruction of f from contour lines, where we had the exact sampling of the discontinuity which was coincident with the grid lines, here we note an irregular behavior for $A_\lambda^M(f_K)$ around the discontinuities of f. Such irregular behavior reduces by increasing the sampling density, especially if such density increase occurs in the neighborhood of the singularities. On the other hand, the AMLE interpolant displays

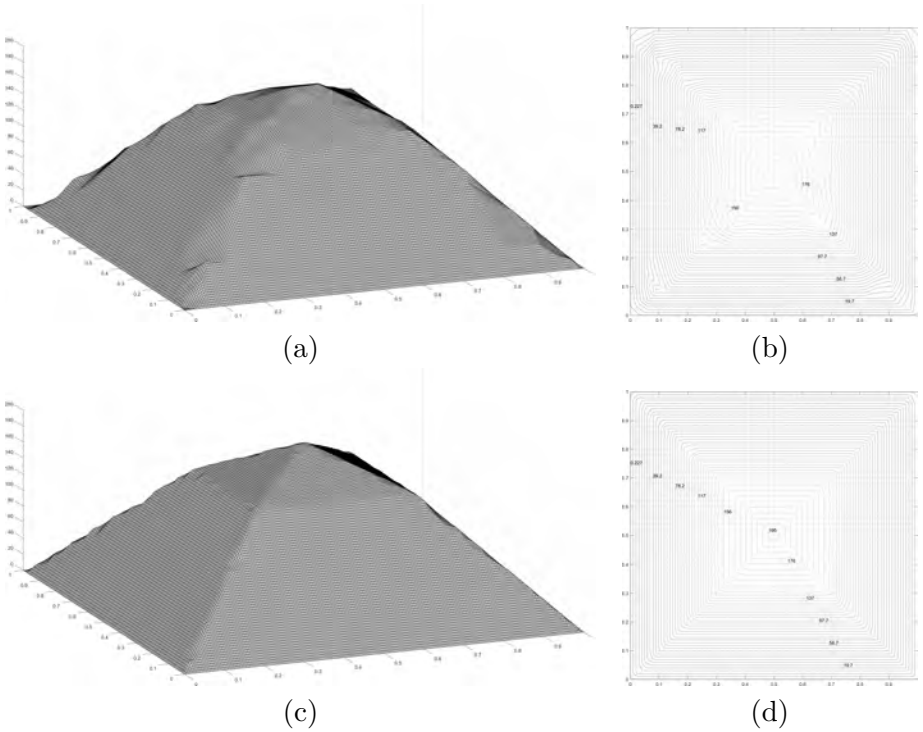

Figure 22. *Example* 7.2.2. (a) *Graph of* $A^M_\lambda(f_K)$ *for* $\lambda = 5 \cdot 10^4$, $M = 1 \cdot 10^5$, *and the set* K *of Figure* 19(a). *Relative* L^2*-errors:* $\epsilon = 0.021574$, $\epsilon_K = 4.4626 \cdot 10^{-16}$. (b) *Isolines of* $A^M_\lambda(f_K)$ *at equally spaced heights equal to* $(\max(f) - \min(f))/50$. (c) *Graph of* $A^M_\lambda(f_K)$ *for* $\lambda = 5 \cdot 10^4$, $M = 1 \cdot 10^5$, *and the set* K *of Figure* 19(b). *Relative* L^2*-errors:* $\epsilon = 0.003914$, $\epsilon_K = 6.2983 \cdot 10^{-16}$. (d) *Isolines of* $A^M_\lambda(f_K)$ *at equally spaced heights equal to* $(\max(f) - \min(f))/50$.

around the singularities a behavior similar to the one obtained from the contour lines, with the difference that now the transition from one affine part of f to the other appears to be smoother. As for the accuracy of the reconstructions, for $A^M_\lambda(f_K)$ we find that $\epsilon = 0.173$ for the coarse sample set and $\epsilon = 0.0901$ for the denser sample set, whereas the relative L^2-error ϵ_K on both sample sets K is of the order of 10^{-16}, confirming that again, $A^M_\lambda(f_K)$ is an interpolant of f_K. For the AMLE interpolant, even in this case, we find higher values for the relative L^2-error, with $\epsilon = 0.22577$ and $\epsilon = 0.13897$ for the coarser and denser sample set, respectively. We note also the introduction of artificial artifacts in the graph of the AMLE interpolant.

The relative L^2-errors obtained for scattered data approximation using A^M_λ and AMLE interpolation are summarized in Table 2 for the examples considered in this section.

7.2.4. DEM reconstruction. We consider here the problem of producing a Digital Elevation Map (DEM) from a sample of the the NASA SRTM global digital elevation model of Earth land. The data provided by the National Elevation Dataset [27] contain geographical coordinates (latitude, longitude, and elevation) of points sampled at one arc-second intervals in latitude and longitude. For our experiments, we choose the region defined by the coordinates [N 40°48′50″, N 40°52′50″] × [E 14°45′50″, E 14°50′00″] extracted from the SRTM1 cell

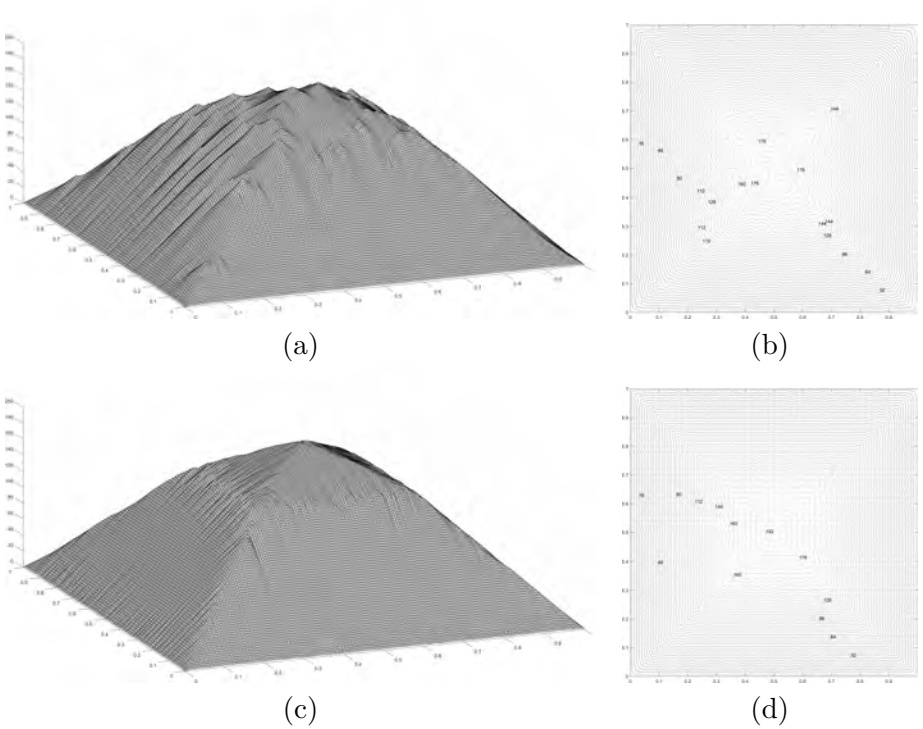

Figure 23. *Example* 7.2.2. (a) *Graph of the AMLE interpolation function of* f_K *with* K *the set of scattered points displayed in Figure* 19(a). *Relative* L^2*-error:* $\epsilon = 0.053594$. (b) *Isolines of the AMLE interpolant at equally spaced heights equal to* $(\max(f) - \min(f))/50$. (c) *Graph of the AMLE interpolation function of* f_K *with* K *the set of scattered points displayed in Figure* 19(b). *Relative* L^2*-error:* $\epsilon = 0.012515$. (d) *Isolines of the AMLE interpolant at equally spaced heights equal to* $(\max(f) - \min(f))/50$.

$N40E014.hgt$ [1]. Such a region consists of an area with extension 7.413 Km × 5.844 km and height varying between 266 m and 1600 m, with variegated topography features. In the digitization by the U.S. Geological Survey, each pixel represents a 30 m × 30 m patch. Figure 26(a) displays the elevation model from the SRTM1 data, which we refer to in the following as the ground truth model. We will take a sample f_K of such data, make the reconstruction using the $A^M_\lambda(f_K)$ and the AMLE interpolant, and compare them with the ground truth model. In the numerical experiments, we consider two sample data, characterized by different data density and type of information. The first, which we refer to as sample set K_1, consists only of level lines at a regular height interval of 66 m and contains 19% of the ground truth real digital data. The second sample set, denoted by K_2, has been formed by randomly taking the 30% of the points belonging to the level lines of the set K_1 and scattered points corresponding to 5% density so that the sample set K_2 amounts to about 9% of the ground truth points. The two sample sets K_1 and K_2 are shown in Figures 26(b) and 26(c), respectively. The graph of the $A^M_\lambda(f_K)$ interpolant and of the AMLE interpolant for the two sample sets along with the respective isolines at equally spaced heights equal to 66 m are displayed in Figures 27 and 28, respectively, whereas Table 3 contains the values of the relative L^2-error between such interpolants and the ground truth model. Though both reconstructions are comparable visually to

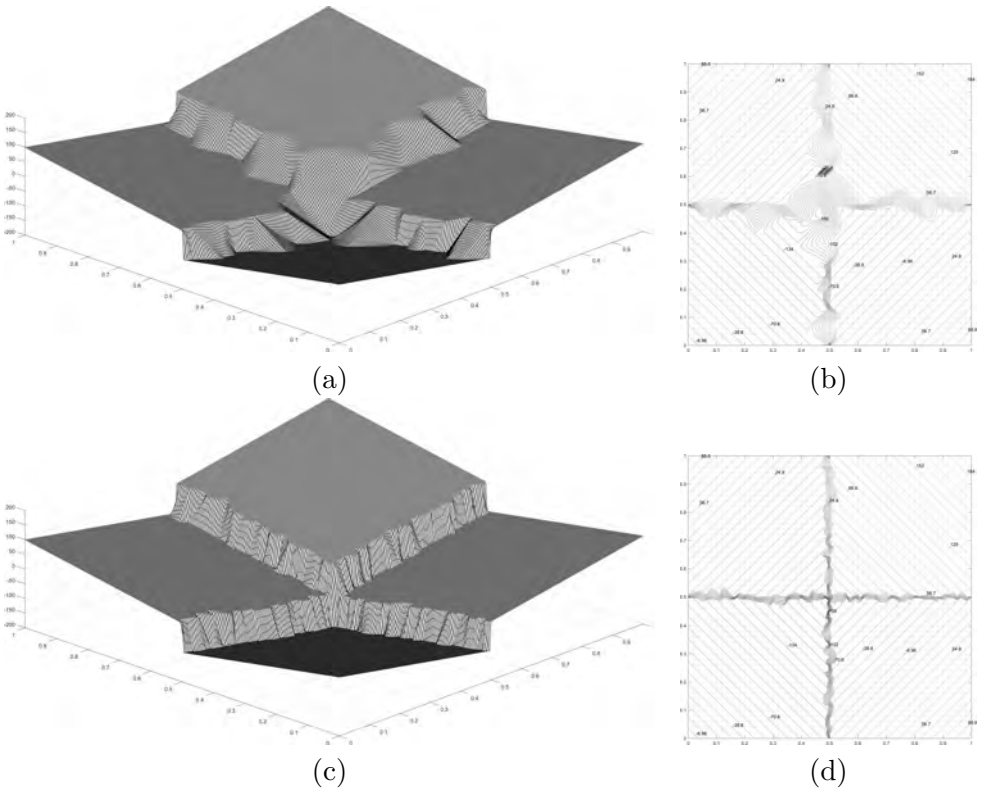

Figure 24. *Example* 7.2.3. (a) *Graph of* $A^M_\lambda(f_K)$ *for* $\lambda = 1 \cdot 10^7$, $M = 1 \cdot 10^5$, *and the set* K *of Figure* 19(a). *Relative* L^2*-errors:* $\epsilon = 0.16729$, $\epsilon_K = 1.2849 \cdot 10^{-16}$. (b) *Isolines of* $A^M_\lambda(f_K)$ *at equally spaced heights equal to* $(\max(f) - \min(f))/50$. (c) *Graph of* $A^M_\lambda(f_K)$ *for* $\lambda = 1 \cdot 10^7$, $M = 1 \cdot 10^5$, *and the set* K *of Figure* 19(b). *Relative* L^2*-errors:* $\epsilon = 0.088589$, $\epsilon_K = 1.459 \cdot 10^{-16}$. (d) *Isolines of* $A^M_\lambda(f_K)$ *at equally spaced heights equal to* $(\max(f) - \min(f))/50$.

the ground truth model, a closer inspection of the pictures shows that in the reconstruction from the synthetic data, the AMLE interpolant does not correctly reconstruct the mountains' peaks, which appear to be smoothed, and introduces artificial ridges along the slopes of the mountains. In contrast, the $A^M_\lambda(f_K)$ interpolant appears better for capturing features of the ground truth model. Finally, we also note that though the sample set K_1 contains a number of ground truth points higher than the sample set K_2, the reconstruction from K_2 appears to be better than the one obtained from K_1. This behavior was found for both interpolations, though it is more notable in the case of the $A^M_\lambda(f_K)$ interpolant. By taking scattered data, we are able to get a better characterization of irregular surfaces compared to the one obtained from a structured representation such as provided by the level lines.

7.2.5. Salt & pepper noise removal. As an application of scattered data approximation to image processing, we consider here the restoration of an image corrupted by salt & pepper noise. This is an impulse-type noise that is caused, for instance, by malfunctioning pixels in camera sensors or faulty memory locations in hardware, so that information is lost at the faulty pixels and the corrupted pixels are set alternatively to the minimum or to the

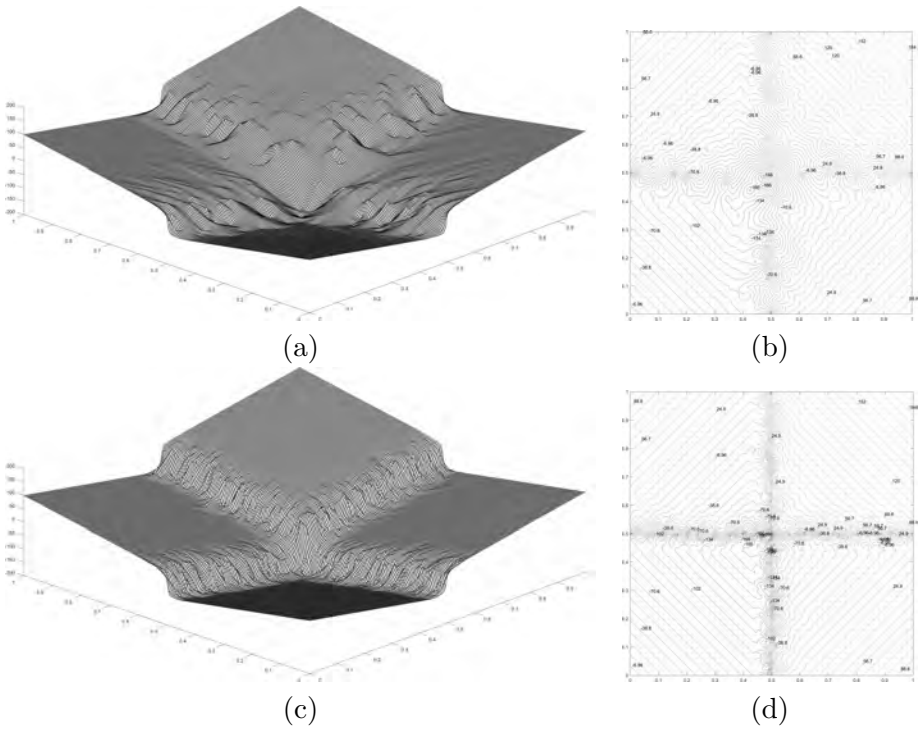

Figure 25. *Example 7.2.3.* (a) *Graph of the AMLE interpolation function of f_K with K the set of scattered points displayed in Figure 19*(a). *Relative L^2-error: $\epsilon = 0.22577$.* (b) *Isolines of the AMLE interpolant at equally spaced heights equal to* $(\max(f) - \min(f))/50$. (c) *Graph of the AMLE interpolation function of f_K with K the set of scattered points displayed in Figure 19*(b). *Relative L^2-error: $\epsilon = 0.13897$.* (d) *Isolines of the AMLE interpolant at equally spaced heights equal to* $(\max(f) - \min(f))/50$.

Table 2

Accuracy of the interpolation for the examples considered in section 7.2. Legend: K, sample set. ϵ, relative L^2-error. ϵ_K, relative L^2-error on the sample set K. F, Franke test function (Example 7.1.1). CPA, continuous piecewise affine function (Example 7.1.2). DPA, discontinuous piecewise affine function (Example 7.1.3).

		ϵ	
f	K	$A^M_\lambda(f_K)$	AMLE
F	coarse	0.0203	0.0576
	dense	0.0016	0.0109
CPA	coarse	0.0216	0.0536
	dense	0.0039	0.0125
DPA	coarse	0.1673	0.2258
	dense	0.0876	0.1390

maximum value of the range of the image values. When the noise density is low, about less than 40%, the median filter is quite effective for restoring the image. However, this filter loses its denoising power for higher noise density given that details and features of the original image are smeared out. In those cases, other techniques must be applied; one possibility is the two-stage TV-based method proposed in [14]. In the following numerical experiments, we consider the image displayed in Figure 29(a) with size 512×512 pixels, damaged by 70% salt

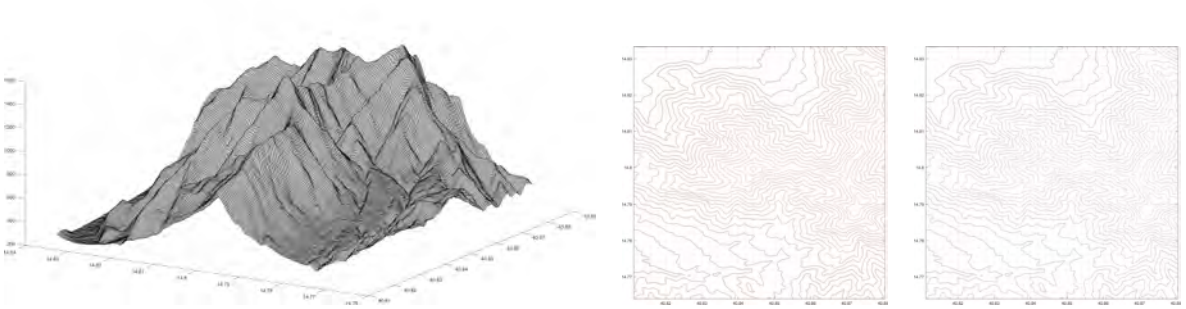

Figure 26. *Example* 7.2.4. *Reconstruction of real-world digital elevation maps.* (a) *Ground truth model from USGS-STRM*1 *data relative to the area with geographical coordinates;* $[\mathrm{N}\,40^\circ 48'50'', \mathrm{N}\,40^\circ 52'50''] \times [\mathrm{E}\,14^\circ 45'50'', \mathrm{E}\,14^\circ 50'00'']$. (b) *Sample set* K_1 *formed by only level lines at regular height interval of* 66 m. *The set* K_1 *contains* 19% *of the ground truth points.* (c) *Sample set* K_2 *formed by taking randomly* 30% *of the points belonging to the level lines of the set* K_1 *and scattered points corresponding to* 5% *density. The sample set* K_2 *contains* 9% *of the ground truth points.*

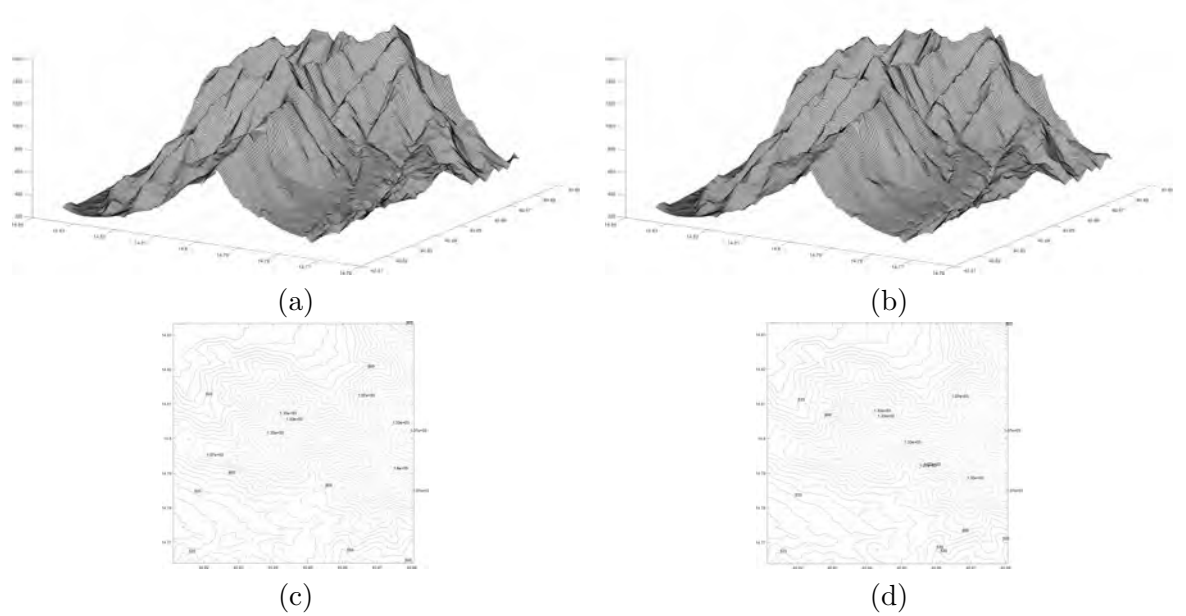

Figure 27. *Example* 7.2.4. *Reconstruction of real-world digital elevation maps.* (a) *Graph of* $A^M_\lambda(f_K)$ *for sample set* K_1. *Parameters:* $\lambda = 1 \cdot 10^3$, $M = 1 \cdot 10^6$. *Relative* L^2*-errors:* $\epsilon = 0.01560$, $\epsilon_K = 0$. (b) *Graph of* $A^M_\lambda(f_K)$ *for sample set* K_2. *Parameters:* $\lambda = 1 \cdot 10^3$, $M = 1 \cdot 10^6$. *Relative* L^2*-errors:* $\epsilon = 0.0117$, $\epsilon_K = 0$. (c) *Isolines of* $A^M_\lambda(f_K)$ *from sample set* K_1 *at regular heights of* 66 m. (d) *Isolines of* $A^M_\lambda(f_K)$ *from sample set* K_2 *at regular heights of* 66 m.

& pepper noise. The resulting corrupted image is displayed in Figure 29(b), where only 78643 pixels out of the total 262144 pixels carry true information. The true image values represent our sample function f_K, whereas the set of the true pixels forms our sample set K. To assess the restoration performance we use the peak signal-to-noise ratio (PSNR) which is expressed

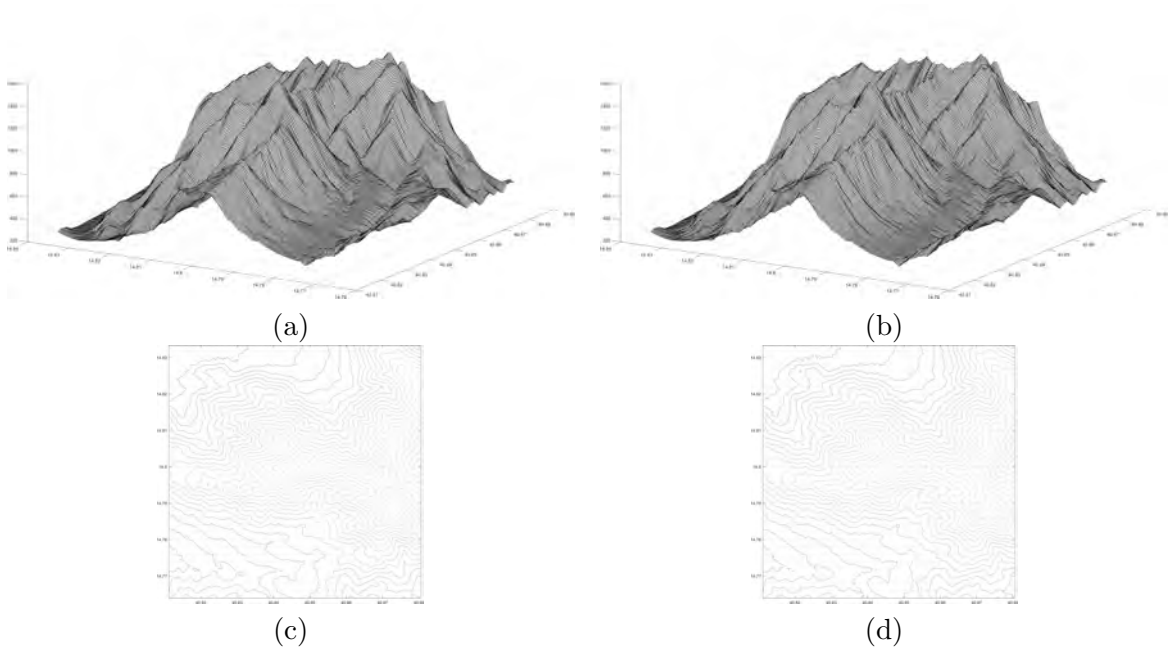

Figure 28. *Example 7.2.4. Reconstruction of real-world digital elevation maps.* (a) *Graph of the AMLE Interpolant from set* K_1. *Relative* L^2*-error:* $\epsilon = 0.0214$. (b) *Graph of the AMLE Interpolant from set* K_2. *Relative* L^2*-error:* $\epsilon = 0.0226$. (c) *Isolines of the AMLE Interpolant from sample set* K_1 *at regular heights of* 66 m. (d) *Isolines of the AMLE Interpolant from sample set* K_2 *at regular heights of* 66 m.

Table 3

Relative L^2*-error for the DEM reconstruction from the two sample sets using the* $A^M_\lambda(f_K)$ *and the AMLE interpolant.*

	ϵ	
Sample set	$A^M_\lambda(f_K)$	AMLE
K_1	0.0156	0.02137
K_2	0.0117	0.02261

in the units of dB and, for an 8-bit image, is defined by

$$\text{PSNR} = 10 \log_{10} \frac{255^2}{\frac{1}{mn} \sum_{i,j} |f_{i,j} - r_{i,j}|^2}, \tag{7.5}$$

where $f_{i,j}$ and $r_{i,j}$ denote the pixel values of the original and restored image, respectively, and m, n denote the size of the image f. In our numerical experiments, we have considered the following cases. The first one assumes the set K to be given by the noise-free interior pixels of the corrupted image together with the boundary pixels of the original image. In the second case, K is just the set of the noise-free pixels of the corrupted image, without any special consideration of the image boundary pixels. In analyzing this second case, to reduce the boundary effects produced by the application of Algorithm 1, we have applied our method to an enlarged image and then restricted the resulting restored image to the original domain. The enlarged image has been obtained by padding a fixed number of pixels before the first image

element and after the last image element along each dimension, making mirror reflections with respect to the boundary. The values used for padding are all from the corrupted image. In our examples, we have considered two versions of enlarged images, obtained by padding the corrupted image with 2 pixels and 10 pixels, respectively. Table 4 compares the values of the PSNR of the restored images by our method and the TV-based method applied to the corrupted image with noise-free boundary and to the two versions of the enlarged images with the boundary values of the enlarged images given by the padded noisy image data. We observe that there are no important variations in the denoising result between the different methods of treating the image boundary. This is also reflected by the close value of the PSNR of the resulting restored images. For 70% salt & pepper noise, Figure 29(c) displays the restored image $A_\lambda^M(f_K)$ with K equal to the true set that has been enlarged by two pixels, whereas Figure 29(d) shows the restored image by the TV-based method [12, 14] using the same set K. Although the visual quality of the images restored from 70% noise corruption is comparable between our method and the TV-based method, the PSNR using our method is higher than that for the TV-based method in all of the experiments reported in Table 4. An additional advantage of our method is its speed. Our method does not require initialization, which is in contrast to the two-stage TV-based method, for which the initialization, for instance, is given by the restored image using an adaptive median filter.

Finally, to demonstrate the performance of our method in some extreme cases of very sparse data, we consider cases of noise density equal to 90% and 99%. Figure 30 displays the restored image by the compensated-convexity–based method and by the TV-based method for cases where K is padded by two pixels and ten pixels for 90% and 99% noise level, respectively. As far as the visual quality of the restored images is concerned, and to the extent that such judgement can make sense given the high level of noise density, the inspection of Figure 30 seems to indicate that $A_\lambda^M(f_K)$ gives a better approximation of details than the TV-based restored image. This is also reflected by the values of the PSNR index in Table 4.

Table 4

Comparison of PSNR *of the restored images by the compensated convexity based method ($A_\lambda^M(f_K)$) and by the two-stage TV-based method (TV) for different sets K.*

	PSNR					
	K with noise-free boundary		K padded by two pixels		K padded by ten pixels	
Noise density	$A_\lambda^M(f_K)$	TV	$A_\lambda^M(f_K)$	TV	$A_\lambda^M(f_K)$	TV
70% (6.990 dB)	31.910 dB	31.175 dB	31.865 dB	31.134 dB	31.869 dB	31.136 dB
90% (5.901 dB)	27.574 dB	26.625 dB	27.506 dB	26.564 dB	27.513 dB	26.566 dB
99% (5.492 dB)	22.076 dB	20.595 dB	21.761 dB	20.469 dB	21.972 dB	20.492 dB

7.3. Image inpainting. As an example of image inpainting, we consider the problem of removing text overprinted on the image displayed in Figure 31(a). If we denote by P the set of pixels containing the overprinted text, and by Ω the domain of the whole image, then $K = \Omega \setminus P$ is the set of the true pixels, and the inpainting problem is in fact the problem of reconstructing the image over P from knowing f_K, if we denote by f the original image values. To assess the performance of our reconstruction compared to state-of-art inpainting methods, we compare our method with the TV-based image inpainting method solved by the split Bregman method described in [29] and with the AMLE inpainting reported in [45].

Figure 29. *Example* 7.2.5. (a) *Original image with size* 512×512. (b) *Original image covered by a salt & pepper noise density of* 70%. PSNR = 6.99 dB. (c) *Restored image* $A_\lambda^M(f_K)$ *with* K *the set of the pixels not corrupted by the salt & pepper noise when the corrupted image is enlarged symmetrically by two pixels on each side,* $\lambda = 15$ *and* $M = 1E13$. PSNR = 31.865 dB. *If the boundary pixels were noise-free, the corresponding restored image would have* PSNR = 31.910 dB. (d) *Restored image by the two-stage TV-based method described in* [12, 14] *with* K *the set of the pixels not corrupted by the salt & pepper noise when the corrupted image is enlarged symmetrically by two pixels on each side.* PSNR = 31.134 dB. *If the boundary pixels were noise-free, the corresponding restored image would have* PSNR = 31.175 dB.

The restored image $A_\lambda^M(f_K)$ obtained by our compensated convexity method is displayed in Figure 31(b), and the restored image by the AMLE method is shown in Figure 31(d), whereas Figure 31(c) presents the restored image by the the split Bregman inpainting method. All the restored images look visually quite good. However, if we use the PSNR as a measure of the quality of the restoration, we find that $A_\lambda^M(f_K)$ has a value of PSNR equal to 42.2066 dB, and the split Bregman inpainting restored image gives a value for PSNR = 41.0498 dB, whereas the AMLE restored image has PSNR equal to 39.4405 dB.

Finally, to assess how well $A_\lambda^M(f_K)$ is able to preserve image details and not introduce unintended effects such as image blurring and staircase effects, Figure 32 displays details of the original image and of the restored images by the three methods. Once again, the good performance of $A_\lambda^M(f_K)$ can be appreciated visually.

Figure 30. *Example* 7.2.5. *Restoration of* 90% *corrupted image (*PSNR $= 5.901\,\mathrm{dB}$*) by* (a) *restored image* $A_\lambda^M(f_K)$*, with* K *the set of the pixels not corrupted by the salt & pepper noise when the corrupted image is enlarged symmetrically by two pixels on each side,* $\lambda = 15$ *and* $M = 1E13$. PSNR $= 27.506\,\mathrm{dB}$. (b) *Restored image by the two-stage TV-based method described in* [12, 14] *with the same set* K *as in* (a). PSNR $= 26.564\,\mathrm{dB}$. *Restoration of* 99% *corrupted image (*PSNR $= 5.492\,\mathrm{dB}$*) by* (c) *restored image* $A_\lambda^M(f_K)$*, with* K *the set of the pixels not corrupted by the salt & pepper noise when the corrupted image is enlarged symmetrically by ten pixels on each side,* $\lambda = 15$ *and* $M = 1E13$. PSNR $= 21.972\,\mathrm{dB}$. (d) *Restored image by the two-stage TV-based method described in* [12, 14] *with the same set* K *as in* (c). PSNR $= 20.492\,\mathrm{dB}$.

8. Proofs of the main results.

Proof of Proposition 2.8. We write $(x, y) \in \mathbb{R}^{n+m}$ with $x \in \mathbb{R}^n$ and $y \in \mathbb{R}^m$. We only prove the result for the upper transform as the proof of the lower transform is similar. By the definition of the upper transform, we have

$$\mathsf{co}[\lambda|\cdot|^2 - f](x) = \lambda|x|^2 - C_\lambda^u(f(x)), \quad x \in \mathbb{R}^n\,.$$

We show that $\mathsf{co}[\lambda|\cdot|^2 - f](x)$ is also the convex envelope of the function $\lambda(|x|^2+|y|^2) - g^{-M}(x, y)$ restricted to $z = 0$. By definition,

$$\lambda|x|^2 - C_\lambda^u(f(x)) = \mathsf{co}[\lambda|\cdot|^2 - f](x) \le \lambda|x|^2 - f(x) \le \lambda(|x|^2 + |y|^2) - g^{-M}(x, y)$$

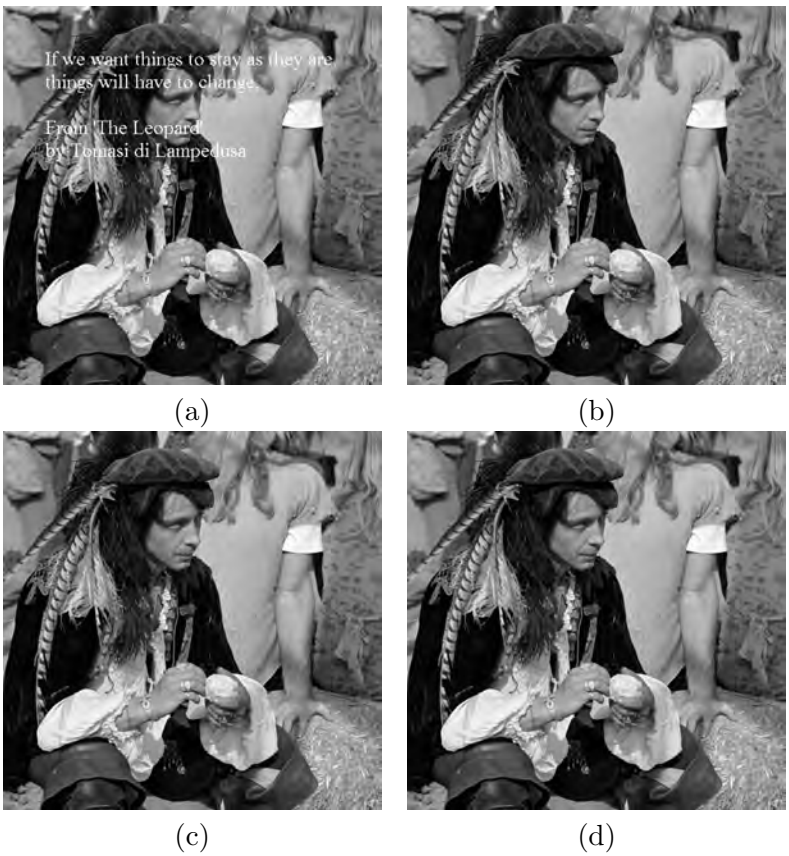

Figure 31. *Example 7.3. Inpainting of the text overprinted on an image:* (a) *Original image with overprinted text.* (b) *Restored image* $A_\lambda^M(f_K)$ *with* K *the set to be inpainted,* $\lambda = 250$*, and* $M = 1 \cdot 10^4$*. Computed value for* PSNR $= 42.2066\,\mathrm{dB}$*; relative* L^2*-error* $\epsilon = 0.016139$*.* (c) *Restored image by the AMLE method described in* [45, 39]*. Computed value for* PSNR $= 39.4405\,\mathrm{dB}$*. Relative* L^2*-error* $\epsilon = 0.022192$*.* (d) *Restored image by the split Bregman inpainting method described in* [29]*. Computed value for* PSNR $= 41.0498\,\mathrm{dB}$*. Relative* L^2*-error* $\epsilon = 0.018438$*.*

as $f(x) \geq g^{-M}(x, y)$ for all $x \in \mathbb{R}^n$ and $y \in \mathbb{R}^m$. Thus, for $y = 0$,

$$\mathsf{co}[\lambda|\cdot|^2 - f](x) \leq \mathsf{co}[\lambda(|x|^2 + |y|^2) - g^{-M}(x, y)]|_{y=0}\,.$$

On the other hand,

$$\mathsf{co}[\lambda(|x|^2 + |y|^2) - g^{-M}(x, y)]|_{y=0} \leq \lambda|x|^2 - g^{-M}(x, 0) = \lambda|x|^2 - f(x)\,.$$

Since the restriction of a convex function to a linear subspace remains convex, we also see that

$$\mathsf{co}[\lambda(|x|^2 + |y|^2) - g^{-M}(x, y)]|_{y=0} \leq \mathsf{co}[\lambda|\cdot|^2 - f](x)\,.$$

Thus

$$\mathsf{co}[\lambda(|x|^2 + |y|^2) - g^{-M}(x, z)]|_{y=0} = \mathsf{co}[\lambda|\cdot|^2 - f](x)\,;$$

hence the conclusion follows. ∎

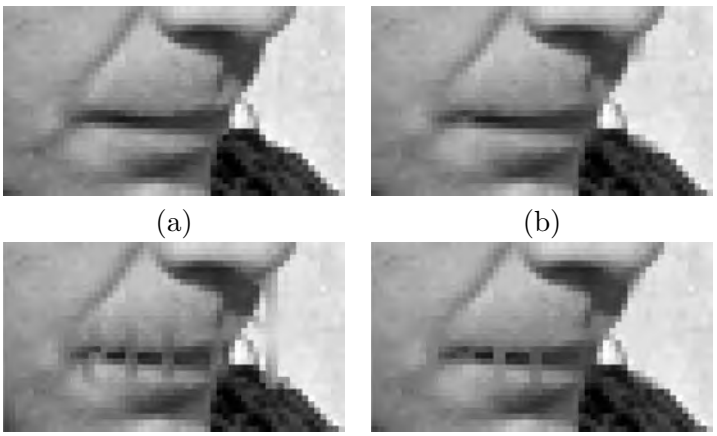

Figure 32. *Example 7.3. Comparison of a detail of the original image with the corresponding detail of the restored images according to the compensated convexity method and the TV-based method.* (a) *Lips detail of the original image without overprinted text.* (b) *Lips detail of the restored image* $A_\lambda^M(f_K)$. (c) *Lips detail of the AMLE-based restored image.* (d) *Lips detail of the TV-based restored image.*

Proof of Theorem 3.1. Note first that it follows from the fact that $a_0 < a_1 < \cdots < a_m$, $m \in \mathbb{N}$, that $V_{a_i} \subset V_{a_j}$ for all $0 \le i < j \le m$. Also, by the translation invariant property of compensated convex transforms, we may assume without loss of generality that $x_0 = 0$, so that

$$C_\lambda^l(f_K^M)(0) = \mathsf{co}[f_K^M + \lambda|\cdot|^2](0), \quad C_\lambda^u(f_K^{-M})(0) = \mathsf{co}[\lambda|\cdot|^2 - f_K^{-M}](0).$$

(i) Suppose that $x_0 = 0 \in \Gamma_{a_k}$, and consider the constant function $\ell(x) = a_k$. Clearly $a_k = f_K^M(0) + \lambda|0|^2$. Next we show that $a_k \le f_K^M(x) + \lambda|x|^2$ for $x \in \Gamma_{a_j}$, for $j \ne k$. Thus we need to prove that $a_k \le a_j + \lambda|x|^2$. Since $0 \in \Gamma_{a_k}$ and $x \in \Gamma_{a_j}$, we have $|x|^2 \ge \delta_0^2$. Under our assumption on λ, we see that $a_k \le a_j + \lambda|x|^2$ holds. Since $a_k < M$, we have $a_k \le f_K^M(x) + \lambda|x|^2$ for all $x \in \mathbb{R}^n$; hence $C_\lambda^l(f_K^M)(0) = a_k$. Similarly, we can show that $C_\lambda^u(f_K^{-M})(0) = a_k$, so that $A_\lambda^M(f_K)(0) = a_k$.

(ii) Since (i) clearly ensures that (3.2) holds whenever $f(x_0) = a_i$ for some $0 \le i \le m$, it remains to consider $x_0 = 0$ such that $a_i < f(x_0) < a_{i+1}$ for some $0 \le i \le m-1$. Now define

$$f_{K_i^-}^M(x) = \begin{cases} f_K^M(x), & x \notin \Gamma_{a_{i+1}}, \\ a_i, & x \in \Gamma_{a_{i+1}}, \end{cases} \qquad f_{K_i^+}^M(x) = \begin{cases} f_K^M(x), & x \notin \Gamma_{a_i}, \\ a_{i+1}, & x \in \Gamma_{a_i}. \end{cases} \tag{8.1}$$

Clearly $f_{K_i^-}^M(x) \le f_K^M(x) \le f_{K_i^+}^M(x)$ and $f_{K_i^-}^{-M}(x) \le f_K^{-M}(x) \le f_{K_i^+}^{-M}(x)$ for $x \in \mathbb{R}^n$, so that

$$C_\lambda^l(f_{K_i^-}^M)(x) \le C_\lambda^l(f_K^M)(x) \le C_\lambda^l(f_{K_i^+}^M)(x), \quad C_\lambda^u(f_{K_i^-}^{-M})(x) \le C_\lambda^u(f_K^{-M})(x) \le C_\lambda^u(f_{K_i^+}^{-M})(x), \quad x \in \mathbb{R}^n, \tag{8.2}$$

and hence by definition,

$$A_\lambda^M(f_{K_i^-})(x) \le A_\lambda^M(f_K)(x) \le A_\lambda^M(f_{K_i^+})(x), \quad x \in \mathbb{R}^n. \tag{8.3}$$

Next we will prove that

$$A_\lambda^M(f_{K_i^-})(0) = a_i, \quad A_\lambda^M(f_{K_i^+})(0) = a_{i+1}\,. \tag{8.4}$$

We first show that $\mathsf{co}[f^M_{K_i^-} + \lambda|\cdot|^2](0) \geq a_i$. Clearly $a_i \leq a_i + \lambda|x|^2 = f^M_{K_i^-}(x) + \lambda|x|^2$ for $x \in \Gamma_{a_i} \cup \Gamma_{a_{i+1}}$. For $x \in \Gamma_{a_j}$ with $j \neq i, i+1$, $a_i \leq a_j + \lambda|x|^2$ if $a_i - a_j \leq \lambda|x|^2$. This inequality holds if $a_m - a_0 \leq \lambda\delta_0^2$, that is, for $\lambda \geq (a_m - a_0)/\delta_0^2$, which is what we have assumed. The inequality $|x| \geq \delta_0$ for $x \in \Gamma_{a_j}$ can be proved by applying the intermediate value theorem to f. If $j < i$, as $f(0) > a_i$ and $f(x) = a_j < a_i$, we have, by the intermediate value theorem, that there is some $\xi \in (0,\,1)$ such that $f(\xi x) = a_i$, that is, $\xi x \in \Gamma_{a_i}$. Thus $|x| > (1-\xi)|x| = |x - \xi x| \geq \delta_0$ as $x \in \Gamma_{a_j}$ and $\xi x \in \Gamma_{a_i}$. If $j > i+1$, we have $f(0) < a_{i+1}$ and $f(x) = a_j > a_{i+1}$. Again we can use the same method to show that $|x| \geq \delta_0$.

By definition of the convex envelope, we see that there is an affine function ℓ such that $\ell(x) \leq f^M_{K_i^-}(x) + \lambda|x|^2$ for $x \in \mathbb{R}^n$ and $\ell(0) = \mathsf{co}[f^M_{K_i^-} + \lambda|\cdot|^2](0)$. From the proof above, we see that $\ell(0) \geq a_i$. Furthermore, if we let $K_l = \{x \in \mathbb{R}^n,\ \ell(x) = f^M_{K_i^-}(x) + \lambda|x|^2\}$, then $0 \in \mathsf{co}[K_l]$ and $\ell(x) = \mathsf{co}[f^M_{K_i^-} + \lambda|\cdot|^2](x)$ for $x \in \mathsf{co}[K_l]$.

By [55, Proposition 3.3], we see that $K_l \subset K$. Now we show that $K_l \subset \Gamma_{a_i} \cup \Gamma_{a_{i+1}}$. If this is not the case, then $K_l \cap \Gamma_{a_k} \neq \varnothing$ for some $k \notin \{i, i+1\}$. We consider two different cases: (a) $k < i$ and (b) $k > i+1$. For case (a), we see that there is some $x^* \in K_l \cap \Gamma_{a_k}$. Thus $\ell(x^*) = a_k + \lambda|x^*|^2$. As $f(0) > a_i$ and $f(x^*) = a_k < a_i$, similar to the proof above, by the intermediate value theorem, we have that there is some $\xi \in (0,\,1)$ such that $f(\xi x^*) = a_i$. Therefore, $\xi x^* \in \Gamma_{a_i}$ so that $\ell(\xi x^*) \leq f^M_{K_i^-}(\xi x^*)$. This implies

$$(1-\xi)\ell(0) + \xi\ell(x^*) \leq a_i + \lambda|\xi x^*|^2\,. \tag{8.5}$$

As $\ell(0) \geq a_i$ and $\ell(x^*) = a_k + \lambda|x^*|^2$, we derive from (8.5) that

$$(1-\xi)a_i + \xi\left(a_k + \lambda|x^*|^2\right) \leq a_i + \lambda|\xi x^*|^2; \tag{8.6}$$

hence,

$$\xi(1-\xi)\lambda|x^*|^2 \leq \xi(a_i - a_k)\,. \tag{8.7}$$

Thus we have found that for $0 < \xi < 1$

$$\lambda(1-\xi)|x^*|^2 \leq (a_i - a_k)\,. \tag{8.8}$$

Since $\lambda(1-\xi)|x^*|^2 \geq \lambda(1-\xi)^2|x^*|^2 \geq \lambda\delta_0^2$ and $a_i - a_k \leq a_m - a_0$, we have $\lambda\delta_0^2 \leq a_m - a_0$, which contradicts our assumption on λ.

If case (b) occurs, we have $f(0) < a_{i+1}$ and $f(x^*) = a_k > a_{i+1}$. Again by the intermediate value theorem, there is some $\xi \in (0,\,1)$ such that $f(\xi x^*) = a_{i+1}$. However, note that here the value of $f^M_{K_i^-}$ on $\Gamma_{a_{i+1}}$ is a_i. Therefore, a similar argument to that for case (a) will lead to a contradiction. Thus in both cases we have proved that $K_l \subset \Gamma_{a_i} \cup \Gamma_{a_{i+1}}$.

Now we consider $C^u_\lambda(f^{-M}_{K_i^-})(0) = \mathsf{co}[\lambda|\cdot|^2 - f^{-M}_{K_i^-}](0)$. Let $\hat\ell$ be the affine function such that $\hat\ell(x) \le \lambda|x|^2 - f^{-M}_{K_i^-}(x)$, $\hat\ell(0) = \mathsf{co}[\lambda|\cdot|^2 - f^{-M}_{K_i^-}](0)$, and let $K_u = \{x \in K,\ \hat\ell(x) = \lambda|x|^2 - f^{-M}_{K_i^-}(x)\}$. Again we have $\hat\ell(0) \ge -a_i$ and we can also show that $K_u \subset \Gamma_{a_i} \cup \Gamma_{a_{i+1}}$. By the definition of the convex envelope, we have

(8.9)

$$\begin{aligned}
&\mathsf{co}[f^M_{K_i^-} + \lambda|\cdot|^2](0)\\
&\quad= \inf\left\{\sum_{k=1}^{n+1}\lambda_k\Big(f^M_{K_i^-}(x_k) + \lambda|x_k|^2\Big),\ x_k\in\mathbb{R}^n,\ \lambda_k\ge 0,\ \sum_{k=1}^{n+1}\lambda_k = 1,\ \sum_{k=1}^{n+1}\lambda_k x_k = 0\right\}\\
&\quad= \inf\left\{\sum_{k=1}^{n+1}\lambda_k\Big(f^M_{K_i^-}(x_k) + \lambda|x_k|^2\Big),\ x_k\in K_l,\ \lambda_k\ge 0,\ \sum_{k=1}^{n+1}\lambda_k = 1,\ \sum_{k=1}^{n+1}\lambda_k x_k = 0\right\}\\
&\quad= \inf\left\{\sum_{k=1}^{n+1}\lambda_k\Big(f^M_{K_i^-}(x_k) + \lambda|x_k|^2\Big),\ x_k\in K_l\cup K_u,\ \lambda_k\ge 0,\ \sum_{k=1}^{n+1}\lambda_k = 1,\ \sum_{k=1}^{n+1}\lambda_k x_k = 0\right\}\\
&\quad= a_i + \inf\left\{\sum_{k=1}^{n+1}\lambda_k\lambda|x_k|^2,\ x_k\in K_l\cup K_u,\ \lambda_k\ge 0,\ \sum_{k=1}^{n+1}\lambda_k = 1,\ \sum_{k=1}^{n+1}\lambda_k x_k = 0\right\}\\
&\quad=: a_i + C_0\,.
\end{aligned}$$

Similarly, we have $\mathsf{co}[\lambda|\cdot|^2 - f^{-M}_{K_i^-}](0) = -a_i + C_0$, and hence

$$A^M_\lambda(f_{K_i^-})(0) = \frac{1}{2}\Big(\mathsf{co}[f^M_{K_i^-} + \lambda|\cdot|^2](0) - \mathsf{co}[\lambda|\cdot|^2 - f^{-M}_{K_i^-}](0)\Big) = a_i\,. \tag{8.10}$$

By using the same argument as above, we can also show that $A^M_\lambda(f_{K_i^+})(0) = a_{i+1}$, and this proves (8.4).

(iii) Suppose $f(0) < a_0$. If we let ℓ be the affine function such that $\ell(x) \le f^M_K(x) + \lambda|x|^2$, $\ell(0) = \mathsf{co}[f^M_K + \lambda|\cdot|^2](0)$, and let $K_l = \{x \in \mathsf{co}[K],\ \ell(x) = f^M_K(x) + \lambda|x|^2\}$, then in this special case we only need to show that $K_l \subset \Gamma_{a_0}$. As $a_0 < a_1 < \cdots < a_m$, we only need to rule out one possibility that $K_l \cap \Gamma_i \ne \emptyset$ for any $0 < i \le m$. By following the arguments of the proof of (ii)(b), we can show that $K_l \subset \Gamma_0$. Similarly, we can also show that $K_u \subset \Gamma_0$, where $K_u = \{x \in \mathsf{co}[K], \hat\ell(x) = \lambda|x|^2 - f^{-M}_K(x)\}$ for the affine function $\hat\ell$ such that $\hat\ell(x) \le \lambda|x|^2 - f^{-M}_K(x)$ and $\hat\ell(0) = \mathsf{co}[\lambda|\cdot|^2 - f^{-M}_K](0)$. The proof is then similar to that of part (ii). Note that here we do not have to introduce functions $f^M_{K_0^+}$ and $f^M_{K_0^-}$ as in (ii) given that the condition we have is $f(0) < a_0$ while in (ii) we had $a_i < f(0) < a_{i+1}$. ∎

Proof of Proposition 3.3. (i) Without loss of generality, we may assume $x_0 = 0 \in \Omega_i$. Now note that Corollary 2.7, applied with f, r, and R given by $\tilde f$, R, and $R+1$, respectively, gives that

$$|A^M_\lambda(\tilde f_{K_{R+1}})(0) - \tilde f(0)| \le \tilde\omega\left(r_c(0) + \frac{\tilde a}{\lambda} + \sqrt{\frac{2\tilde b}{\lambda}}\right). \tag{8.11}$$

Then since $0 \in \Omega_i \subset V_{a_m}$, it follows that $\tilde f(0) = f(0)$, and also that $r_c(0) \le d_i(0)$, by (2.9). To prove (3.5), it thus remains to show that $A^M_\lambda(\tilde f_{K_{R+1}})(0) = A^M_\lambda(f_K)(0)$. To see this, note

first that by arguments similar to those in the proof of [55, Theorem 3.7], we have that

$$C^l_\lambda(\tilde{f}^M_{K_{R+1}})(0) = \sum_{k=1}^{n^*} \lambda_k(\tilde{f}_{K_R}(x_k) + \lambda|x_k|^2) \tag{8.12}$$

for some $2 \le n^* \le n+1$, $\lambda_k > 0$, $x_k \in K_{R+1}$, $k = 1, 2, \dots, n^*$, with $\Sigma_{k=1}^{n^*}\lambda_k = 1$ and $\Sigma_{k=1}^{n^*}\lambda_k x_k = 0$. Now if $x_k \in K$ for each $1 \le k \le n^*$, then $\tilde{f}_{K_{R+1}}(x_k) = f_K(x_k)$, and hence $C^l_\lambda(\tilde{f}^M_{K_{R+1}})(0) = C^l_\lambda(f^M_K)(0)$. So suppose, for contradiction, that $x_{k_0} \in K_{R+1} \setminus K = B^c(0; R+1)$. Then there exists an affine function ℓ such that

$$\ell(y) \le \tilde{f}^M_{K_{R+1}}(y) + \lambda|y|^2 \text{ for all } y \in \mathbb{R}^n, \quad \ell(x_k) = \tilde{f}^M_{K_{R+1}}(x_k) + \lambda|x_k|^2, \ 1 \le k \le n^*,$$

so that

$$\ell(x_{k_0}) = \tilde{f}^M_{K_{R+1}}(x_{k_0}) + \lambda|x_{k_0}|^2 = a_m + 1 + \lambda|x_{k_0}|^2.$$

Since $\tilde{f}^M_{K_{R+1}}(y) = a_m + 1$ for all $y \in B^c(0, R+1)$, ℓ must be the unique tangent plane to the function $y \to a_m + 1 + \lambda|y|^2$ at $y = x_{k_0}$, namely

$$\ell(y) = a_m + 1 + \lambda|x_{k_0}|^2 + 2\lambda x_{k_0} \cdot (y - x_{k_0}), \quad y \in \mathbb{R}^n.$$

Now it follows from the fact that this plane does not touch the graph of $y \to a_m + 1 + \lambda|y|^2$ at any other point that $x_k \notin B^c(0, R+1)$ for $1 \le k \le n^*$, $k \ne k_0$, and hence, since $n^* \ge 2$, there must exist $x_{\hat{k}}$, $\hat{k} \ne k_0$, with $x_{\hat{k}} \in \Gamma_{a_j}$ for some $1 \le j \le m$ and $\ell(x_{\hat{k}}) = \tilde{f}^M_{K_{R+1}}(x_{\hat{k}}) + \lambda|x_{\hat{k}}|^2 = a_j + \lambda|x_{\hat{k}}|^2$. But then

$$a_m + 1 + \lambda|x_{k_0}|^2 + 2\lambda x_{k_0} \cdot x_{\hat{k}} - 2\lambda|x_{k_0}|^2 = a_j + \lambda|x_{\hat{k}}|^2,$$

and hence, since $x_{k_0} \in B^c(0; R+1)$ and $x_{\hat{k}} \in B(0, R)$,

$$a_m - a_j + 1 = \lambda(|x_{\hat{k}}|^2 - 2x_{k_0} \cdot x_{\hat{k}} + |x_{k_0}|^2) = \lambda|x_{\hat{k}} - x_{k_0}|^2 > \lambda,$$

which contradicts the assumption on λ. Likewise, $C^u_\lambda(\tilde{f}^{-M}_{K_{R+1}})(0) = C^u_\lambda(\tilde{f}^{-M}_K)(0)$, and hence $A^M_\lambda(\tilde{f}_{K_{R+1}})(0) = A^M_\lambda(f_K)(0)$, as required.

(ii) The proof of the Lipschitz case follows similar arguments. ∎

Proof of Theorem 4.1. Similar to the proof of Theorem 3.1(i), we fix $x_{j_0} \in K$ and let $f_\lambda(x) = \lambda|x - x_{j_0}|^2 - f^{-M}_K(x)$. Define $\ell(x) = -f(x_{j_0})$ for all $x \in \mathbb{R}^n$. Then ℓ is a constant function and so is affine. Clearly $\ell(x_{j_0}) = f_\lambda(x_{j_0})$. We need to prove that

$$\ell(x) \le f_\lambda(x) \tag{8.13}$$

for all $x \in \mathbb{R}^n$ so that $\mathsf{co}[f_\lambda](x_{j_0}) = \ell(x_{j_0}) = -f(x_{j_0})$; hence $C^u_\lambda(f^{-M}_K)(x_{j_0}) = f(x_{j_0})$. Inequality (8.13) is equivalent to

$$-f(x_{j_0}) \le \lambda|x - x_{j_0}|^2 - f^{-M}_K(x), \quad x \in \mathbb{R}^n.$$

If $x \in \mathbb{R}^n \setminus K$, $f_K^M(x) = -M$. Since $-f(x_{j_0})) < M < \lambda|x - x_{j_0}|^2 + M$, we clearly have $\ell(x) \le f_\lambda(x)$ for all $x \in \mathbb{R}^n \setminus K$. If $x_j \in K$ and $x_j \neq x_{j_0}$, we need to prove that

$$-f(x_{j_0}) \le \lambda|x_j - x_{j_0}|^2 - f(x_j), \quad \text{or, equivalently,} \quad f(x_j) - f(x_{j_0}) \le \lambda|x_j - x_{j_0}|^2 .$$

Since $\alpha = \min\{|x_i - x_j|,\ x_i, x_j \in K,\ x_i \neq x_j\}$, if $\lambda > L/\alpha$, we have

$$f(x_j) - f(x_{j_0}) \le L|x_j - x_{j_0}| \le \lambda\alpha|x_j - x_{j_0}| \le \lambda|x_j - x_{j_0}|^2 ,$$

which completes the proof. ∎

Proof of Lemma 4.3. We may write $\ell_s(x) = a \cdot x + b$ with $a \in \mathbb{R}^n$ and $b \in \mathbb{R}$. We see that $D\ell_s(x) = a$, and we need to give an estimate of $|a|$. Since we have $\ell_s(x_i) = f_S(x_i)$ and $|\ell_s(x_i) - \ell_s(x_1)| = |f_S(x_i) - f_S(x_1)| \le L|x_i - x_1|$, we see that $|a \cdot (x_i - x_1)| \le L|x_i - x_0|$ for $i = 1, 2, \ldots, k$. As $\dim(\mathsf{co}[S]) = n$, there are at least n-vectors, say $\{x_2 - x_1, \ldots, x_{n+1} - x_1\}$, which are linearly independent and hence form a basis of $\mathbb{R}^n$. If we let $\{e_1, \ldots, e_n\}$ be any orthonormal basis of $\mathbb{R}^n$, there is an $n \times n$ invertible matrix $A = (a_{ij})_{i,j=1}^n$ such that $e_i = \sum_{j=1}^n a_{ij}(x_{j+1} - x_1)$. Hence

$$|a \cdot e_i| \le \sum_{j=1}^n |a_{ij}||a \cdot (x_{j+1} - x_1)| \le L \left(\sum_{j=1}^n |a_{ij}|^2 \right)^{1/2} \left(\sum_{j=1}^n |x_{j+1} - x_1|^2 \right)^{1/2} .$$

Therefore, the Euclidean norm of a satisfies $|a| \le L|A|(\sum_{j=1}^n |x_i - x_0|^2)^{1/2}$, where $|A|$ denotes the Frobenius norm of the matrix A, and can then take $C_s = |A|(\sum_{j=1}^n |x_i - x_0|^2)^{1/2}$, which completes the proof. ∎

Proof of Theorem 4.5. We prove the result for the upper transform. The proof of the lower transform follows similar arguments.

Let us consider the affine function $\lambda r_s^2 - \ell_s(x)$. For $x \in S$, clearly

$$\lambda r_s^2 - \ell_s(x) = \lambda r_s^2 - f_K(x) = \lambda|x - x_s|^2 - f_K^{-M}(x) . \tag{8.14}$$

If we can show that $\lambda r_s^2 - \ell_s(x) < \lambda|x - x_s|^2 - f_K^{-M}(x)$ for $x \in \mathbb{R}^n \setminus S$, then one obtains

$$\mathsf{co}[\lambda|(\cdot) - x_s|^2 - f_K^{-M}](x) = \lambda r_s^2 - \ell_s(x) \tag{8.15}$$

for $x \in \mathsf{co}[S]$, and the proof for the upper transform then follows.

We consider two different cases: (i) $x \in K \setminus S$ and (ii) $x \in \mathbb{R}^n \setminus K$.

For case (i), let $x \in K \setminus S$. We need then to prove that

$$\lambda r_s^2 - \ell_s(x) < \lambda|x - x_s|^2 - f_K(x) , \tag{8.16}$$

or, equivalently, that

$$\lambda r_s^2 - \ell_s(x) + f_K(x) < \lambda|x - x_s|^2 . \tag{8.17}$$

We have the following estimates for the left-hand side of (8.17):

$$\begin{aligned}\lambda r_s^2 - \ell_s(x) + f_K(x) &\le \lambda r_s^2 + |\ell_s(x) - \ell_s(x_s)| + |\ell_s(x_s)| + A_0 \\ &\le \lambda r_s^2 + C_s L|x - x_s| + C_s L r_s + 2A_0\,.\end{aligned} \tag{8.18}$$

We have used the fact that for any $x^* \in S$,

$$|\ell_s(x_s)| \le |\ell_s(x_s) - \ell_s(x^*)| + |\ell_s(x^*)| \le C_s L r_s + A_0 \tag{8.19}$$

as $\ell_s(x^*) = f_K(x^*)$. Therefore, (8.17) holds if

$$\lambda r_s^2 + C_s L|x - x_s| + C_s L r_s + 2A_0 < \lambda|x - x_s|^2\,. \tag{8.20}$$

Note that $|x - x_s| \ge r_s + \sigma_s$. Let us consider the function

$$g(t) = \lambda t^2 - \lambda r_s^2 - C_s L t - C_s L r_s - 2A_0\,. \tag{8.21}$$

If we can find conditions for λ such that $g(r_s + \sigma_s) > 0$ and $g'(t) > 0$ when $t \ge r_s + \sigma_s$, then (8.20) holds and (8.17) will be satisfied.

We see that $g(r_s + \sigma_s) > 0$ is equivalent to

$$\lambda[(r_s + \sigma_s)^2 - r_s^2] > C_s L(2r_s + \sigma_s) + 2A_0\,. \tag{8.22}$$

This last inequality is equivalent to (4.2). Thus (8.17) holds and thus $g(r_s + \sigma_s) > 0$.

Next we have $g'(t) = 2\lambda t - C_s L$. Since $g'(t)$ itself is an increasing function, we only need to show that $g'(r_s + \sigma_s) > 0$, which is equivalent to

$$\lambda > \frac{C_s L}{2(r_s + \sigma_s)}\,, \tag{8.23}$$

which follows from (4.2). This completes the proof for case (i).

(ii) Let $x \in \mathbb{R}^n \setminus K$; hence $-f_K^{-M}(x) = M$. We need to prove that

$$\lambda r_s^2 - \ell_s(x) < \lambda|x - x_s|^2 + M\,. \tag{8.24}$$

Again we have

$$\lambda r_s^2 - \ell_s(x) \le \lambda r_s^2 + C_s L|x - x_s| + C_s L r_s + A_0\,. \tag{8.25}$$

Therefore, we prove (ii) if

$$\lambda r_s^2 + C_s L|x - x_s| + C_s L r_s + A_0 < \lambda|x - x_s|^2 + M\,. \tag{8.26}$$

Since (4.2) is satisfied, then by inspection it is easy to verify that (8.26) holds for all non-negative numbers $|x - x_s| \ge 0$, which completes the proof. ∎

Proof of Lemma 4.9. (i) We see that both p_+ and p_- are well-defined functions in D and clearly $p_-(x) \le v \le p_+(x)$ for every $(x, v) \in \mathsf{co}[\Gamma_s]$. It is also easy to see that the two different expressions for $p_+(x)$ and, respectively, for $p_-(x)$ are equal.

(ii) Since $\mathsf{co}[\Gamma_s]$ is a convex polytope, we have, for any x_1, $x_2 \in D$ and for every $0 < t < 1$, that

$$t(x_1, p_+(x_1)) + (1-t)(x_2, p_+(x_2)) = (tx_1 + (1-t)x_2, tp_+(x_1) + (1-t)p_+(x_2)) \in \mathsf{co}(\Gamma_s)$$

as both D and $\mathsf{co}[\Gamma_s]$ are convex. Furthermore, by definition of p_+, $tp_+(x_1) + (1-t)p_+(x_2) \le p_+(tx_1 + (1-t)x_2)$. Thus p_+ is concave in D, and hence is continuous in D. Similarly we can show that p_- is convex, and hence continuous, in D. Also p_+ and p_- are both piecewise affine functions. In fact, since $\mathsf{co}[\Gamma_s]$ is a convex polytope, $\mathsf{co}[\Gamma_s]$ has finitely many closed n-dimensional faces. We may write $\partial\,\mathsf{co}[\Gamma_s] = \Gamma_+ \cup \Gamma_- \cup \Gamma_0$, where $\Gamma_+ = \cup_{k=1}^m F_k^+$, $\Gamma_- = \cup_{j=1}^l F_j^-$, and $\Gamma_0 = \cup_{r=1}^s F_r^0$ with F_k^+, F_j^-, and F_r^0 n-faces of $\mathsf{co}[\Gamma_s]$. For F_k^+, there is an affine function $\ell_k^+ : \mathbb{R}^n \to \mathbb{R}$ such that $\ell_k^+(x) = v$ if $(x, v) \in F_k^+$ and $\ell_k^+(x) > v$ if $(x, v) \in \mathsf{co}[\Gamma_s] \setminus (F_k^+)$. Similarly, for F_j^-, there is an affine function $\ell_j^- : \mathbb{R}^n \to \mathbb{R}$ such that $\ell_j^-(x) = v$ if $(x, v) \in F_j^-$ and $\ell_k^-(x) < v$ if $(x, v) \in \mathsf{co}[\Gamma_s] \setminus (F_j^-)$. Every F_r^0 is an n-face whose normal vectors are in $\mathbb{R}^n \times \{0\} \subset \mathbb{R}^n \times \mathbb{R}$; that is, F_r^0 is perpendicular to $D \times \{0\}$. Since the vertices of each F_k^+ are extreme points of $\mathsf{co}[\Gamma_s]$ and every point $x \in S$ is an extreme point of $\mathsf{co}[S]$, we see that for every extreme point (x, v) of $\mathsf{co}[\Gamma_s]$, x is an extreme point of D. Let $D_k^+ = P_{\mathbb{R}^n}(F_k^+)$ be the orthogonal projection from F_k^+ to $\mathbb{R}^n$; then D_k^+ is a convex polytope contained in D whose vertices are all in S. The projection $P_{\mathbb{R}^n}$ also maps the relative boundary of F_k^+ to the boundary of D_k^+, and the relative interior F_k^+ to the interior of D_k^+. Also on D_k^+, $p_+(x) = \ell_k^+(x)$. Thus $p_+(\cdot)$ is affine on D_k^+.

Similarly, for each F_j^-, we define $D_j^- = P_{\mathbb{R}^n}(F_j^-)$. Then the vertices of D_j^- belong to S and $p_-(x) := \ell_j^-(x)$ is affine on D_j^-.

(iii) It is easy to see that $\mathring{D}_k^+ \cap \mathring{D}_j^+ = \emptyset$ and $\mathring{D}_k^- \cap \mathring{D}_j^- = \emptyset$ for $k \ne j$. Next we show that $D = \cup_{k=1}^m D_k^+ = \cup_{j=1}^l D_j^-$.

If $\cup_{k=1}^m D_k^+ \ne D$, there is an interior point $x \in D \setminus \cup_{k=1}^m D_k^+$. By definition $(x, p_+(x)) \in \partial\,\mathsf{co}[\Gamma_s]$, and we may assume that $(x, p_+(x))$ lies in the relative interior of an n-face $F \subset \partial\,\mathsf{co}[\Gamma_s]$. If F is one of the F_j^-'s, this implies $p_+(x) = p_-(x)$. This cannot happen inside D. If F is one of the F_r^0's, then $D_r^0 := P_{\mathbb{R}^n}(F_r^0)$ is an $n-1$-dimensional polytope. If E is the $(n-1)$-dimensional plane in $\mathbb{R}^n$ containing D_r^0, then D must lie on one side of D_r^0. Therefore, $D_r^0 \subset \partial D$; hence x is a boundary point of D. This contradicts our assumption that x is an interior point of D. Thus $D = \cup_{k=1}^m D_k^+$. Similarly, we can show that $D = \cup_{j=1}^l D_j^-$.

The other conclusions also follow from the above arguments. ∎

Proof of Theorem 4.11. Since $\mathsf{co}[S] = \cup_{k=1}^m D_k^+$, then on each D_k^+, there is an affine function $\ell_k^+ : \mathbb{R}^n \to \mathbb{R}$ such that $\ell_k^+(x) = p_k^+(x)$ for $x \in D_k^+$ and $\ell_k^+(x) > f_K(x)$ for $x \in S_k^+$, where S_k^+ is the set of extreme points of D_k^+ given by Lemma 4.9 which is a subset of S. Let $C_k^+ > 0$ be the constant given by Lemma 4.3 so that $|D\ell_k^+(x)| < C_k^+ L \le C_s L$.

If we can show that $\mathsf{co}[\lambda|(\cdot) - x_s|^2 - f_K^{-M}] = \lambda r_s^2 - \ell_k^+(x)$ for $x \in D_k^+$, the proof is finished. As in the proof of Theorem 4.5, we have to consider different cases. If $x \in \mathbb{R}^n$ or $x \in \mathbb{R}^n \setminus K$ or $x \in K \setminus S$, the proof for the inequality $\lambda r_s^2 - l_k^+(x) \le \lambda|x - x_s|^2 - f_K^{-M}(x)$ is the same as

that in the proof of Theorem 4.5. The only new case we have to consider is for $x \in S \setminus S_k^+$.

But for $x \in S \setminus S_k^+$, the above inequality is

$$\lambda r_s^2 - \ell_k^+(x) \leq \lambda |x - x_s|^2 - f_K(x) = \lambda r_s^2 - f_K(x)\,, \tag{8.27}$$

which is equivalent to $\ell_k^+(x) \geq f_K(x)$ as $S \subset \partial B(x_s; r_s)$. We also know from Lemma 4.9 that $\ell_k^+(x) > f_K(x)$ for $x \in S \setminus S_k^+$. Therefore, on each D_k^+, (8.27) holds as $p_+(x) = \ell_k^+(x)$ on D_k^+. The proof for the lower transform is similar. The proof is finished. ∎

Proof of Corollary 5.4. For the proof of this result, we first follow the proof of Theorem 2.5 so that the points x^i for the convex envelope are in $\bar{\Omega}$. Then we follow the proof of [55, Theorem 3.7] to show that x^i's can only be in K. The rest of the proof then follows from that of Theorem 2.5. ∎

Acknowledgments. The authors are extremely grateful to the anonymous referees, whose constructive comments on earlier versions of the manuscript have contributed to produce a better version of the paper. The authors would also like to thank Isaac Newton Institute for Mathematical Sciences for support and hospitality during the program "Variational methods and effective algorithms for imaging and vision," when part of the work on this paper was undertaken. K.Z. wishes to thank The University of Nottingham for its support. The authors finally would like to thank Simone Parisotto for delightful discussions on the numerical simulations of surface reconstructions from real data.

REFERENCES

[1] *Srtm and landcover download site*, http://rmd.neoknet.com/srtm1/ (accessed: 2018-05-04).

[2] A. Almansa, F. Cao, Y. Gousseau, and B. Rougé, *Interpolation of digital elevation models using AMLE and related methods*, IEEE Trans. Geosci. Remote Sensing, 40 (2002), pp. 314–325, https://doi.org/10.1109/36.992791.

[3] L. Ambrosio, N. Fusco, and D. Pallara, *Functions of Bounded Variation and Free Discontinuity Problems*, Clarendon Press, Oxford, UK, 2000.

[4] F. Andreu, C. Ballester, V. Caselles, and J. M. Mazón, *The Dirichlet problem for the total variation flow*, J. Funct. Anal., 180 (2001), pp. 347–403, https://doi.org/10.1006/jfan.2000.3698.

[5] G. Aronsson, *Extension of functions satisfying Lipschitz conditions*, Ark. Math., 6 (1967), pp. 551–561, https://doi.org/10.1007/BF02591928.

[6] Z. Belhachmi, D. Bucur, B. Burgeth, and J. Weickert, *How to choose interpolation data in images*, SIAM J. Appl. Math., 70 (2009), pp. 333–352, https://doi.org/10.1137/080716396.

[7] G. Bellettini, V. Caselles, and M. Novaga, *The total variation flow in* $\mathbb{R}^N$, J. Differential Equations, 184 (2002), pp. 475–525, https://doi.org/10.1006/jdeq.2001.4150.

[8] M. Bertalmio, G. Sapiro, V. Caselles, and C. Ballester, *Image inpainting*, in Proceedings of the 27th SIGGRAPH, ACM, New York, 2000, pp. 417–424, https://doi.org/10.1145/344779.344972.

[9] M. Bildhauer, M. Fuchs, and J. Weickert, *Denoising and inpainting of images using TV-type energies: Theoretical and computational aspects*, J. Math. Sci., 219 (2016), pp. 899–910, https://doi.org/10.1007/s10958-016-3153-y.

[10] K. Bredies, K. Kunisch, and T. Pock, *Total generalized variation*, SIAM J. Imaging Sci., 3 (2010), pp. 492–526, https://doi.org/10.1137/090769521.

[11] M. D. Buhmann, *Radial Basis Functions*, Cambridge University Press, Cambridge, UK, 2004.

[12] J. Cai, R. Chan, and B. Morini, *Minimization of an edge-preserving regularization functional by conjugate gradient type methods*, in Image Processing Based on Partial Differential Equations, X. Tai, K. Lie, T. F. Chan, and S. Osher, eds., Springer, New York, 2005, pp. 109–122, https://doi.org/10.1007/978-3-540-33267-1_7.

[13] V. Caselles, J. Morel, and C. Sbert, *An axiomatic approach to image interpolation*, IEEE Trans. Image Process., 7 (1998), pp. 376–386, https://doi.org/10.1109/83.661188.
[14] R. H. Chan, C.-W. Ho, and M. Nikolova, *Salt-and-pepper noise removal by median-type noise detectors and detail-preserving regularization*, IEEE Trans. Image Process., 14 (2005), pp. 1479–1485, https://doi.org/10.1109/TIP.2005.852196.
[15] T. F. Chan and S. H. Kang, *Error analysis for image inpainting*, J. Math. Imag. Vis., 26 (2006), pp. 85–103, https://doi.org/10.1007/s10851-006-6865-7.
[16] T. F. Chan and J. Shen, *Nontexture inpainting by curvature-driven diffusions*, J. Vis. Commun. Image Represent., 12 (2001), pp. 436–449, https://doi.org/10.1006/jvci.2001.0487.
[17] T. F. Chan and J. Shen, *Image Processing and Analysis: Variational, PDE, Wavelet, and Stochastic Methods*, SIAM, Philadelphia, 2005, https://doi.org/10.1137/1.9780898717877.
[18] M. DeBerg, M. VanKreveld, M. Overmars, and O. Schwarzkopf, *Computational Geometry*, 2nd ed., Springer-Verlag, Berlin, 2000.
[19] R. A. DeVore and G. G. Lorentz, *Constructive Approximation*, Springer-Verlag, Berlin, 1993.
[20] J. Duchon, *Interpolation des fonctions de deux variables suivant le principe de la flexion des plaques minces*, Rev. Française Automat. Informat. Recherche Opérationnelle Sér., 10 (1976), pp. 5–12.
[21] J. Dugundji, *Topology*, Allyn and Bacon, Boston, MA, 1970.
[22] H. Edelsbrunner, *Algorithms in Combinatorial Geometry*, Springer-Verlag, Berlin, 1987.
[23] G. E. Fasshauer, *Meshfree Approximation Methods with MATLAB*, World Scientific, Singapore, 2007.
[24] H. Federer, *Geometric Measure Theory*, Springer-Verlag, Berlin, 1969.
[25] R. Franke, *A Critical Comparison of Some Methods for Interpolation of Scattered Data*, Tech. rep. NPS-53-79-003, Naval Postgraduate School, Monterey, CA, 1979.
[26] R. Franke, *Scattered data interpolation: Tests of some methods*, Math. Comput., 38 (1982), pp. 181–200, https://doi.org/10.1090/S0025-5718-1982-0637296-4.
[27] D. Gesch, G. Evans, J. Mauck, J. Hutchinson, and W. Carswell, Jr., *The National Map Elevation*, U.S. Geological Survey Fact Sheet 3053, 2009.
[28] P. Getreuer, *Contour stencils: Total variation along curves for adaptive image interpolation*, SIAM J. Imaging Sci., 4 (2011), pp. 954–979, https://doi.org/10.1137/100802785.
[29] P. Getreuer, *Total variation inpainting using split Bregman*, Image Process. On Line, 2 (2012), pp. 147–157, https://doi.org/10.5201/ipol.2012.g-tvi.
[30] M. Giaquinta, G. Modica, and J. Soucek, *Functionals with linear growth in the calculus of variations* I, Comment. Math. Univ. Carolinae, 20 (1979), pp. 143–156.
[31] E. Giusti, *Minimal Surfaces and Functions of Bounded Variation*, Birkhäuser, Basel, 1984.
[32] P. Henrici, *Discrete Variable Methods in Ordinary Differential Equations*, John Wiley & Sons, New York, 1967.
[33] J.-B. Hiriart-Urruty and C. Lemaréchal, *Fundamentals of Convex Analysis*, Springer-Verlag, Berlin, 2001.
[34] R. Jensen, *Uniqueness of Lipschitz extensions: Minimizing the Sup norm of the gradient*, Arch. Ration. Mech. Anal., 123 (1993), pp. 51–74, https://doi.org/10.1007/BF00386368.
[35] J. Lellmann, J. Morel, and C. Schönlieb, *Anisotropic third-order regularization for sparse digital elevation models*, in Scale Space and Variational Methods in Computer Vision, A. Kuijper, K. Bredies, T. Pock, and H. Bischof, eds., Springer, Berlin, 2013, pp. 161–173, https://doi.org/10.1007/978-3-642-38267-3_14.
[36] S. Lodha and R. Franke, *Scattered data techniques for surfaces*, in Proceedings of Dagstuhl '97, Scientific Visualization, Vol. 18, G. Nielson, H. Hagen, and F. Post, eds., IEEE Computer Society, Washington, DC, 1999, pp. 181–222.
[37] A. Oberman, *The convex envelope is the solution of a nonlinear obstacle problem*, Proc. Amer. Math. Soc., 135 (2007), pp. 1689–1694, https://doi.org/10.1090/S0002-9939-07-08887-9.
[38] A. Okabe, B. Boots, K. Sugihara, and S. N. Chiu, *Spatial Tessellations*, 2nd ed., John Wiley & Sons, Chichester, UK, 2000.
[39] S. Parisotto and B. Schönlieb, *MATLAB codes for the Image Inpainting Problem*, GitHub repository, MATLAB Central File Exchange, September 2016.
[40] M. J. D. Powell, *Approximation Theory and Methods*, Cambridge University Press, Cambridge, UK, 1981.

[41] R. T. Rockafellar, *Convex Analysis*, Princeton University Press, Princeton, NJ, 1970.
[42] L. Rudin, S. Osher, and E. Fatemi, *Nonlinear total variation based noise removal algorithms*, Phys. D, 60 (1992), pp. 259–268, https://doi.org/10.1016/0167-2789(92)90242-F.
[43] G. Sapiro, *Geometric Partial Differential Equations and Image Analysis*, Cambridge University Press, New York, 2001.
[44] O. Savin, C^1 *regularity for infinity harmonic functions in two dimensions*, Arch. Ration. Mech. Anal., 176 (2005), pp. 351–361, https://doi.org/10.1007/s00205-005-0355-8.
[45] C. Schönlieb, *Partial Differential Equation Methods for Image Inpainting*, Cambridge University Press, New York, 2015.
[46] P. Soille, *Spatial distributions from contour lines: An efficient methodology based on distance transformations*, J. Vis. Commun. Image Represent., 2 (1991), pp. 138–150, https://doi.org/10.1016/1047-3203(91)90004-Y.
[47] M. L. Stein, *Interpolation of Spatial Data: Some Theory for Kriging*, Springer–Verlag, New York, 1999.
[48] L. N. Trefethen, *Spectral Methods in MATLAB*, Software Environ. Tools 10, SIAM, Philadelphia, 2000, https://doi.org/10.1137/1.9780898719598.
[49] L. N. Trefethen, *Approximation Theory and Approximation Practice*, SIAM, Philadelphia, 2013.
[50] J. Weickert, *Anisotropic Diffusion in Image Processing*, B.G. Teubner, Stuttgart, Germany, 1998.
[51] H. Wendland, *Scattered Data Approximation*, Cambridge University Press, New York, 2005.
[52] K. Zhang, *Compensated convexity and its applications*, Ann. Inst. H. Poincaré Anal. Non Linéaire, 25 (2008), pp. 743–771, https://doi.org/10.1016/j.anihpc.2007.08.001.
[53] K. Zhang, E. Crooks, and A. Orlando, *Compensated convexity transforms and numerical algorithms*, in preparation.
[54] K. Zhang, E. Crooks, and A. Orlando, *Compensated convexity, multiscale medial axis maps and sharp regularity of the squared-distance function*, SIAM J. Math. Anal., 47 (2015), pp. 4289–4331, https://doi.org/10.1137/140993223.
[55] K. Zhang, E. Crooks, and A. Orlando, *Compensated convexity methods for approximations and interpolations of sampled functions in Euclidean spaces: Theoretical foundations*, SIAM J. Math. Anal., 48 (2016), pp. 4126–4154, https://doi.org/10.1137/15M1045673.
[56] K. Zhang, A. Orlando, and E. Crooks, *Compensated convexity and Hausdorff stable extraction of intersections for smooth manifolds*, Math. Models Methods Appl. Sci., 25 (2015), pp. 839–873, https://doi.org/10.1142/S0218202515500207.
[57] K. Zhang, A. Orlando, and E. Crooks, *Compensated convexity and Hausdorff stable geometric singularity extractions*, Math. Models Methods Appl. Sci., 25 (2015), pp. 747–801, https://doi.org/10.1142/S0218202515500189.